



**NTNU – Trondheim**  
Norwegian University of  
Science and Technology

# Frictional pressure-drop models for steady-state and transient two-phase flow of carbon dioxide

**Frøydis Aakenes**

Master of Science in Product Design and Manufacturing

Submission date: June 2012

Supervisor: Inge Røinaas Gran, EPT

Co-supervisor: Svend Tollak Munkejord, SINTEF

Norwegian University of Science and Technology  
Department of Energy and Process Engineering



EPT-M-2012-97

**MASTER'S THESIS**

for

student Frøydis Aakenes

Spring 2012

Frictional pressure-drop models for steady-state and transient two-phase flow of carbon dioxide

*Friksjonstrykktapsmodeller for stasjonær og tidsavhengig tofasestrømning av karbondioksid***Background and objective**

Carbon dioxide (CO<sub>2</sub>) is greenhouse gas contributing to heating the planet. At the same time, it can be injected into oil and gas fields to increase the recovery. To be injected into oil or gas fields, the CO<sub>2</sub> needs to be transported from the point of capture, for instance in pipes. The CO<sub>2</sub> will generally contain impurities, which even in small amounts can significantly influence its thermophysical properties. During design, and when setting up operational procedures of the pipeline, it is necessary to be able to calculate transient scenarios. For example, during a depressurization due to closure of the pipeline, the temperature will decrease, and this can make the pipe material brittle. Therefore, it is important to be able to estimate the temperature drop. Among the relevant constitutive relations is the model for frictional pressure drop, which is also connected to the slip relation.

At SINTEF Energy Research, Department of Gas Technology, a numerical model for pipe flow of multiphase multicomponent mixtures is under development. This model will be employed in the present work.

**The following tasks are to be considered:**

1. Compare selected frictional pressure-drop models to available steady-state experimental data.
2. Implement selected frictional pressure-drop models in the above-mentioned numerical model. Perform tests and discuss the results. In particular,
  - a. A comparison should be made with the steady-state experimental data.
  - b. In the transient case, a discussion of the influence of friction model and slip model should be made.

Within 14 days of receiving the written text on the master thesis, the candidate shall submit a research plan for his project to the department.

When the thesis is evaluated, emphasis is put on processing of the results, and that they are presented in tabular and/or graphic form in a clear manner, and that they are analyzed carefully.

The thesis should be formulated as a research report with summary both in English and Norwegian, conclusion, literature references, table of contents etc. During the preparation of the text, the candidate should make an effort to produce a well-structured and easily readable report. In order to ease the evaluation of the thesis, it is important that the cross-references are correct. In the making of the report, strong emphasis should be placed on both a thorough discussion of the results and an orderly presentation.

The candidate is requested to initiate and keep close contact with his/her academic supervisor(s) throughout the working period. The candidate must follow the rules and regulations of NTNU as well as passive directions given by the Department of Energy and Process Engineering.


Risk assessment of the candidate's work shall be carried out according to the department's procedures. The risk assessment must be documented and included as part of the final report. Events related to the candidate's work adversely affecting the health, safety or security, must be documented and included as part of the final report.

Pursuant to "Regulations concerning the supplementary provisions to the technology study program/Master of Science" at NTNU §20, the Department reserves the permission to utilize all the results and data for teaching and research purposes as well as in future publications.

The final report is to be submitted digitally in DAIM. An executive summary of the thesis including title, student's name, supervisor's name, year, department name, and NTNU's logo and name, shall be submitted to the department as a separate pdf file. Based on an agreement with the supervisor, the final report and other material and documents may be given to the supervisor in digital format.

Department of Energy and Process Engineering, May 2012

  
Olav Bolland  
Department Head

  
Inge R. Gran  
Academic Supervisor

Research Advisors: 

# Abstract

Related to the technology of CO<sub>2</sub> capture, transport, and storage (CCS), an accurate transport model which predicts the behaviour of carbon-dioxide mixtures during steady-state and transient situations, is needed. A correct estimation of the frictional pressure-drop is an important part of such a model.

A *homogenous friction-model*, the *Friedel model* [20], and the *Cheng et al. model* [8] have been compared with six steady-state experiments using pure CO<sub>2</sub> [24]. The experiments were nearly adiabatic and within the following range: mass velocities from 1058 to 1663 kg/m<sup>2</sup>s, saturated temperatures from 3.8 to 17 °C (reduced pressures from 0.52 to 0.72), vapor fractions from 0.099 to 0.742, and pipe diameter of 10 mm. The Friedel model was found to be the most accurate model with a standard deviation of 9.7 % versus 55.74 % for the Cheng et al. model and 29.18 % for the homogenous model.

The selected friction models were implemented into a numerical model for pipe flow of multi-phase CO<sub>2</sub>, and one of the mentioned experiments [24] was reproduced. The result illustrates how the accuracy of the friction model is even more important when used as a part of the complete transport-model. This is mainly because the friction model and other sub-models, such as the equation of state, are coupled. During the implementation of the Cheng et al. model, certain errors in the original paper [8] were found and corrected.

In the case of a transient flow, the influence of the friction model and the associated slip relation, were explored. It was shown that wave speeds strongly depends on the slip relation used. The friction model itself will indirectly affect the wave speed. This is mainly because of the reduced fluid velocity arising when the driving force across the wave is reduced. However, the main effect of the friction model is the pressure gradient arising in regions where the velocity is non-zero.

## Sammendrag

I forbindelse med fangst, transport og lagring av CO<sub>2</sub> (CCS), vil det være behov for en nøyaktig modell som beskriver flerfase-transport av CO<sub>2</sub>. En korrekt prediksjon av friksjonstrykktapet vil være en viktig del av en slik modell.

En *homogen friksjonsmodell*, *Friedel-modellen* [20] og *Cheng et al.-modellen* [8] har blitt sammenliknet med seks stasjonære eksperimenter for ren CO<sub>2</sub> [24]. Eksperimentene ble kjørt under adiabatisk forhold og med en massefluks mellom 1058 og 1663 kg/m<sup>2</sup>s, likevektstemperatur mellom 3.8 og 17 °C (reduisert trykk mellom 0.52 og 0.72), strømmende massefraksjon mellom 0.099 og 0.742 og en indre rørdiameter på 10 mm. For de gitte strømningsforholdene [24], var Friedel-modellen den mest nøyaktige med et standardavvik på 9.7 %. For Cheng et al.-modellen og den homogene modellen var standardavviket på henholdsvis 55.74 % og 29.18 % .

Friksjonsmodellene ble videre implementert i en numerisk transportmodell for flerfase CO<sub>2</sub>, og et av de nevnte eksperimentene [24] ble simulert. Resultatene illustrerer at friksjonsmodellnøyaktigheten er enda viktigere når den benyttes som en del av en større modell. Hovedårsaken til dette er at friksjonsmodellen og andre sub-modeller, som for eksempel tilstandslikningen, er koplet. Under implementeringen av Cheng et al. modellen ble enkelte feil i originalartikkelen [8] funnet og rettet opp.

Hvordan friksjonsmodeller og de tilhørende slipp-modellene påvirker en transient strømning, har blitt undersøkt. Det ble vist at bølgehastighetene avhenger sterkt av slipp-modellen. Friksjonsmodellen vil påvirke bølgehastighetene indirekte. Dette skyldes først og fremst en reduksjon i fluidhastigheten, som følge av at trykkfallet over bølgene vil avta. Hovedeffekten av friksjonsmodellen vil være trykkgradienten som oppstår der fluidet strømmer.

# Preface

This master's thesis is the final work of a 5 year Master of Technology education program within the department of Mechanical Engineering at NTNU.

The work carried out has been a part of an ongoing project at SINTEF Energy Research called "CO<sub>2</sub> dynamics", with Statoil, Vattenfall, Gassco and NTNU as partners. One of the objectives in this project has been to develop a numerical model for pipe flow of multiphase multicomponent mixtures, with emphasis on CO<sub>2</sub> mixtures. The work carried out in this master's thesis is implemented in this numerical model.

First, I would like to thank my supervisor Inge Gran for making this project possible. Further, I would like to express a special thanks to my co-supervisor Svend Tollak Munkejord for his support and for always taking the time to answer my questions.

The analysis carried out in this report would not have been possible without experimental data, thus an important thanks goes to Statoil for giving me access to parts of a very useful SINTEF report [24] concerning frictional pressure-drop experiments carried out in 2008. The report [24] was a result of the CO2ITIS project financed by Statoil and the CLIMIT-program of the Research Council of Norway. I would also like to thank Gelein De Koeijer and Rudolf Held from Statoil, and Michael Drescher and Geir Skaugen from SINTEF, for all help related to the understanding of the work described in the report [24].

Last, but not least, a sincere thanks goes to Dr. Lixin Cheng for all his help and useful discussions related to the understanding and implementation of the Cheng et al. model.





# Contents

Abstract . . . . .	3
Sammendrag . . . . .	4
Preface . . . . .	5
Nomenclature . . . . .	11
<b>1 Introduction</b>	<b>15</b>
1.1 Background . . . . .	15
1.1.1 Global warming and greenhouse gas emissions . . . . .	15
1.1.2 CO <sub>2</sub> capture and storage (CCS) . . . . .	15
1.1.3 CO <sub>2</sub> transport . . . . .	16
1.2 Problem description . . . . .	17
1.3 Survey of the report . . . . .	18
<b>I THEORY</b>	<b>19</b>
<b>2 Multiphase flow</b>	<b>21</b>
2.1 Flow patterns . . . . .	21
2.2 Two-phase parameters . . . . .	22
2.3 Multiphase flow modeling . . . . .	23
2.3.1 Drift-flux model . . . . .	24
2.3.2 Source-term models . . . . .	25
2.3.3 Slip models . . . . .	26
2.4 Properties of the drift-flux model . . . . .	27
2.4.1 Characteristic properties . . . . .	27
2.4.2 Waves . . . . .	29
2.5 Boundary conditions . . . . .	30
2.6 Summary . . . . .	30
<b>3 Thermodynamics</b>	<b>31</b>
3.1 Equation of state . . . . .	31
3.1.1 State variables . . . . .	31
3.1.2 The fundamental equation . . . . .	31
3.1.3 Derived properties . . . . .	32
3.2 Span-Wagner equation of state . . . . .	32
3.2.1 Using the Span-Wagner EOS . . . . .	32
3.3 The stiffened-gas equation of state . . . . .	34
3.3.1 Parameter fitting . . . . .	35
3.4 Summary . . . . .	35

<b>4</b>	<b>Numerical methods</b>	<b>37</b>
4.1	Finite-volume methods . . . . .	37
4.2	The Courant-Friedrichs-Levy number . . . . .	38
4.3	Flux estimation . . . . .	39
4.3.1	The MUSTA method . . . . .	39
4.4	Summary . . . . .	41
<b>5</b>	<b>Frictional forces</b>	<b>43</b>
5.1	Friction modeling in single-phase flow . . . . .	43
5.1.1	Darcy friction-factor relations . . . . .	44
5.2	Friction modeling in two-phase flow . . . . .	45
5.3	Selected wall-friction models . . . . .	46
5.3.1	A homogeneous model . . . . .	46
5.3.2	The Friedel model . . . . .	47
5.3.3	The Cheng et al. model . . . . .	49
5.4	Summary . . . . .	51
<b>II</b>	<b>MATERIAL AND MODEL IMPLEMENTATION</b>	<b>53</b>
<b>6</b>	<b>Friction-model implementation</b>	<b>55</b>
6.1	The MATLAB-code . . . . .	55
6.2	Verification . . . . .	55
6.2.1	Results . . . . .	56
6.2.2	Slip-model sensitivity . . . . .	58
6.3	Summary . . . . .	59
<b>7</b>	<b>Experimental data</b>	<b>61</b>
7.1	Background . . . . .	61
7.2	The CO <sub>2</sub> pipeline test rig . . . . .	61
7.3	The experiments . . . . .	62
7.4	Vapor-fraction calculations . . . . .	62
7.5	The frictional pressure-drop . . . . .	64
7.6	Summary . . . . .	65
<b>8</b>	<b>Uncertainty and sensitivity</b>	<b>67</b>
8.1	Uncertainty . . . . .	67
8.1.1	Categorization of errors . . . . .	68
8.1.2	Error propagation . . . . .	68
8.1.3	Multiple-sample versus single-sample experiments . . . . .	69
8.2	Uncertainty analysis . . . . .	69
8.2.1	Sensor uncertainty . . . . .	69
8.2.2	Pressure-drop uncertainty . . . . .	70
8.2.3	Uncertainty in other variables . . . . .	70
8.3	Friction-model sensitivity . . . . .	72
8.4	Summary . . . . .	74

<b>III RESULTS AND DISCUSSION</b>	<b>75</b>
<b>9 Friction-model comparison</b>	<b>77</b>
9.1 Calculations . . . . .	77
9.2 Results . . . . .	78
9.3 Discussion . . . . .	81
9.3.1 Comparison with Friedel's results . . . . .	82
9.3.2 Comparison with Cheng et al.'s results . . . . .	82
9.4 Summary and conclusion . . . . .	82
<b>10 Steady-state simulation</b>	<b>83</b>
10.1 Mathematical models used . . . . .	83
10.1.1 Initial conditions . . . . .	83
10.1.2 Boundary conditions . . . . .	84
10.1.3 Numerical setup . . . . .	84
10.2 Results . . . . .	85
10.3 Discussion . . . . .	87
10.4 Summary and conclusions . . . . .	87
<b>11 Transient effects of friction models</b>	<b>89</b>
11.1 Mathematical models used . . . . .	89
11.1.1 Initial conditions . . . . .	89
11.1.2 Boundary conditions . . . . .	90
11.1.3 Parameters for the stiffened-gas EOS . . . . .	90
11.1.4 Constant fluid properties . . . . .	90
11.1.5 Numerical setup . . . . .	91
11.2 Cases . . . . .	91
11.3 Results for case 1 . . . . .	91
11.3.1 Grid refinement . . . . .	91
11.3.2 Physical behavior . . . . .	92
11.3.3 Eigenvalues . . . . .	94
11.4 Results for case 2 . . . . .	95
11.5 Results for case 3 . . . . .	96
11.6 Influence of slip relation . . . . .	97
11.7 Friction-model effects . . . . .	98
11.8 Summary and conclusions . . . . .	101
<b>12 Conclusions and further work</b>	<b>103</b>
<b>Appendix:</b>	
<b>A Zuber-Findlay slip relation</b>	<b>109</b>
A.1 Manipulation of the Zuber-Findlay slip relation . . . . .	109
A.1.1 Written in terms of the slip . . . . .	109
A.1.2 Written in a dimensionless form . . . . .	109
A.1.3 Written in terms of the total mass velocity, $G$ . . . . .	109
A.1.4 Written in terms of the void fraction . . . . .	110

---

<b>B</b>	<b>Implementation of the Rouhani-Axelsson version of the Zuber-Findlay slip relation</b>	<b>111</b>
<b>C</b>	<b>Implementation of boundary conditions</b>	<b>113</b>
<b>D</b>	<b>Typical CO<sub>2</sub>-transport pipes</b>	<b>115</b>
<b>E</b>	<b>Speed of sound for the stiffened gas EOS</b>	<b>117</b>
<b>F</b>	<b>Eigenvalues for the DF4 model</b>	<b>119</b>
	F.1 The parameter $\zeta$ . . . . .	119
	F.2 Calculations used in Section 11.3.3 . . . . .	120
<b>G</b>	<b>The experiments [24]</b>	<b>121</b>
<b>H</b>	<b>The implementation of the Cheng et al. flow-pattern map</b>	<b>123</b>

# Nomenclature

## Dimensionless numbers

CFL Courant-Friedrichs Levy number, see Equation (4.8)

Fr Froude number

Re Reynolds number

We Weber number

## Greek symbols

$\alpha$  Volume fraction

$\Lambda$  Eigenvalue matrix

$\epsilon$  Roughness

$\Gamma$  Phase-transfer rate

$\gamma$  Ratio of specific heats  $c_p/c_v$

$\lambda$  Eigenvalue

$\mu$  Viscosity

$\Phi$  Two-phase multiplier, see Equation (5.10)

$\phi$  Slip

$\rho$  Density

$\sigma$  Surface tension

$\tau$  Shear tension

$\theta$  Angle

$\zeta$  Function used in Equation 2.35

## Latin symbols

$q$  Heat

$q''$  Heat flux

$\bar{\epsilon}$  Mean error

$\mathbf{F}$  Discretized flux

$\mathbf{f}$  Flux

$\mathbf{Q}$  Volume averaged quantity

$\mathbf{q}$  Composite variable/ conserved variable

$\mathbf{R}$  Right eigen vector

$\mathbf{S}$  Source term

$\mathbf{u}$  Velocity

$\mathbf{w}$  Characteristic variable

$\dot{m}$  Mass-flow rate

$A$  Area

$a$  Specific Helmholtz free energy

$c$  Speed of sound

$C_p$  Extensive heat capacity, see Equation 2.33

$c_p$  Specific heat at constant pressure

[m]  
[kg/m<sup>3</sup>s]

[Ns/m<sup>2</sup>]

[kg/m<sup>3</sup>]

[N/m]

[N/m<sup>2</sup>]

[rad]

[W]

[W/m<sup>2</sup>]

[\*/m<sup>2</sup>s]

[m/s]

[kg/s]

[m<sup>2</sup>]

[J/kg]

[m/s]

[J/m<sup>3</sup>K]

[J/kgK]

$c_v$	Specific heat at constant volume	[J/kgK]
$d$	Diameter	[m]
$E$	Function used in Equation (5.21)	
$e$	Internal + kinetic energy	[J/kg]
$F$	Force	[N]
$F$	Function used in Equation (5.22)	
$f$	Darcy friction factor	
$f$	Function	
$G$	Mass flux (mass velocity)	[kg/m <sup>2</sup> s]
$g$	Gravitational acceleration	[m/s <sup>2</sup> ]
$g$	Specific Gibbs free energy	[J/kg]
$H$	Function used in Equation (5.23)	
$h$	Specific enthalpy	[J/kg]
$h_{ig}$	Heat of vaporization	[J/kg]
$j$	Volumetric flux	[m/s]
$K_s$	Slip constant	
$L$	Length	[m]
$M$	Number of time steps	
$N$	Number of grid cells	
$P$	Perimeter	[m]
$p$	Pressure	[Pa]
$R$	Measured value, see Equation (8.1)	
$r$	Measured value, see Section 8.1.2	
$r$	Radius	[m]
$S$	Wave speed	[m/s]
$s$	Specific entropy	[J/kgK]
$s_R$	Relative standard deviation	
$S_s$	Slip constant	
$T$	Temperature	[K]
$t$	Time	[s]
$U$	Overall heat-transfer coefficient	[W/m <sup>2</sup> K]
$x$	Flowing vapor-fraction	
$x$	Spatial location	[m]
$z_i$	Relative error	

**Subscripts**

0	Initial condition
0	Reference condition
$\infty$	Reference conditions
<i>crit</i>	At critical conditions
<i>g</i>	Related to gas phase
<i>i</i>	At fluid interphase
<i>i, j</i>	Spatial discretization
<i>k</i>	Related to phase <i>k</i>
<i>L</i>	Left
<i>l</i>	Related to liquid phase
<i>mix</i>	Related to mixture
<i>n, m</i>	Time discretization

<i>q</i>	Differentiation with respect to the composite variable $q$
<i>R</i>	Right
<i>sat</i>	At saturated conditions
<i>sur</i>	Surroundings
<i>t</i>	Time differentiation
<i>tot</i>	Total
<i>w</i>	At wall
<i>x</i>	Spatial differentiation

**Abbreviations**

CCS	CO <sub>2</sub> capture and storage
CFD	Computational fluid dynamics
DF3	Three-equation drift-flux (model)
DF4	Four-equation drift-flux (model)
EOS	Equation of state
MUSTA	Multi-stage





# Chapter 1

## Introduction

### 1.1 Background

#### 1.1.1 Global warming and greenhouse gas emissions

The world is facing a complex and challenging problem, that is the climate change. Scientists agree that the climate change is mainly caused by the increasing amount of greenhouse gasses (GHG) in the atmosphere produced by human activities, such as the extensive use of fossil fuels. Deep cuts in global emissions are required in order to avoid a further warming of the climate. However, an increasing amount energy is needed in the future, and the use of fossil fuels will probably remain the dominant source of energy for many years to come [3].

#### 1.1.2 CO<sub>2</sub> capture and storage (CCS)

According to IPCC (the Intergovernmental Panel on Climate Change), CO<sub>2</sub> emission is the most important GHG in terms of quantity (see Figure 1.1). This is the motivation for the technology named CO<sub>2</sub> Capture and Storage (CCS). CO<sub>2</sub> is 1) captured at the power plants or from other industrial applications, 2) transported and then, 3) injected and stored in geological formations underground. Thus, problems related to the use of fossil fuel is reduced.

Injection of CO<sub>2</sub> into reservoirs for Enhanced Oil Recovery (EOR) has been done since the 1970s, there are by now eight commercial-scale CCS projects in operation around the globe<sup>1</sup> and the capacity for storage is considered to be large and safe. Thus, the technology of CCS is regarded promising [18, 19, 23]. However, there are still several challenges in all the three fields mentioned above, – capture, transportation and storage. This report will only consider topics related to CO<sub>2</sub> transportation.

---

<sup>1</sup>Val Verde Natural Gas Plants (USA), Enid Fertilizer (USA), Shute Creek Gas Processing Facility (USA), Sleipner CO<sub>2</sub> Injection (Norway), Great Plains Synfuels Plant and Weyburn-Midale Project (Canada), In Salah CO<sub>2</sub> Storage (Algeria), Snøhvit CO<sub>2</sub> Injection (Norway), and Century Plant (USA) [22]

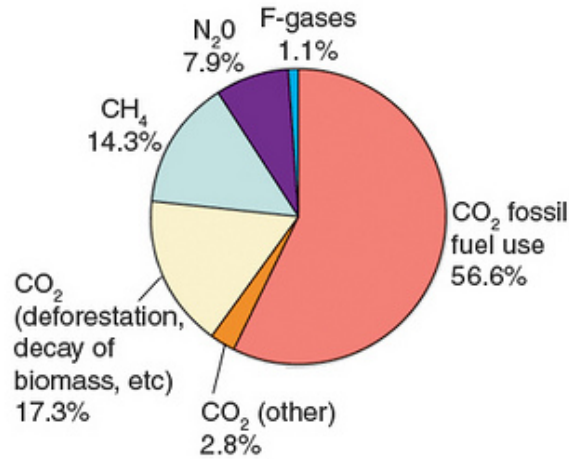


Figure 1.1: Total anthropogenic GHG emissions in 2004 in terms of CO<sub>2</sub>-equivalents [31]. As seen, most of the emissions is CO<sub>2</sub> (76.7%).

### 1.1.3 CO<sub>2</sub> transport

Once the CO<sub>2</sub> is captured, it has to be transported to the place where it will be injected and stored. Current means of transport are trucks, rail, ships and pipelines. The latter is the most common when dealing with large quantities and relatively long distances<sup>2</sup>. By compressing the CO<sub>2</sub> to about 150 bars, it will be super-critical. In this state the CO<sub>2</sub> has a relatively high density and low viscosity. This makes the transportation efficient.

Even though there exists a lot of experience concerning transportation of CO<sub>2</sub> in pipes, there are some differences between the existing pipelines and the future pipelines. First of all, the current experience is related to EOR and transportation of relatively pure CO<sub>2</sub>. In the case of CCS, larger amount of impurities may be present. This will change the properties of the fluid and hence the behavior of the flow. Another challenge is related to safety. Today, most of the pipelines are found in sparsely populated areas while future pipeline networks will most probably go through densely populated areas [23]. The consequences of failures will therefore be more serious. In order to make the transportation safe and efficient, accurate models which predict the behavior of CO<sub>2</sub> mixtures in different situations are needed. Situations such as steady-state transport and transient incidents, like a depressurization of a pipeline, are of interest.

<sup>2</sup>Existing long-distance pipelines are between 100 km and 1000 km [35]

## 1.2 Problem description

In order to predict the behavior of CO<sub>2</sub> pipe-flows, a transport model describing multiphase multicomponent mixtures is needed. SINTEF Energy Research, Department of Gas Technology, is currently developing such a numerical model. Throughout this report, this model will be referred to as the CO<sub>2</sub>-transport (COTT) model or the CO<sub>2</sub>-transport (COTT) code. The main objective of this master's thesis is to investigate one specific part of the CO<sub>2</sub>-transport model, – that is the modeling of the pressure drop arising in pipe flows due to frictional forces.

In many circumstances, a correct estimation of friction is crucial. First of all, the pipes of interest (see Appendix D) may be relatively long, often many hundreds kilometers. Thus, the estimated frictional pressure-drop per meter have a huge impact on the total required pumping power. Another important issue is that other flow variables and fluid properties are quite sensitive to the pressure in the pipe. For instance, if the pressure is not estimated correctly, neither will the temperature, the flowing vapor-fraction or any of the fluid properties. This issue is related to a concern arising during a depressurization of a pipeline, where both the pressure and the temperature will drop. A large temperature drop can make the steel pipe brittle, cracks may emerge and leakage may be the result. Friction will affect the size of the pressure drop. Therefore an accurate prediction of the frictional effect is essential.

In particular, the following questions are to be asked:

1. What friction model will most accurately describe the frictional pressure-drop arising in pipelines for carbon dioxide transport?
2. How will the friction model perform when used as a part of the complete CO<sub>2</sub>-transport model?
3. How and how much does the choice of friction model, and the associated slip relation, affect a transient flow?

## 1.3 Survey of the report

The questions in Section 1.2 will be answered by performing the following three tasks:

- Compare steady-state pressure-drop experiments with results obtained using selected friction models.
- Implement the selected friction correlations in the COTT model, perform a simulation, and compare with experimental data.
- Perform a transient simulation using the COTT code. Investigate how transient phenomena are affected by the choice of friction model and the associated slip correlation.

The first part of this report (Chapter 2–5) presents theory needed to understand the COTT model and the nature of friction forces and frictional modeling. In addition, the friction models used in this report, that is the Friedel model [20] and the Cheng et al. model [8], will be described in detail.

The second part of this report (Chapter 6–8) describes the implementation and verification of the Cheng et al. model, the experimental data used and the uncertainty related to the experiments.

The last part of this report (Chapter 9–11) presents the set-up and results for the above mentioned tasks.

Further work and the main conclusions are summarized in Chapter 12.

**Part I**  
**THEORY**



# Chapter 2

## Multiphase flow

The simplest multiphase flow is a two-phase flow. It consists of two different phases and can be a solid/liquid flow, a solid/gas flow or a gas/liquid flow. This report will consider a two-phase gas/liquid flow since this is typically what is present during transient situations and steady-state transport of pure CO<sub>2</sub>.

### 2.1 Flow patterns

Two-phase flows are often categorized based on the geometrical structure of the flow. The structures are called *flow patterns* and some of the most common patterns are illustrated in Figure 2.1.

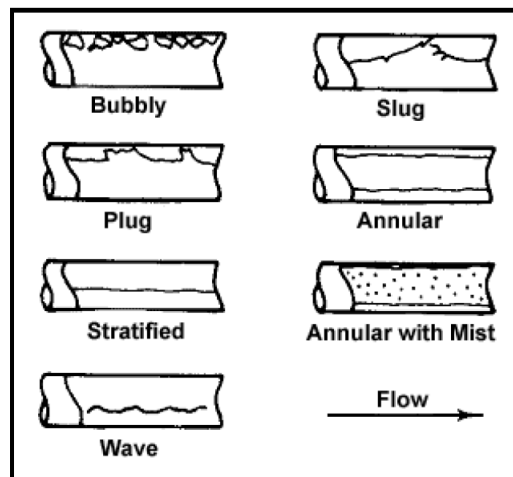


Figure 2.1: Two-phase flow patterns in horizontal flow [37, Ch.12].

## 2.2 Two-phase parameters

In order to describe the two-phase flow in a mathematical manner, the following parameters are typically used (when the flow is treated as one dimensional):

**The volume fraction (void fraction):** is the cross sectional area occupied by phase  $k$  divided by the total cross-sectional area.

$$\alpha_k \equiv \frac{A_k}{A_{tot}} = \frac{A_k}{A_l + A_g}, \quad (2.1)$$

where  $k$  takes on the values  $g$  and  $l$ , representing the gas and liquid phase respectively. The term *void fraction* refer to the gas volume fraction.

**The component volumetric-flux:** is the volume flow of phase  $k$  divided by the total cross sectional area,  $A_{tot}$ . This is sometimes called the superficial component-velocity [5, Ch. 1, p3].

$$j_k \equiv \alpha_k u_k \quad (2.2)$$

**The total volumetric flux:** is the sum of all the volumetric fluxes.

$$j \equiv j_g + j_l \quad (2.3)$$

**The drift velocity:** is the velocity of component  $k$  in the frame of reference moving at the velocity equal to the total volumetric flux [5, Ch.1, p5].

$$u_{J,k} \equiv u_k - j \quad (2.4)$$

**The component mass-flux:** is the mass flow of species  $k$  divided by the total cross sectional area.

$$G_k \equiv \frac{\dot{m}_k}{A_{tot}} = u_k \rho_k \alpha_k = j_k \rho_k \quad (2.5)$$

**The total mass-flux (mass velocity):** is the sum of all the component mass-fluxes.

$$G \equiv G_g + G_l = \frac{\dot{m}_{tot}}{A_{tot}} \quad (2.6)$$

**The flowing vapor-fraction** is the mass flow rate of gas divided by the total mass flow rate [5, Ch. 1].

$$x \equiv \frac{\dot{m}_g}{\dot{m}_{tot}} = \frac{\dot{m}_g}{\dot{m}_g + \dot{m}_l} = \frac{G_g}{G_g + G_l} \quad (2.7)$$

These definitions will be used throughout the rest of this report.



## 2.3 Multiphase flow modeling

In principle, modeling two-phase flow could be the same as modeling single phase flow; Apply the transport equations to each phase and impose boundary conditions at the boundaries. What complicates the analysis of two-phase flow is the need for a new kind of boundary condition, that is at the fluid interface. This results in two main issues:

- Additional constitutive models are needed in order to describe the energy transfer, the mass transfer and the momentum transfer between the present phases.
- The interfacial boundaries are not stationary, but are moving in a complicated manner. A way to keep track of all the moving interfaces is therefore needed.

An approach like this would be very computationally expensive. This is partly because of the issues mentioned, and because an extremely fine grid is needed in all regions where an interface is present in order to capture the small scale boundary phenomena. Therefore, simplified approaches are often used. In this report, the following simplifications will be used:

- The flow will be treated as one dimensional
- The viscous term,  $\tau_{xx}$ , will be neglected
- Turbulence and axial heat transfer is not considered

Thus the following transport equations are obtained (see e.g. [29, Ch.2] and [30]):

*Continuity:*

$$\frac{\partial}{\partial t}(\alpha_k \rho_k) + \frac{\partial}{\partial x}(\alpha_k \rho_k u_k) = \Gamma_k, \quad (2.8)$$

*Momentum:*

$$\frac{\partial}{\partial t}(\alpha_k \rho_k u_k) + \frac{\partial}{\partial x}(\alpha_k \rho_k u_k^2) + \alpha_k \frac{\partial p_k}{\partial x} + (p_k - p_{ik}) \frac{\partial \alpha_k}{\partial x} = S_{m,k}, \quad (2.9)$$

*Energy:*

$$\frac{\partial}{\partial t}(\alpha_k \rho_k e_k) + \frac{\partial}{\partial x}(\alpha_k u_k (\rho_k e_k + p_k)) + p_k \frac{\partial \alpha_k}{\partial t} - (p_k - p_{ik}) \frac{\partial \alpha_k}{\partial x} u_{ik} = S_{e,k}, \quad (2.10)$$

where all quantities are evaluated as a cross-sectional average,  $p_{ik}$  is the interfacial pressure,  $e_k = e_u + 1/2u^2$ , and  $k$  takes on the values  $g$  and  $l$  representing the gas and liquid phase, respectively. This model is often referred to as the *two-fluid model*.

The terms on the right-hand side of the transport equations are sources and sinks of mass, momentum and energy. This will be discussed in further detail in Section 2.3.2.

### 2.3.1 Drift-flux model

The drift-flux model uses a priori knowledge about how the average velocity of the gas phase is related to the average velocity of the liquid phase. This is formulated as an algebraic equation, called a *slip relation*. Further, a new momentum equation is obtained by adding the two momentum equations given by (2.9). Thus, the number of differential equations are reduced by one compared to the two-fluid model and will hence be less computational expensive to solve. By doing this, source terms related to the momentum interaction between the two phases are canceled out.

The drift-flux model can be simplified by replacing additional differential equations by algebraic equations. Two drift-flux models will be presented in the next two sections where two different simplifications are made.

#### The four-equation drift-flux model (DF4)

In the four-equation drift-flux model, temperature equilibrium is assumed. Thus, one energy equation can be replaced by the following simple algebraic temperature relation,  $T_g = T_l$ . A new energy equation is obtained by adding the gas-energy equation (2.10) and the liquid-energy equation (2.10). By doing this, source terms related to the heat transfer between the two phases are canceled out. Thus, Equations (2.8)-(2.10) are reduced to<sup>1</sup> :

$$\frac{\partial}{\partial t}(\alpha_g \rho_g) + \frac{\partial}{\partial x}(\alpha_g \rho_g u_g) = \Gamma, \quad (2.11)$$

$$\frac{\partial}{\partial t}(\alpha_l \rho_l) + \frac{\partial}{\partial x}(\alpha_l \rho_l u_l) = -\Gamma, \quad (2.12)$$

$$\frac{\partial}{\partial t}(\alpha_g \rho_g u_g + \alpha_l \rho_l u_l) + \frac{\partial}{\partial x}(\alpha_g \rho_g u_g^2 + \alpha_l \rho_l u_l^2 + p) = S_{mom}, \quad (2.13)$$

$$\frac{\partial}{\partial t}(\alpha_g \rho_g e_g + \alpha_l \rho_l e_l) + \frac{\partial}{\partial x}(\alpha_g \rho_g e_g + \alpha_l \rho_l e_l + (\alpha_g u_g + \alpha_l u_l)p) = S_{heat}, \quad (2.14)$$

where  $p = \alpha_g p_g + \alpha_l p_l$ .

#### The three-equation drift-flux model (DF3)

In the three-equation drift-flux model an additional assumption is made, that is chemical-potential equilibrium. Thus, one mass-transport equation can be replaced by setting the chemical potential of the liquid phase equal to the chemical potential of the gas phase.

A new mass-transport equation is obtained by adding the two mass equation given by (2.8). By doing this, source terms related to the mass transfer between the two phases are canceled out. The system of transport equation will be quite similar to the DF4 model, except that the mass-transport equations will be replaced by the following total-mass-transport equation:

$$\frac{\partial}{\partial t}(\alpha_g \rho_g + \alpha_l \rho_l) + \frac{\partial}{\partial x}(\alpha_g \rho_g u_g + \alpha_l \rho_l u_l) = 0 \quad (2.15)$$

The complete DF3 model is thus Equation 2.13, 2.14 and 2.15.

---

<sup>1</sup>When assuming  $p_{ig} = p_{il} = p_g = p_l$

Both the DF4 model and the DF3 model can be written in the following compact vector form:

$$\mathbf{q}_t + \mathbf{f}(\mathbf{q})_x = \mathbf{s} \quad (2.16)$$

$\mathbf{q}$  will further be referred to as either the *conserved variables*, because they are conserved when the source terms are zero, or the *composite variables*.

### 2.3.2 Source-term models

The terms on the right-hand side of Equation (2.16) are sources and sinks of mass, momentum and energy. Body forces, frictional forces between the present phases and wall friction are examples of sources/sinks of momentum. Heat transfer between the phases and through the pipe walls are examples of sources of energy. Chemical reactions, condensation, and evaporation are examples of sources of mass. The source-term models are derived from a variety of fields, such as fluid mechanics, thermodynamics and heat and mass transfer. The relevant sources and how they will be modeled in this report are described below.

#### Phase transfer

The phase transfer term,  $\Gamma$  will only arise in the DF4 model. However, in the simulations preformed in this report the phase transfer will not be considered and therefore set to zero.

#### Frictional forces

In the *two-fluid model* three different friction forces have to be modeled. That is, between the wall and the gas phase, between the wall and the liquid phase, and between the gas and liquid phase. In the case of the drift-flux model only one friction force needs to be modeled, that is the total wall-friction force. Mainly the wall friction is considered in this report.

The wall friction is included on the right hand side of Equation (2.13) as:

$$S_{m,f} = \frac{\tau_w P}{A}, \quad (2.17)$$

where  $P$  is the perimeter of the pipe,  $A$  is the cross sectional area, and  $\tau_w$  is the modeled wall shear. A detailed discussion of this is found in Chapter 5.

#### Body forces

The gravitational force is the most common body force arising because of the gravitational acceleration,  $g$ , in the direction of the flow. For horizontal pipes  $g_x = 0$  and for vertical pipes  $g_x = 9.81 \text{ m/s}^2$ . The gravitational body force is included on the right hand side of Equation (2.13) as:

$$S_{m,b} = \rho g_x \quad (2.18)$$

#### Heat transfer

In the drift-flux model, the heat transfer through the wall can be modeled as a function of the overall heat transfer coefficient. The heat transfer is included on the right hand side of Equation (2.14) as:

$$S_{heat} = \frac{U \Delta T P}{A}, \quad (2.19)$$

where  $P$  is the perimeter of the pipe,  $A$  is the cross sectional area,  $U$  is the overall heat transfer coefficient, and  $\Delta T = T_{sur} - T(x)$ .

When using the two-fluid model, a model for the interfacial heat transfer is also needed.

### 2.3.3 Slip models

A *slip model* is a correlation used in the drift-flux model, which relates the *average* gas velocity to the *average* liquid velocity. The name should not be confused with the concept of *slip* in the two- and three-dimensional model, where we are dealing with *local* velocities. Be aware, in the rest of this report, the *average velocity* will be referred to as simply *the velocity*.

#### The linear slip-model

One possible simple slip-relation is the linear slip-model. It relates the liquid velocity to the gas velocity in the following way:

$$u_l = K_s u_g + S_s, \quad (2.20)$$

where  $K_s$  and  $S_s$  are slip constants.

No-slip is a special case of the linear slip-model obtained by setting  $K_s = 1$  and  $S_s = 0$ . Then the average liquid velocity and the average gas velocity are equal.

#### The Zuber-Findlay slip-model

Zuber and Findlay [41] developed the following slip model:

$$\phi = u_g - u_l = \frac{u_g(K_s - 1) + S_s}{S_s \alpha_l}, \quad (2.21)$$

where  $S_s$  is the *weighted mean drift velocity*, and  $K_s$  is the *distribution parameter* which takes into account the effects of non uniform flow.

$$K_s = \frac{\overline{\alpha j}}{\bar{\alpha} j}, \quad (2.22)$$

$$S_s = \frac{\overline{\alpha u_{j,l}}}{\bar{\alpha}}, \quad (2.23)$$

where  $u_{j,l}$  is the drift velocity of the liquid phase and  $j$  is the total volumetric flux.

There are derived several relations both for the distribution parameter and the weighted mean-drift-velocity. Possible relations, which are used in this report, are the Rouhani-Axelsson [34] correlations given by Equation (2.24) and (2.25). See also [37, Ch. 17].

$$K_s = 1 + 0.12(1 - x) \quad (2.24)$$

$$S_s = 1.18(1 - x) \left[ \frac{g\sigma(\rho_l - \rho_g)}{\rho_l^2} \right]^{1/4} \quad (2.25)$$

## 2.4 Properties of the drift-flux model

Insight into how the conserved variables are transported can be obtained by investigating the characteristic properties.

### 2.4.1 Characteristic properties

By using the chain rule, the original system given by Equation (2.16), can be rewritten in the following form<sup>2</sup>:

$$\mathbf{q}_t(x, t) + \mathbf{f}_q \mathbf{q}_x = 0, \quad (2.26)$$

where  $\mathbf{f}_q$  is called the Jacobian matrix [25].

$\mathbf{f}_q$  can further be written in terms of the right eigenvector-matrix  $\mathbf{R}$  and a diagonal matrix  $\mathbf{\Lambda}$ .

$$\mathbf{f}_q = \mathbf{R}\mathbf{\Lambda}\mathbf{R}^{-1}, \quad (2.27)$$

with

$$\mathbf{\Lambda} = \begin{bmatrix} \lambda_1 & 0 & 0 & 0 \\ 0 & \lambda_2 & 0 & 0 \\ 0 & 0 & \lambda_3 & 0 \\ 0 & 0 & 0 & \lambda_4 \end{bmatrix}, \quad (2.28)$$

where  $\lambda_i$  are the eigenvalues of the Jacobian matrix.

Further, by defining the characteristic property vector

$$\mathbf{w} = \mathbf{R}^{-1}\mathbf{q}, \quad (2.29)$$

the following system of equations can be obtained:

$$\mathbf{w}_t(x, t) + \mathbf{\Lambda}\mathbf{w}_x = 0, \quad (2.30)$$

The conserved variables,  $\mathbf{q}$ , are thus decomposed into a set of linearly independent characteristic variables,  $\mathbf{w}$ . This may be convenient, since the speed at which information travels in the characteristic system is explicitly given by the eigenvalues,  $\lambda_i$ .

How information propagates in the domain can be plotted in a time-space diagram (see Figure 2.2). Each line represents the path at which information about each characteristic property propagates. The slope of the lines are  $1/\lambda_i$ . In the DF3 model (see Section 2.3.1), four distinct regions are present in the time-space diagram. In each region the value of  $\mathbf{w}$  is constant. In region a)  $\mathbf{w} = \mathbf{w}_L$  because all information is solely coming from the initial  $\mathbf{w}_L$ . In region d)  $\mathbf{w} = \mathbf{w}_R$  because all information is solely coming from the initial  $\mathbf{w}_R$ . In region b)  $\mathbf{w} = \mathbf{w}^*$  which is a function of  $\mathbf{w}_L$  and  $\mathbf{w}_R$ , and in region c)  $\mathbf{w} = \mathbf{w}^{**}$  which is another function of  $\mathbf{w}_L$  and  $\mathbf{w}_R$ .

Further the obtained solution for the characteristic variable,  $\mathbf{w}$ , can be mapped back into the  $\mathbf{q}$ -space in order to find the solution for the conserved quantities,  $\mathbf{q}$ . In the regions where  $\mathbf{w}$  is constant,  $\mathbf{q}$  will also be constant. This means that speed of the information in the physical space is also  $\lambda_1$ ,  $\lambda_2$  and  $\lambda_3$ .

---

<sup>2</sup>When the source terms are set to zero

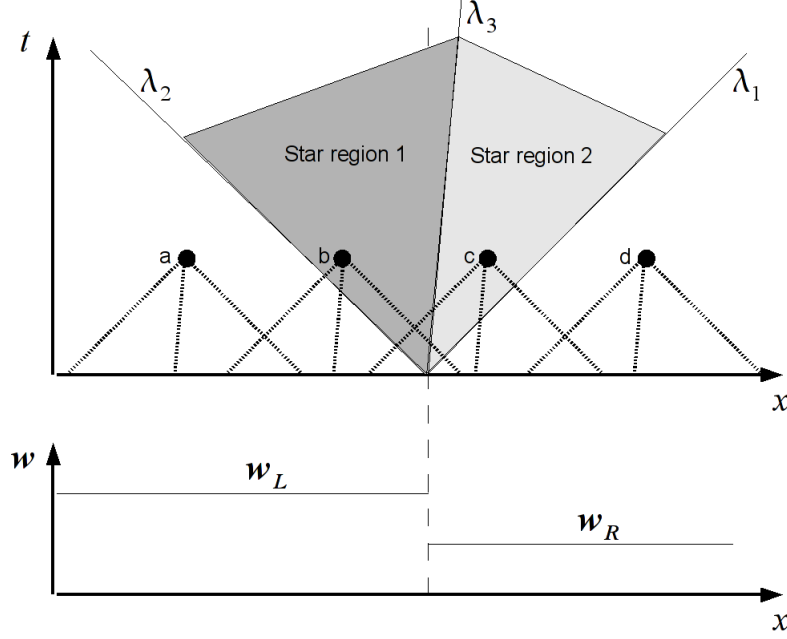


Figure 2.2: The propagation of the characteristic properties shown in a space-time diagram. This is a sketch showing how information propagates in the DF3 model

The exact same idea applies for the DF4 model. Then, four characteristic properties are present and thus four eigenvalues.

An analytical expression for the eigenvalues of the DF4 model and the DF3 model at no-slip are given below.

#### Eigenvalues for the DF4 model at no-slip conditions

In the case of no-slip conditions, Martinez et al. [15] have derived expressions for the eigenvalues in the four-equation drift-flux model.

$$\mathbf{\Lambda} = \begin{bmatrix} u - c_{DF4} \\ u \\ u \\ u + c_{DF4} \end{bmatrix}, \quad (2.31)$$

$$c_{DF4}^{-2} = (\rho_g \alpha_g + \rho_l \alpha_l) \left( \frac{\alpha_g}{\rho_g c_g^2} + \frac{\alpha_l}{\rho_l c_l^2} \right) + \frac{(\rho_g \alpha_g + \rho_l \alpha_l) C_{p,g} C_{p,l} (\zeta_g - \zeta_l)^2}{T(C_{p,g} + C_{p,l})}, \quad (2.32)$$

where  $c_{DF4}$  is the mixture speed of sound, and  $c_g$  and  $c_l$  is the speed of sound of the gas phase and liquid phase respectively.  $C_p$  is the extensive heat capacity [15]:

$$C_{p,k} = \rho_k \alpha_k c_{p,k}, \quad (2.33)$$

where

$$c_{p,k} = T \left( \frac{\partial s_k}{\partial T} \right)_p, \quad (2.34)$$

and

$$\zeta_k = \left( \frac{\partial T}{\partial p} \right)_{s_k} = -\frac{1}{\rho_k^2} \left( \frac{\partial \rho_k}{\partial s_k} \right)_p. \quad (2.35)$$

**Eigenvalues for the DF3 model at no-slip conditions**

In the case of no-slip conditions, T. Flåtten and H. Lund [17, Ch. 6] have derived expressions for the eigenvalues in the three-equation drift-flux model.

$$\mathbf{\Lambda} = \begin{bmatrix} u - c_{DF3} \\ u \\ u + c_{DF3} \end{bmatrix}, \quad (2.36)$$

where  $c_{DF3}$  is the mixture speed of sound. For details see [17, Ch. 6].

**Eigenvalues at slip conditions**

An analytical expression for the eigenvalues for the DF3 model and the DF4 model at slip conditions, is hard to obtain. However, Evje and Flåtten [14] made an estimation for the DF4 model when the energy equation is excluded.

$$\mathbf{\Lambda} = \begin{bmatrix} u_{p1} - c_{DF4*} \\ u_{p2} \\ u_{p1} + c_{DF4*} \end{bmatrix}, \quad (2.37)$$

where  $c_{DF4*}$  is the mixture speed of sound and  $u_{p1}$  and  $u_{p2}$  are average velocities. For further details see [14] and e.g. [29, App. B].

**2.4.2 Waves**

Three different categories of waves may arise in the solution of the DF3 model and the DF4 model. That are *shock waves*, *rarefaction waves* and *material waves*. The speed of each of these waves are closely related to the eigenvalues of the system. A brief description are given below. For further detail see e.g. [38, Ch. 2-3]).

**Shock wave**

A shock wave will arise if the characteristics are colliding. From the entropy condition [38, Sec. 2.4.4], the speed of the shock wave  $S_1$  is given by:

$$\lambda(\mathbf{q}_L) > S > \lambda(\mathbf{q}_R), \quad (2.38)$$

where  $\lambda(\mathbf{q}_L)$  and  $\lambda(\mathbf{q}_R)$  are the eigenvalue to the left and the right of the shock, respectively.

**Rarefaction wave**

In a rarefaction wave, the characteristics are spreading out. The speed of the rarefaction wave is thus variable with the highest speed found at the at the front of the wave,  $\lambda(\mathbf{q}_L)$ , and the lowest speed found at the tail of the wave,  $\lambda(\mathbf{q}^*)$ .

**Material wave**

The characteristics are parallel across the material wave. Thus, the speed of the material wave is identical to the relevant eigenvalue.

**In the case of subsonic flow**

In the DF4 model (see Equation (2.31)),  $\lambda_1$  is related to the rarefaction wave,  $\lambda_2$  and  $\lambda_3$  is the speed of the material waves, and  $\lambda_4$  is related to the shock wave. In the DF3 model (see Equation (2.36)), the same apply, except now, only one material wave is present.

## 2.5 Boundary conditions

Knowledge about the characteristics can be used in order to specify appropriate boundary conditions at the inlet and outlet. When an eigenvalue is positive, the characteristic variable should be specified at the western boundary, and when the characteristic is negative the characteristic variable should be specified at the eastern boundary (see Figure 2.3). However, typically it is more convenient to specify the primitive variables at the boundary rather than the characteristic variables. In order to do so, an understanding of what primitive variables are included in the different characteristics is important.

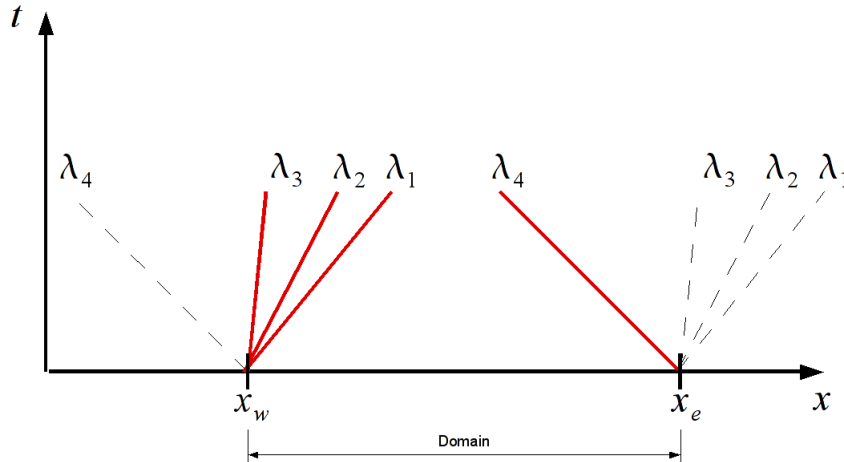


Figure 2.3: Space-time diagram. Information about the characteristics is necessary in order to set appropriate boundary conditions. In this specific case, one boundary condition should be specified at the eastern boundary and three boundary conditions should be specified at the western boundary

## 2.6 Summary

In this chapter, one-dimensional transport models are presented, in particular *a two-fluid model*, a *four-equation drift-flux* (DF4) model, and a *three-equation drift-flux* (DF3) model. In the two-fluid model, the conservation laws are applied to each phase separately. Thus, six differential equations are obtained. In the case of the drift-flux models, a priori knowledge about the slip between the present phases is used. Hence, the number of differential equations are reduced by one and the computational cost will be lower. Additional assumptions can further be made. In the DF4 model, temperature equilibrium is assumed, and in the DF3 model both temperature equilibrium and chemical-potential equilibrium are assumed.

In Section 2.3.3, two possible slip relations for the drift-flux model are presented, – that is the linear slip model, and the Zuber-Findlay slip-model. The source terms present in the transport models were briefly discussed in Section 2.3.2. Some mathematical properties of the transport models were discussed in Section 2.4, and in Section 2.5 it is demonstrated how this knowledge can be used to set appropriate boundary conditions.



# Chapter 3

## Thermodynamics

In order to solve the two-fluid model, the DF4-model or the DF3-model presented in Chapter 2.3, several thermodynamic relations, called equation of states, are needed.

We start out with some general theory related to equation of states, and further two relevant equation of states will be presented.

### 3.1 Equation of state

An equation of state (EOS) describes the relationship between state variables of a fluid. The functional relationship between the pressure, temperature and density is the most used equation of state. However, an equation relating any three state variables is an equation of state.

#### 3.1.1 State variables

A state variable is a variable that only depends on the equilibrium state of the fluid irrespective of how the fluid arrived at this specific state. Examples of thermodynamical state variables are the following: Density ( $\rho$ ), temperature ( $T$ ), pressure ( $P$ ), specific internal energy ( $e$ ) and specific entropy ( $s$ ). A combination of either of the mentioned state variables is also called a state variable. Some examples of these are:

*The specific enthalpy:*

$$h \equiv e + \frac{p}{\rho} \quad (3.1)$$

*The specific Gibbs free energy:*

$$g \equiv h - Ts \quad (3.2)$$

*The specific Helmholtz free energy:*

$$a \equiv e - Ts \quad (3.3)$$

#### 3.1.2 The fundamental equation

The thermodynamical state of a fluid can be completely characterized by knowing only two of the thermodynamical state variables. All other thermodynamical state variables can further

be derived from a fluid-specific function called *the fundamental equation*. For details see e.g [6, Ch. 3].

In this report, the fundamental equation written in terms of the specific Helmholtz free energy, will be used:

$$a = a(T, \rho) \quad (3.4)$$

### 3.1.3 Derived properties

As mentioned above, by knowing only two state variables, all other state variables can be derived from the fundamental equation and its derivatives. Using a fundamental equation written in terms of the specific Helmholtz free energy, the following definitions will be used [36]:

*Pressure*

$$p(T, \rho) \equiv \rho^2 \frac{\partial a}{\partial \rho} \Big|_T \quad (3.5)$$

*Specific entropy*

$$s(T, \rho) \equiv - \frac{\partial a}{\partial T} \Big|_\rho \quad (3.6)$$

*Specific internal energy*

$$e(T, \rho) \equiv a - T \frac{\partial a}{\partial T} \Big|_\rho \quad (3.7)$$

Further, other properties, such as specific heat and speed of sound can be found from the following definitions:

*Specific heat*

$$c_v \equiv \frac{\partial e}{\partial T} \Big|_\rho \quad (3.8)$$

*Speed of sound*

$$c^2 \equiv \frac{\partial p}{\partial \rho} \Big|_s \quad (3.9)$$

The challenge is further to find the functional form of  $a(T, \rho)$ . In the next two sections, two possible functions will be presented.

## 3.2 Span-Wagner equation of state

In 1994, Span and Wagner [36] used experimental data to construct a function for the Helmholtz free energy for CO<sub>2</sub>. This equation is now called the Span-Wagner equation of state and it predicts the states of CO<sub>2</sub> from the triple-point temperature to 1100 K and for pressures up to 800 MPa. It is a quite complicated equation containing 51 terms and is commonly used as a reference EOS for pure CO<sub>2</sub>. For details see their original paper [36].

### 3.2.1 Using the Span-Wagner EOS

#### Single phase

When only one phase is present, the Span-Wagner EOS can be used directly to find the pressure, entropy and energy either, explicitly (when the density and temperature are known),

or implicitly (if any other two state variables are known).

### Two phase (based on [21])

In the two-phase region, the gas phase and liquid phase are both present and in equilibrium. Equilibrium means that the pressure, temperature and chemical potential<sup>1</sup> are identical for the gas phase and liquid phase. In this case, the use of the Span-Wagner EOS may be more complicated because a set of equations have to be solved. In the case of the DF3 model with no slip, the mixture internal energy,  $e_{mix}$ , and mixture density,  $\rho_{mix}$ , are typically known. In order to compute  $T, \rho_g, \rho_l, e_g, e_l, P$  and  $\alpha$ , seven equations are required:

*Mixture density:*

$$\rho_{mix} \equiv \alpha \rho_g + (1 - \alpha) \rho_l \quad (3.10)$$

*Mixture internal energy:*

$$e_{mix} \equiv \frac{1}{\rho_{mix}} \left[ \alpha \rho_g e_g + (1 - \alpha) \rho_l e_l \right] \quad (3.11)$$

The internal energy for each phase is given by the Span-Wagner EOS:

$$e_k(T, \rho_k) \equiv a - T \left. \frac{\partial a}{\partial T} \right|_{\rho} \quad (3.12)$$

The pressure is given by the Span-Wagner EOS using either the liquid properties or the gas properties:

$$p(T, \rho_k) \equiv \rho_k^2 \left. \frac{\partial a}{\partial \rho_k} \right|_T \quad (3.13)$$

Since the two phases are in equilibrium, the pressure and the specific Gibbs free energy for the liquid phase and gas phase are equal

$$p(\rho_g, T) = p(\rho_l, T) \quad (3.14)$$

$$g(\rho_g, T) = g(\rho_l, T) \quad (3.15)$$

These seven variables can be solved for using an iterative procedure:

1. Guess the temperature,  $T$
2. Solve (3.14) and (3.15) for  $\rho_g$  and  $\rho_l$
3. Find the void fraction ( $\alpha$ ) from Equation (3.10)
4. Calculate the internal energy for the gas and liquid phase using (3.12)
5. Calculate the mixture internal energy  $e_{mix}$  using Equation (3.11)
6. Adjust the temperature guess based on the difference between the given  $e_{mix}$  and the result from the calculation above
7. Repeat until convergence
8. Calculate the pressure using Equation (3.14)

---

<sup>1</sup>when pressure is constant and only one species is present, the chemical potential is equal the specific Gibbs free energy

**From a phase-diagram perspective:**

Using a phase diagram, the solution procedure would be the following (see Figure 3.1):

1. Find the constant pressure line going through  $(\rho_{mix}, e_{mix})$
2. Find  $\rho_g, \rho_l, e_g$  and  $e_l$  from the diagram
3. Calculate the void fraction using Equation (3.10)

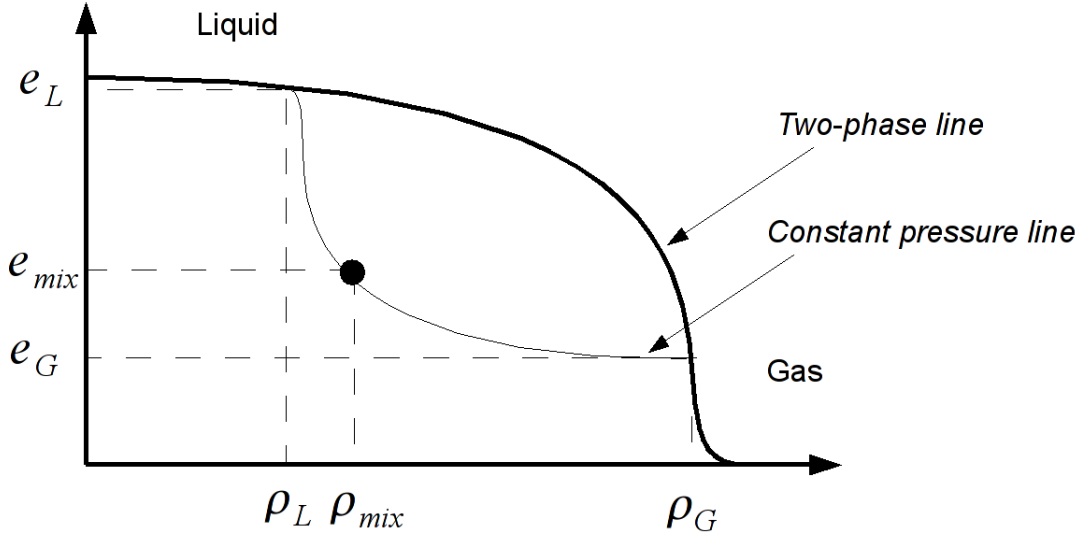


Figure 3.1: A sketch of a possible phase diagram. How to find  $T, \rho_g, \rho_l, e_g, e_l, P$  and  $\alpha$  when only  $e_{mix}$  and  $\rho_{mix}$  are known using a phase diagram.

The Span-Wagner EOS, is accurate, but it is rather complex. This is why simplified equation of states are often used. One simplified EOS is given in the next section.

### 3.3 The stiffened-gas equation of state

The stiffened-gas equation of state [26] is a simple EOS which often is used to describe denser gasses and compressible liquids. It is defined by the following expression for the Helmholtz free energy:

$$a(\rho, T) = c_v T (1 - \ln(T/T_0) + (\gamma - 1) \ln(\rho/\rho_0)) - s_0 T + \frac{p_\infty}{\rho} + e_0, \quad (3.16)$$

where  $c_v, \gamma, p_\infty, T_0, \rho_0, s_0$  and  $e_0$  are constants. By making use of the definitions given in Section 3.1.3 for the pressure and energy, the following is obtained:

$$p(\rho, T) = \rho(\gamma - 1)c_v T - p_\infty, \quad (3.17)$$

$$e(\rho, T) = c_v T + \frac{p_\infty}{\rho} + e_0, \quad (3.18)$$

and

$$s(\rho, T) = c_v \ln \left[ \frac{T}{T_0} \left( \frac{\rho_0}{\rho} \right)^{\gamma-1} \right]. \quad (3.19)$$

### 3.3.1 Parameter fitting

The parameters in the stiffened-gas EOS can be specified according to a specific fluid and a specific reference state  $(P_0, T_0)$ . The constant parameters in the case of  $\text{CO}_2$  can for instance be set by making use of the Span-Wagner EOS. Hence,  $c_v = c_v(P_0, T_0)$  and  $\gamma = \gamma(P_0, T_0)$ . Further,  $p_\infty$  can be computed by rearranging Equation (3.17).

However, if a correct prediction of the wave speeds are important, an alternative procedure suggested by Flåtten and Lund [16] can be used:

#### The speed of sound procedure [16]:

According to the stiffened gas equation of state the speed of sound is:

$$c^2 = (\gamma - 1)c_p T \quad (3.20)$$

For details see Appendix E

The constant parameters of Equation (3.16) can be obtained the following way:

1. Define a reference state ( $P_0$  and  $T_0$ )
2. Use experimental data or results obtained with the Span-Wagner EOS to find the value of  $\rho$ ,  $c_{p,0}$  and  $c_0$
3. Use Equation (3.20) and solve for  $\gamma$
4. Solve for  $c_v$  by using the following definition;  $\gamma = c_p/c_v$
5. Rearrange Equation (3.17) and solve for  $p_\infty$

## 3.4 Summary

In this chapter we have introduced the concept of an equation of state. In Section 3.1.3 we saw how equations of state could be derived from the fundamental equation. Further, two possible functional forms of the fundamental relations were presented in Section 3.2 and 3.3. Those were the Span-Wagner EOS and the stiffened-gas EOS.



# Chapter 4

## Numerical methods

In this Chapter, the numerical methods for solving the two-phase transport model given by Equation (2.16), will be presented.

First, the fundamentals about the finite-volume approach is presented. Further, the MUSTA method will be described in details.

### 4.1 Finite-volume methods

In order to solve a differential equation using the finite-volume approach, the domain of interest is first divided into a set of finite volumes. The midpoint in each finite volume is assigned a property value  $Q_i^n$  which corresponds to the average value of  $q$  within the specific finite volume at time step  $n$  (see Equation (4.1) and Figure 4.1).

$$Q_i^n = \frac{1}{\Delta x} \int_{x_{i-1/2}}^{x_{i+1/2}} q(x, t_n) dx \quad (4.1)$$

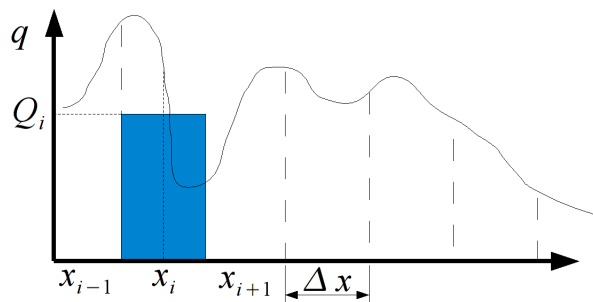


Figure 4.1: Each finite volume is assigned a value  $Q_i$  at its midpoint ( $x_i$ ).  $Q_i$  corresponds to the average value of  $q$  within the specific finite volume.

Further, the differential equations, given by (2.16), have to be discretized. By integrating Equation (2.16) over each finite volume, a discrete expression for  $Q_i$  at time step  $n$ , can be derived [25, Ch. 4]. Thus, the following is obtained:

$$\int_{\Delta x_i} \left[ \frac{\partial}{\partial t} \mathbf{q} + \frac{\partial}{\partial x} \mathbf{f}(\mathbf{q}) \right] dx_i = \int_{\Delta x_i} \mathbf{s} dx_i, \quad (4.2)$$

and hence

$$\frac{\partial}{\partial t} \int_{\Delta x_i} \mathbf{q} dx_i + \int_{\Delta x_i} \frac{\partial}{\partial x} \mathbf{f}(\mathbf{q}) dx_i = \int_{\Delta x_i} \mathbf{s} dx_i. \quad (4.3)$$

Using the definition given by Equation (4.1), we get:

$$\Delta x \frac{\partial}{\partial t} \mathbf{Q}_i + [\mathbf{f}(\mathbf{q}(x_{i+1/2}, t)) - \mathbf{f}(\mathbf{q}(x_{i-1/2}, t))] = \Delta x \mathbf{S}_i, \quad (4.4)$$

$$\frac{\partial}{\partial t} \mathbf{Q}_i = \frac{\mathbf{F}_{i-1/2}^n - \mathbf{F}_{i+1/2}^n}{\Delta x} + \mathbf{S}_i, \quad (4.5)$$

where the following notation is used:  $\mathbf{F}_i^n = \mathbf{f}(\mathbf{q}(x_i, t))$ . Further, the explicit forward Euler scheme is used for time discretization:

$$\frac{\partial \mathbf{Q}}{\partial t} \approx \frac{\mathbf{Q}^{n+1} - \mathbf{Q}^n}{\Delta t} \quad (4.6)$$

Thus the following discretized equation is obtained:

$$\boxed{\mathbf{Q}_i^{n+1} = \mathbf{Q}_i^n + \frac{\Delta t}{\Delta x} (\mathbf{F}_{i-1/2}^n - \mathbf{F}_{i+1/2}^n) + \Delta t \mathbf{S}_i} \quad (4.7)$$

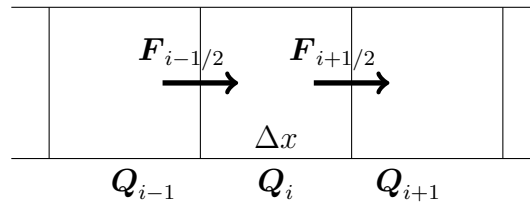


Figure 4.2: An illustration of Equation (4.7) where the source term,  $\mathbf{S}_i$ , is neglected. As seen, the value of  $\mathbf{Q}_i$  changes due to the fluxes at the interface at  $i + 1/2$  and  $i - 1/2$ .

The flux,  $\mathbf{F}$ , is a function of  $\mathbf{q}$ . However, no information is given about  $\mathbf{q}$  at the cell interface ( $i + 1/2$  and  $i - 1/2$ ). Thus, the challenge of using the method given in Equation (4.7) is the estimation of the fluxes  $\mathbf{F}_{i+1/2}$  and  $\mathbf{F}_{i-1/2}$ .

There exist many different finite-volume methods. The way the flux is estimated defines the method. In Section 4.3 one possible estimation of the flux will be presented.

## 4.2 The Courant-Friedrichs-Levy number

The Courant-Friedrichs-Levy (CFL) number is a dimensionless number defined as:

$$\text{CFL} = \frac{|\lambda|_{\max} \Delta t}{\Delta x}, \quad (4.8)$$



where  $|\lambda|_{max}$  is the absolute value of the maximum eigenvalue in the domain for the given system of equations.

Typically, the CFL-number has to be smaller than 1 in an explicit numerical method in order to assure stability. Physically, this means that the distance traveled by a wave during a time interval of  $\Delta t$  has to be smaller than the resolution of the grid ( $\Delta x$ ).

By specifying the CFL number, the length of the time step used in numerical calculations can be computed.

## 4.3 Flux estimation

There are several ways in which the flux can be estimated. In this report the multi-stage (MUSTA) method will be used.

### 4.3.1 The MUSTA method

The MUSTA method proposed by Toro [39] is aimed at coming close to the accuracy of upwind schemes while retaining the simplicity of a centered scheme [29, Sec. 8.1.3]. The method does not make use of the wave-propagating information in the equations. Thus, it can more easily be applied to more complicated systems of equations like many multi-phase flow transport-models, where the eigenstructure is hard to obtain.

The MUSTA flux at the interface is approximated by performing several sub time-steps using a simple first-order centered flux on a local grid. The first-order centered flux used in this report is the FORCE flux.

#### The FORCE flux

The FORCE flux is given as the arithmetic mean of the Richtmyer and Lax-Friedrichs scheme [38, Sec. 7.4.2]:

$$\mathbf{F}_{i+1/2}^{\text{FORCE}} = \frac{1}{2}(\mathbf{F}_{i+1/2}^{\text{RI}} + \mathbf{F}_{i+1/2}^{\text{LF}}), \quad (4.9)$$

where the Lax Friedrichs scheme is [38, Sec. 5.3.4]

$$\mathbf{F}_{i+1/2}^{\text{LF}} = \frac{1}{2}(\mathbf{F}_i^n + \mathbf{F}_{i+1}^n) + \frac{1}{2} \frac{\Delta x}{\Delta t} (\mathbf{Q}_i^n - \mathbf{Q}_{i+1}^n), \quad (4.10)$$

and the Richtmyer scheme is [38, Sec. 5.3.4]

$$\mathbf{F}_{i+1/2}^{\text{RI}} = \mathbf{F}(\mathbf{Q}_{i+1/2}^{n+1/2}), \quad (4.11)$$

where

$$\mathbf{Q}_{i+1/2}^{n+1/2} = \frac{1}{2}(\mathbf{Q}_i^n + \mathbf{Q}_{i+1}^n) + \frac{1}{2} \frac{\Delta t}{\Delta x} (\mathbf{F}_i^n - \mathbf{F}_{i+1}^n), \quad (4.12)$$

and where  $\mathbf{F}_i^n$  is short hand notation for  $\mathbf{F}(\mathbf{Q}_i^n)$ .

**The MUSTA procedure (based on [29, Sec. 8.2.2])**

The MUSTA flux (see Figure 4.3a) is computed the following way:

1. Define a temporary local grid consisting of  $2N$  cells where the cell-value,  $Q_j$ , is set to:

$$Q_j = \begin{cases} Q_i, & \text{if } 1 \leq j \leq N \\ Q_{i+1}, & \text{if } N < j \leq 2N \end{cases}, \quad (4.13)$$

where  $j$  is the index for the local grid and  $i$  is the index for the global grid. See Figure 4.3b.

2.  $M$  time-steps are carried out on the local grid using the first-order centered flux given by Equation (4.9). See Figure 4.3c. The local solution at time step  $m + 1$  is found using:

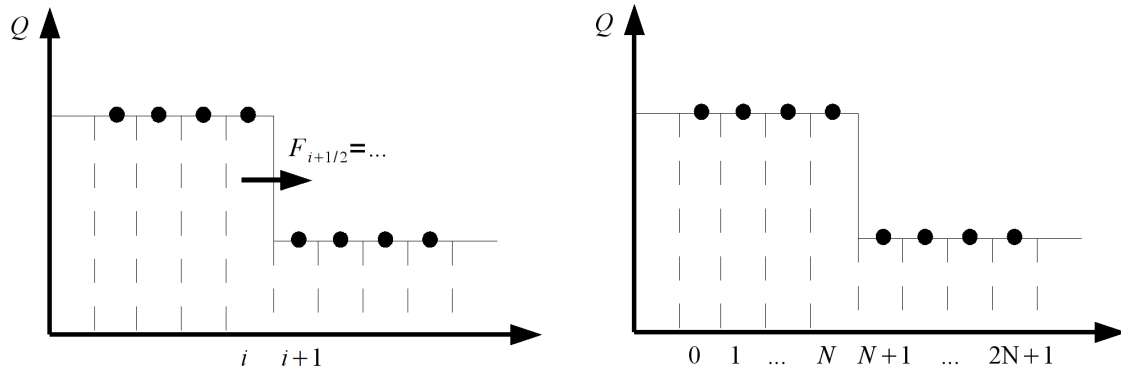
$$Q_j^{m+1} = Q_j^m + \frac{\Delta t_{loc}}{\Delta x} (F_{j-1/2}^m - F_{j+1/2}^m), \quad (4.14)$$

where  $\Delta t_{loc}$  is the time-step length used at the local grid, which may be different from the global time-step length ( $\Delta t$ ).

3. The first-order centered-flux calculated on the local grid at time step  $M$  in the local-grid-cell number  $N + 1/2$  is defined as the MUSTA flux. This is further used as the flux on the global grid in Equation (4.7). See Figure 4.3d.

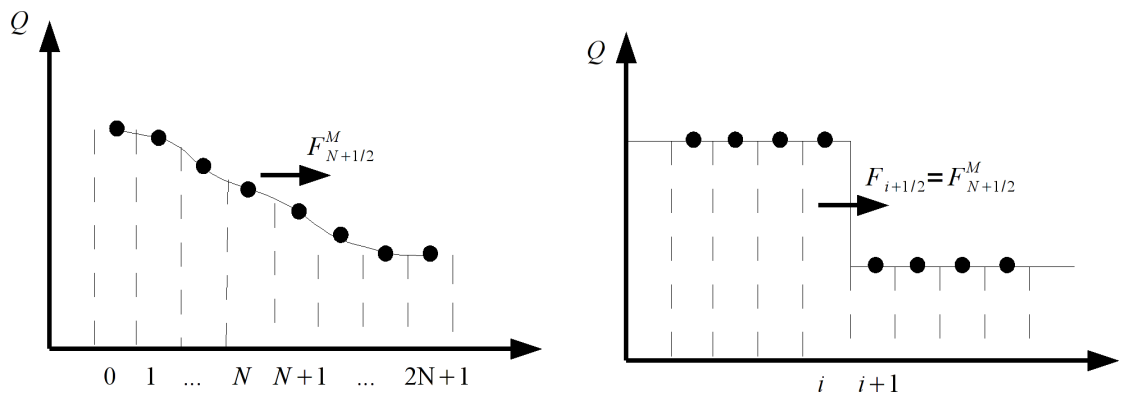
In order to avoid interference from the boundaries in the local grid, the number of sub-steps,  $M$ , should be smaller or equal to the number of local cells,  $2N$  [29, Sec. 8.4].

The local time step  $\Delta t_{loc}$  is calculated using Equation (4.8). However, now the *local* maximum eigenvalue is used.



(a) Global grid: The MUSTA flux,  $F_{i+1/2}$  is initially unknown.

(b) Definition of a local grid.



(c)  $M$  time steps are carried out on the local grid using a first-order centered scheme.

(d) Back to the global grid: The flux calculated on the local grid at time step  $M$  is defined as the MUSTA flux.

Figure 4.3: The MUSTA procedure

## 4.4 Summary

In this Chapter, the numerical method used to solve the two-phase transport model given in Chapter 2.3.1 is presented. A finite volume method is used. The time discretization is done using the explicit forward Euler and the MUSTA method is used for spatial discretization.



# Chapter 5

## Frictional forces

The modeling of the frictional pressure-drop in the one-dimensional two-phase transport-models from Section 2.3, will be discussed. How the friction is modeled in a single-phase flow will be explained in Section 5.1. Then, possible ways to model the friction in two-phase flow will be presented in Section 5.2. The friction models which will be used throughout the rest of this report will be presented in Section 5.3.

### 5.1 Friction modeling in single-phase flow

In order to understand how the friction is modeled in a single-phase flow, it may be convenient to imagine that a control volume is placed around the flow (see Figure 5.1). The wall friction can be recognized as an external force acting on the control volume.

$$F_w = \tau_w P \Delta x, \quad (5.1)$$

where  $P$  is the perimeter of the pipe and  $\Delta x$  is the length of the control volume. The wall shear tension  $\tau_w$  is typically modeled the following way:

$$\tau_w = f \frac{\rho u^2}{8}, \quad (5.2)$$

where  $f$  is the Darcy friction factor and  $u$  is the mean velocity computed as:  $u = \dot{m}_{tot}/(\rho A)$ . Relations for the Darcy friction factor will be given in the next section.

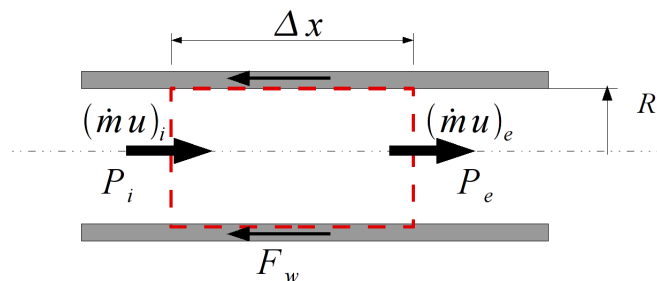


Figure 5.1: The friction force,  $F_w$ , is an external force acting on the control volume (the red dotted line).

Since the momentum equation given by (2.13), consists of cross-sectional-averaged terms, the effect of wall friction will appear as a source term in (2.13) on the following form:

$$S = \frac{\tau_w P}{A}, \quad (5.3)$$

where  $P$  is the perimeter of the pipe, and  $A$  is the cross-sectional area.

### 5.1.1 Darcy friction-factor relations

The Darcy-friction factor is an important parameter in the friction relations. It is a function of several fluid and flow properties. In this section, some of the most commonly used correlations will be presented.

#### Laminar flow:

An analytical solution for the Darcy friction factor can be obtained for a laminar fully developed flow [40, Ch. 6].

$$f = \frac{64}{\text{Re}} \quad (5.4)$$

#### Turbulent flow,– smooth pipes:

Prandtl derived the following equation for  $f$  which is now the accepted formula for turbulent flow in smooth pipes [40, Ch.6]:

$$\frac{1}{f^{1/2}} = 2.0 \log(\text{Re} f^{1/2}) - 0.8 \quad (5.5)$$

However, this equation is cumbersome to solve for  $f$ . Therefore alternative approximation of this formula is often used. One of the most famous approximations are given by Blasius (be aware that it has a limited range of applicability).

$$f = \frac{0.316}{\text{Re}^{0.25}}, \quad 4000 < \text{Re} < 10^5 \quad (5.6)$$

An alternative formula is used by Friedel [20]. It satisfy a smooth transition from the laminar friction factor given by Equation (5.4).

$$f = \left( 0.86859 \ln \left[ \frac{\text{Re}}{1.964 \ln \text{Re} - 3.8215} \right] \right)^{-2}, \quad \text{Re} > 1055 \quad (5.7)$$

#### Turbulent flow,– rough pipes:

The roughness of the pipe will strongly affect the frictional pressure-drop of a turbulent flow [40, Ch. 6]. The following correlation made by Colebrook is now the accepted formula for rough pipes:

$$\frac{1}{f^{1/2}} = -2.0 \log \left[ \frac{\epsilon/d}{3.7} + \frac{2.51}{\text{Re} f^{1/2}} \right] \quad (5.8)$$

In order to avoid iteration, Haaland made an approximation to the Colebrook relation as follows:

$$\frac{1}{f^{1/2}} = -1.8 \log \left[ \left( \frac{\epsilon/d}{3.7} \right)^{1.11} + \frac{6.9}{\text{Re}} \right], \quad (5.9)$$

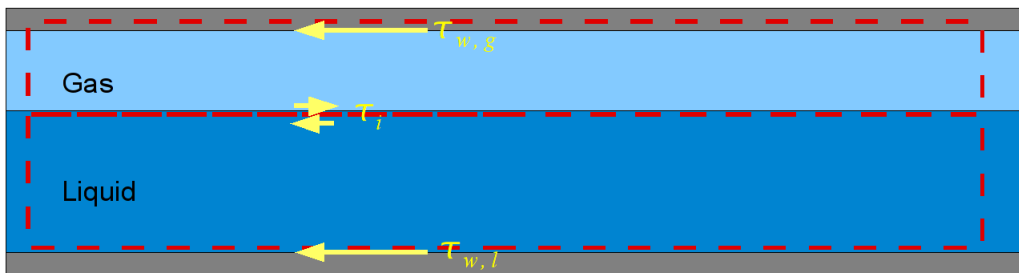
where  $\epsilon$  is the pipe wall roughness. Equations (5.8) and (5.9), can also be used for smooth pipes by setting  $\epsilon = 0$ .

It should be noted that for the transition region,  $2000 < \text{Re} < 4000$ , there does not exist any reliable friction correlations [40]. Nevertheless, either the turbulent assumption or the laminar assumption is often used in this region.

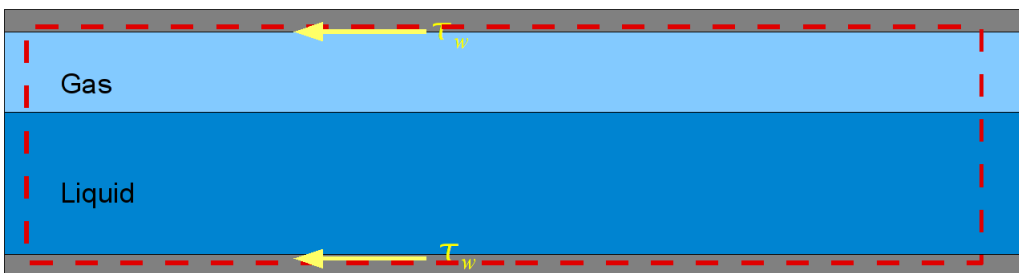
## 5.2 Friction modeling in two-phase flow

The starting point of modeling the frictional forces in a two-phase flow is exactly the same as in single-phase flow. A control-volume analysis is performed and the friction forces acting on the control volume are determined. In the case of the drift-flux model, only one momentum equation is used. Hence a control volume can be placed around the total mixture, and the only external force acting, can be recognized as the wall friction. In the case of the two-fluid model, two momentum equations are used. In this case, a control volume can be placed around each phase and hence three external forces are recognized; the friction between the gas and the wall, the friction between the liquid and the wall, and the interfacial friction between the gas phase and liquid phase (see Figure 5.2).

Only the modeling of the friction forces in the drift-flux model, that is the total wall-friction, will be considered in further details.



(a)



(b)

Figure 5.2: a) In the two-fluid model, momentum conservation is applied to each phase separately, thus the liquid wall-shear, gas wall-shear, and the interfacial shear has to be modeled. b) In the drift-flux model, the momentum equation is applied to the total mixture, thus only the total wall shear has to be modeled.

In the case of the drift-flux model, only the total wall-friction has to be modeled. This is typically done using three different approaches:

- The homogeneous approach
- The two-phase multiplier approach
- The flow-pattern dependent approach

In a *homogenous model*, the two-phase mixture is treated as a pseudo single-phase-fluid. The pseudo-fluid properties are defined as an average of the properties of the gas phase and liquid phase. Further, the frictional pressure-drop is found by inserting the mixture properties in the single-phase relations presented in the Section 5.1.

Often the two-phase frictional-pressure-drop is modeled by introducing a *two-phase friction-multiplier*. The idea is that the two-phase frictional pressure-drop is equal to the single-phase frictional-pressure drop<sup>1</sup>, multiplied with a factor  $\Phi^2$ .

$$S_{mf} = \Phi^2 S_{sf} \quad (5.10)$$

The two-phase multiplier is a function which is suppose to take into account the flow-pattern-dependent behavior of the friction.

A *flow-pattern dependent approach* consist of two separate models; a model that predicts the flow-pattern and a friction-model. First the flow pattern must be determined, further the corresponding frictional pressure-drop correlation is used.

## 5.3 Selected wall-friction models

In this section, the wall-friction models which will be used throughout this report are presented. Based on the conclusions in the pre-master project [2], the two-phase multiplier model of Friedel [20] and the the flow-pattern dependent model of Cheng et al. [8] are considered to be the most promising friction models for CO<sub>2</sub> pipe flows. In addition, a very simple homogeneous model is presented as a comparison to the two more sophisticated models.

### 5.3.1 A homogeneous model

In the homogenous model used in this report, the following definitions of the mixture density, mixture viscosity [10, Sec. 2.3.2] and mean velocity are used:

$$\rho_{mix} = \left( \frac{x}{\rho_g} + \frac{1-x}{\rho_l} \right)^{-1} \quad (5.11)$$

$$\mu_{mix} \left( \frac{x}{\mu_g} + \frac{1-x}{\mu_l} \right)^{-1} \quad (5.12)$$

$$\bar{u} = \frac{G}{\rho_{mix}} \quad (5.13)$$

---

<sup>1</sup>when the given total mass flux,  $G$ , is considered to flowing as liquid-only or gas-only.



These definitions are used in the following frictional pressure-drop relations:

For *laminar flow* ( $Re < 2000$ ):

$$f = \frac{64}{Re} \quad (5.14)$$

For *turbulent flow* ( $Re \geq 2000$ ):

$$f = \left[ 1.8 \log \left( \frac{Re}{6.9} \right) \right]^{-2}, \quad (5.15)$$

which is the smooth-pipe assumption applied to Equation (5.9).

Since neither the Friedel model or the Cheng et al. model are functions of the roughness, a homogenous model which uses the same assumption has been considered.

### 5.3.2 The Friedel model

The Friedel [20] correlation is a model based on the two-phase multiplier idea. It is a curve fit of 25 000 frictional-pressure-drop measurements at various single phase and two-phase conditions. The correlation takes into account the following variables: flow direction (vertical upward, vertical downward, horizontal), mass velocity, flowing vapor-fraction, hydraulic diameter, cross-section geometry (annular, circular, rectangular), pipe length, gravitational acceleration, and fluid properties, such as density, viscosity, and surface tension. The effect of wall roughness is considered to be neglectable [20].

#### Data used for the horizontal two-phase flow

Most of the experiments are carried out using air-water and air-oil flows in circular tubes. The distribution of the fluid properties used in the experiments are extremely nonuniform. In order to get an idea of the applicability of the correlation, the range and arithmetic mean of the experimental data used are listed in Table 5.1.

Table 5.1: The table shows the the range and arithmetic mean of the experimental data used in the development of the Friedel correlation [20]. The single-component flows are a two-phase mixtures where the gas phase and the liquid phase consist of the same species. The two-component flows are two-phase flows where the gas phase and liquid phase consist of two different species.

Variables		Single component		Two component	
		Range	Mean	Range	Mean
Mass flow rate [kg/m <sup>2</sup> s]	$G$	7–4500	674	2–10330	885
Density ratio	$\rho_l/\rho_g$	4–49070	1541	8–120	428
Pressure [bar]	$p$	0.02–178	20	1–64	10
Flowing vapor-fraction	$x$	0–1	0.35	0–1	0.26
Hydraulic diameter [mm]	$d$	4–200	27	1–154	49
Viscosity ratio,	$\mu_l/\mu_g$	2–46	17	13–33620	444
Surface tension [ $10^{-3}$ N/m]	$\sigma$	2–92	36	20–76	53

**Model**

The frictional pressure-drop predicted by Friedel [20] is:

$$S_{mf} = \Phi^2 S_l, \quad (5.16)$$

where

$$S_l = \frac{f_l G^2}{2d\rho_l}. \quad (5.17)$$

In the original paper of Friedel, the Darcy-friction factor,  $f_l$ , is evaluated using Equation (5.7). Nevertheless, the Blasius correlation is most commonly used (see e.g. [37, Ch. 13]):

$$f_l = \frac{0.316}{\text{Re}_l^{0.25}}, \quad (5.18)$$

where the following definition of the Reynolds number is used:

$$\text{Re}_l = \frac{Gd}{\mu_l} \quad (5.19)$$

The two-phase friction multiplier is:

$$\Phi^2 = E + \frac{3.24FH}{\text{Fr}_h^{0.045} \text{We}_l^{0.035}}, \quad (5.20)$$

where the functions  $E$ ,  $F$  and  $H$  are defined as:

$$E = (1 - x)^2 + x^2 \frac{\rho_l f_g}{\rho_g f_l}, \quad (5.21)$$

$$F = x^{0.78} (1 - x)^{0.224}, \quad (5.22)$$

and

$$H = \left(\frac{\rho_l}{\rho_g}\right)^{0.91} \left(\frac{\mu_g}{\mu_l}\right)^{0.19} \left(1 - \frac{\mu_g}{\mu_l}\right)^{0.7}. \quad (5.23)$$

The Froud number, which indicate the relative importance of inertia compared to gravitational forces is

$$\text{Fr}_h = \frac{G^2}{gd\rho_h^2}. \quad (5.24)$$

The Weber number, which indicate the relative importance of inertia compared to surface tension is

$$\text{We}_l = \frac{G^2 d}{\sigma \rho_h}, \quad (5.25)$$

and the homogenous (or average) density is

$$\rho_h = \left(\frac{x}{\rho_g} + \frac{1-x}{\rho_l}\right)^{-1}. \quad (5.26)$$

### 5.3.3 The Cheng et al. model

Cheng et al. [8] have developed a frictional pressure-drop model specifically for CO<sub>2</sub>. Throughout this report, this model will be referred to as *the Cheng et al. model*. In contrast to the Friedel model, the Cheng et al. model is a flow-pattern dependent model. Thus it also includes a model in order to determine the flow pattern as well as friction-correlations. The model is derived based on the experimental data listed in Table 5.2.

Table 5.2: The flow pattern map of Cheng et al. is applicable for the following range of flow conditions [8, Tab.1][9, Tab.1]

Variables		Flow-pattern model	Friction model
Tube diameter [mm]	$d$	0.6 – 10	0.8 – 7
Mass velocity [kg/m <sup>2</sup> s]	$G$	80 – 1500	200 – 400
Heat flux [kW/m <sup>2</sup> ]	$q''$	5 – 46	3–15
Saturation temperature [° C]	$T_{sat}$	-28 – 25	-25 – 20
Reduced pressure	$p/p_{crit}$	0.21 – 0.87	0.21 – 0.78

Cheng et al. categorize the flow into eight different flow patterns:

- S - Stratified flow
- SW - Stratified-wavy flow
- SWS - Stratified-wavy and slug flow
- I - Intermittent flow (plug flow)
- B - Bubbly flow
- A - Annular flow
- D - Dry-out flow
- M - Mist flow

The flow-pattern model of Cheng et al. takes the form as a flow-pattern map and may look like the one in Figure 5.3.

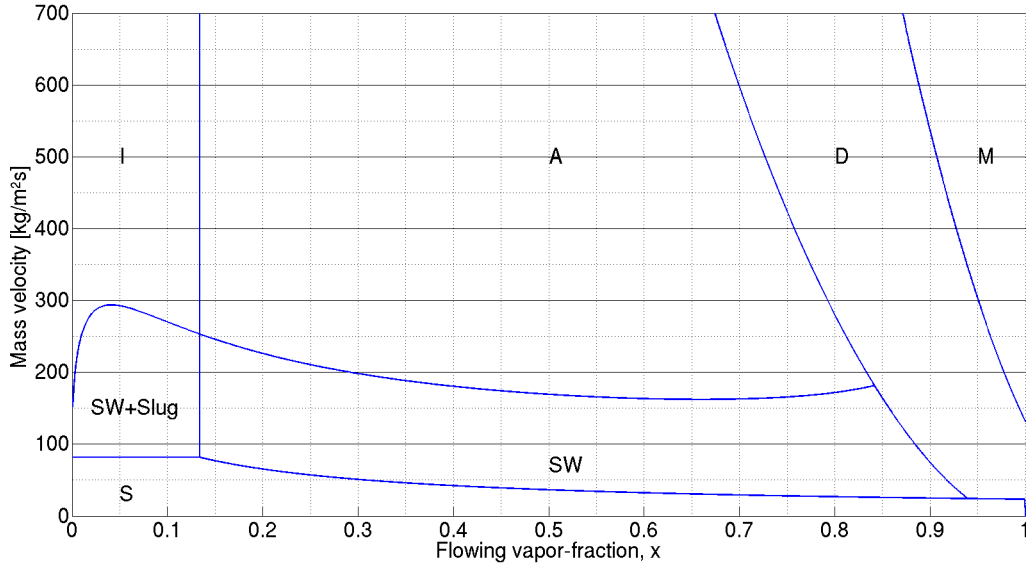


Figure 5.3: An example of what the flow-pattern map of Cheng et al. may look like.

Transition lines (which depends on fluid properties) separates different regions in the map. Further the flow pattern can be determined based on the total mass flow rate,  $G$ , and the vapor fraction,  $x$ .

The equations for the transition lines and the friction correlations for each flow pattern are found in the original paper of Cheng et al. [8].

Be aware that one specific slip-relation is assumed in the Cheng et al. model. That is the Rouhani-Axelsson version of the Zuber-Findlay slip model. The slip relation is incorporated in the void-fraction correlation used in [8] and is given by Equation 5.27. For details see Appendix A.

$$\alpha = \frac{x}{\rho_g} \left[ (1 + 0.12(1 - x)) \left( \frac{x}{\rho_g} + \frac{1 - x}{\rho_l} \right) + \frac{1.18(1 - x)[g\sigma(\rho_l - \rho_g)]^{1/4}}{G\rho_l^{1/2}} \right]^{-1} \quad (5.27)$$

### Corrections

During the implementation of the Cheng et al. model, certain errors were found in the paper of Cheng et al. [8]. After several discussions with Dr. Cheng [7], the following equations were corrected:

- The power of 0.02 in Equation (40) in [8] should be removed such that:

$$f_{SW} = \theta_{dry}^* f_v + (1 - \theta_{dry}^*) f_a \quad (5.28)$$

- It should be clarified that Equation (14), in [8], should be used in *all* calculation of  $G_{wavy}$  in Equation (42), in [8].

- One parenthesis is missing in Equation (13) in [8]. The correct version is found in Biberg's paper [4, Eq. (14)].
- The frictional pressure-drop in the mist region, Equation (48) in [8], should only be used for mass flow rates higher than 150 kg/m<sup>2</sup>s. For lower mass flow rates, the mist relation developed by Thome and Quiben should be used [33, Eq. (22)].

## 5.4 Summary

In this Chapter, the modeling of the friction term in Equation (2.13) was discussed. In Section 5.1 the most common friction correlations for single-phase flow is presented. In the case of two-phase flow, what friction terms needs to be modeled depends the transport model used, – In the *the two-fluid model* both the wall-friction and the interfacial friction must be modeled, and in the *drift-flux model* only the total wall-friction must be modeled. Three wall-friction models using three different approaches were presented; A *homogenous model*, the *two-phase multiplier model* by Friedel, and the *flow-pattern-dependent model* by Cheng et al. The model of Friedel [20] is considered to be promising because it is developed based on a large amount of experimental data, the Cheng et al. model [8] is considered to be promising because it is developed specifically for CO<sub>2</sub>, and the homogenous model is a very simple approach used as a comparison to the two more sophisticated models.



## Part II

# MATERIAL AND MODEL IMPLEMENTATION





# Chapter 6

## Friction-model implementation

The Friedel model, the homogenous model, and the The Cheng et al. model have been implemented in a separate program-code (used in Chapter 9), and later in the COTT code (used in Chapter 10 and 11). The separate program-code will further be referred to as *the MATLAB code*. The implementation of the Friedel model and the homogenous model are relatively straight forward, thus only the Cheng et al. model will be considered here.

### 6.1 The MATLAB-code

A program code has been written in order to determine the flow pattern and further the frictional pressure-drop using the Cheng et al. model. The idea behind the program code can be found in Appendix H.

### 6.2 Verification

In order to verify the implemented code, a comparison is made with results provided by Dr. Cheng. The test conditions used are found in Table 6.1 and the corresponding property values are found in Table 6.2.

Table 6.1: Test conditions

Mass velocity [kg/m <sup>2</sup> s]	$G$	400 and 150
Saturated temperature [°C]	$T_{sat}$	-10
Diameter [mm]	$d$	7
Heat flux [kW/m <sup>2</sup> ]	$q''$	10

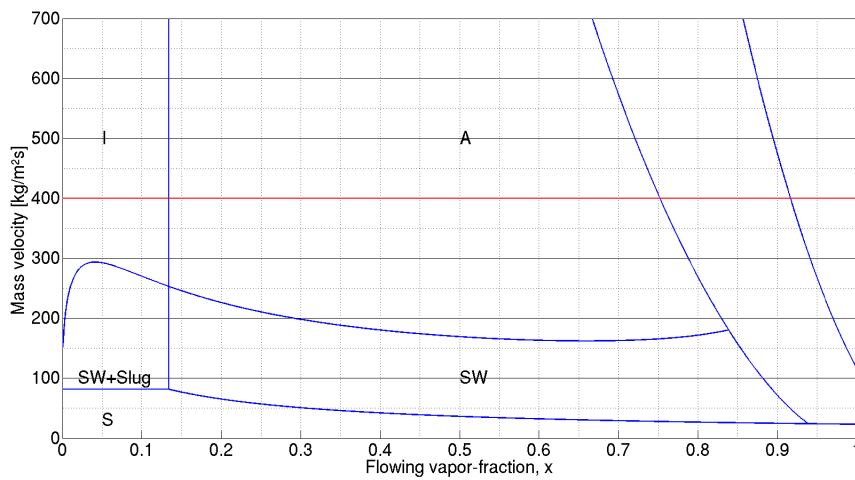
Table 6.2: Saturation properties at  $T_{sat} = -10^\circ$  C obtained from NIST [1].

		<b>Gas phase</b>	<b>Liquid phase</b>
Density [kg/m <sup>3</sup> ]	$\rho$	71.185	982.93
Viscosity [N/m <sup>2</sup> s]	$\mu$	$1.3863 \cdot 10^{-5}$	$11.802 \cdot 10^{-5}$
Enthalpy [kJ/kg]	$h$	435.14	176.52

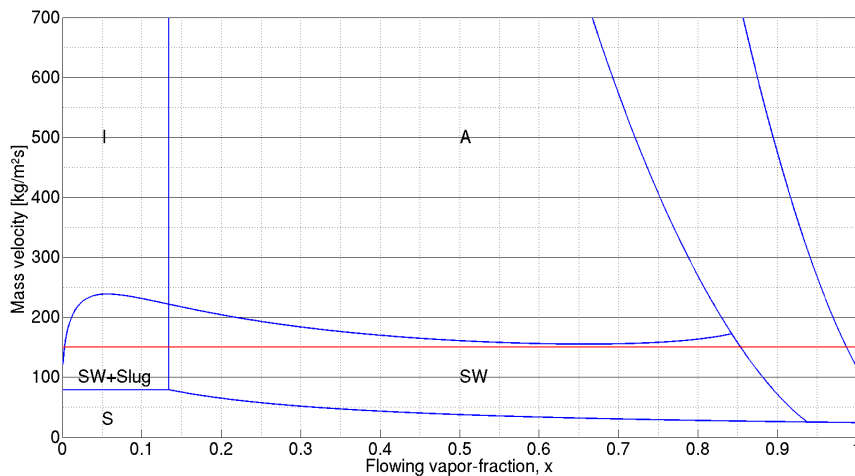
The heat of vaporization is  $h_{lg} = h_g - h_l = 258.62$  kJ/kg, and the surface tension is  $\sigma = 0.0064953$  N/m.

### 6.2.1 Results

Flow-pattern maps generated by the MATLAB code for the given test conditions are shown in Figure 6.1. The frictional pressure-drop is further calculated for the conditions along the horizontal red line shown in each flow-pattern map. The results both from the MATLAB code (referred to as Aakenes) and from Dr. Cheng are shown in Figure 6.2. As seen from the plot, the results are in good agreement. The small differences are expected to be due to difference in the fluid-property models. In this report NIST Web-Book is used while Dr. Cheng has used the NIST 6 software [7].



(a)  $G = 400$  kg/m<sup>2</sup>s

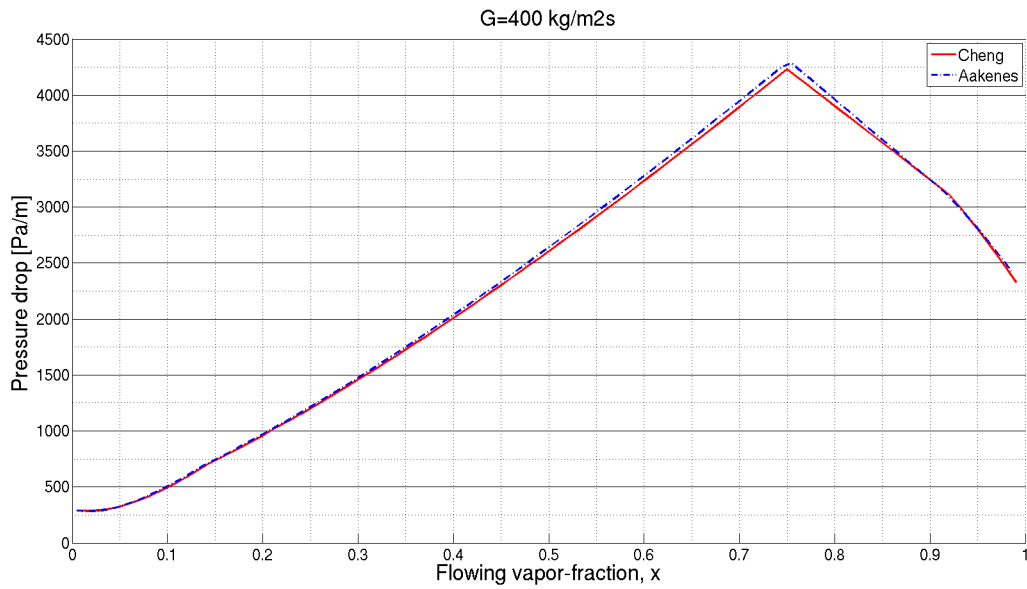


(b)  $G = 150$  kg/m<sup>2</sup>s

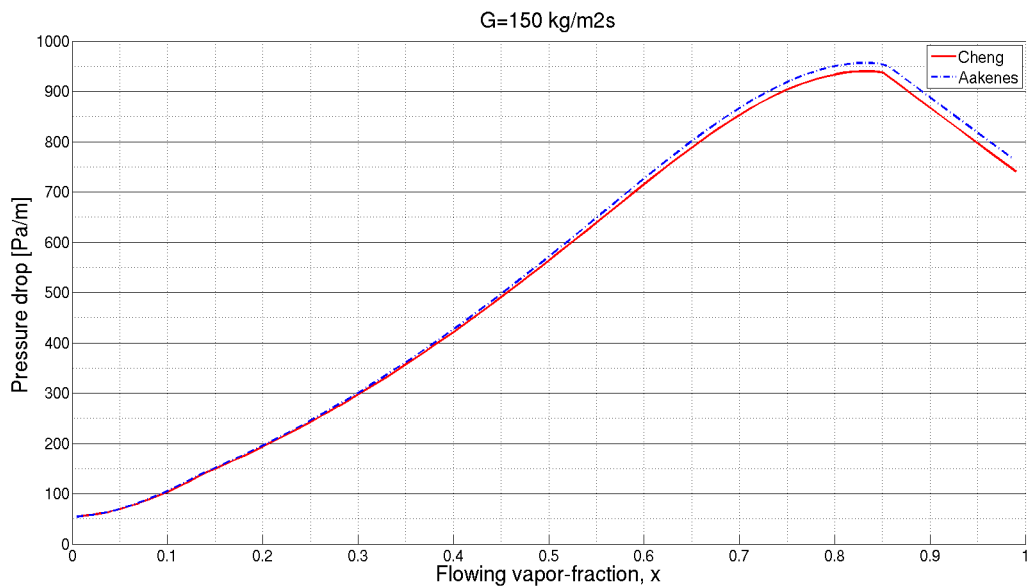
Figure 6.1: Flow-pattern maps generated by the MATLAB code.

Be aware; The bubbly transition-line is not shown in Figure 6.1. Further, the stratified transition line and the stratified-wavy transition-line are functions of the mass velocity,  $G$ ,

and are therefore slightly different in a) and b). The implementation is also verified for a test case in the stratified region.



(a)



(b)

Figure 6.2: Frictional pressure-drop as a function of the flowing vapor-fraction ( $x$ ) for the test conditions given in Table 6.1. The results from the MATLAB code (Aakenes), compared with Dr. Cheng's results.

### 6.2.2 Slip-model sensitivity

In this section, how the result using the Cheng et al. model is changing when different slip-correlations are used, will be investigated. The following slip relations will be used:

- The Rouhani-Axelsson version of the Zuber-Findlay slip-relation (see Section 2.3.3). This is used in the original version of the Cheng et al. model.
- A constant-parameter Zuber-Findlay slip-relation, where the parameters  $K_s$  and  $S_s$  (see Equation (2.24) and (2.25)) are evaluated at  $x = 0.5$ .
- No slip condition. Given by Equation (2.20) when  $K_s = 1$  and  $S_s = 0$ .

The result is illustrated in Figure 6.3. As seen from the plot, the frictional pressure-drop will be underestimated in the case of no slip (up to 20%). For the constant parameter Zuber-Findlay slip-relation, the frictional pressure-drop is calculated exact at  $x = 0.5$ , overestimated when  $x > 0.5$ , and underestimated when  $x < 0.5$ . In the mist region,  $x > 0.92$ , the calculated frictional pressure-drop is not affected by the slip relation.

As seen, the error arising when using the constant parameter Zuber-Findlay slip-relation around  $x = 0.5$  is small. Thus, the constant parameter Zuber-Findlay slip-relation may be a good and simpler alternative if a priori knowledge about the approximate flowing vapor-fraction is given. When using the COTT code, the use of a constant parameter Zuber-Findlay slip-relation would also reduce the computational cost. This is because iteration is avoided (See Appendix B).

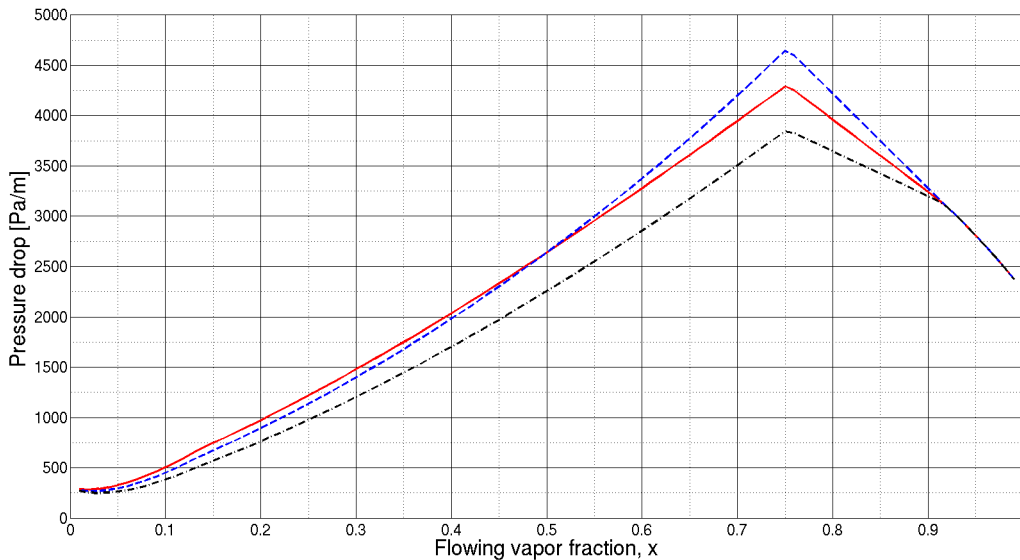


Figure 6.3: Slip-model sensitivity for the conditions listed in Table 6.1 and  $G = 400$ . Red continuous line: Rouhani-Axelsson. Blue dashed line: Rouhani-Axelsson evaluated at  $x = 0.5$ . Black dot-dash line: No slip.

## 6.3 Summary

In this chapter, the implementation of the Cheng et al. friction model was discussed in detail. First, the logic behind the program code was described in Section 6.1. In Section 6.2, the implementation of the program code was verified using results provided by Dr. Cheng. During this work some errors were found in the paper of Cheng et al. [8], these are described in Section 5.3.3 in Chapter 5.

The performance of the Cheng et al. model when different slip-models are used was investigated in Section 6.2.2. For the specific test case, we saw that when using the no-slip model, an underestimation of about 20 % was made. Nevertheless, the no-slip model will still be used in some of the cases in this report.



# Chapter 7

## Experimental data

### 7.1 Background

At Statoil Research Center Rotvoll in Trondheim, a CO<sub>2</sub> pipeline test rig is built with the purpose of understanding the physics related to transportation of CO<sub>2</sub>. The results used in this master's thesis are obtained from six steady-state two-phase pressure-drop experiments carried out at their test rig in 2007 [11, 12, 24].

### 7.2 The CO<sub>2</sub> pipeline test rig

The test rig consists of a 139 meter long 10 mm pipe, where the inlet is connected to a high-pressure (HP) tank and the outlet is connected to a low-pressure tank (See Figure 7.1). The pressure, temperature and mass flow rates are measured by several sensors as shown in Figure 7.1.

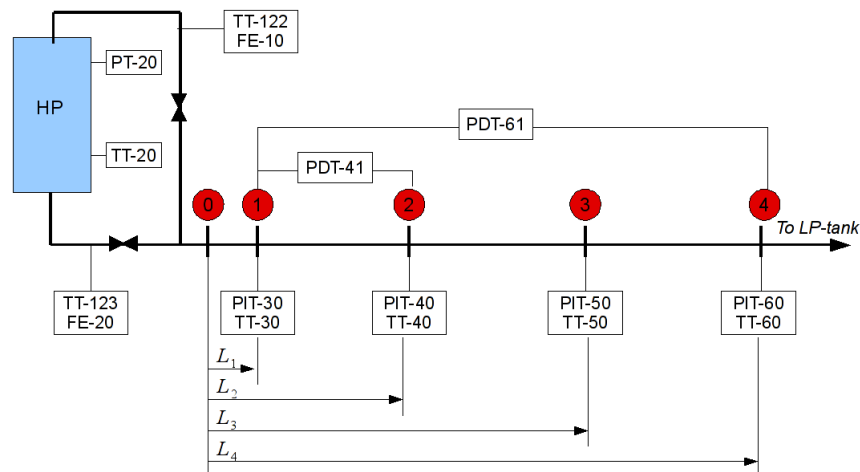


Figure 7.1: The test rig. Sensors measuring absolute pressure (PIT and PT), differential pressure (PDT), temperature (TT) and mass flow rates (FE) are placed as shown.  $L_1 = 0.2$  m,  $L_2 = 50.5$  m,  $L_3 = 101$  m and  $L_4 = 139$  m.

## 7.3 The experiments

Six experiments have been carried out in the test rig. The experiments were run until steady state was obtained, then the pressure, temperature and mass flow-rate were logged over a period of about 20 minutes. In further calculations, the average of the measurements at each location, have been used. An overview of the conditions in the experiments are given in Table 7.1. For further details see Appendix G.

Table 7.1: Overview of the experimental conditions in [24]. The flowing vapor-fraction and heat flux are calculated as shown in Section 7.4.

Variable		Range
Mass velocity [kg/m <sup>2</sup> s]	$G$	1058 – 1663
Flowing vapor-fraction	$x$	0.099 – 0.742
Saturated temperature [C°]	$T$	3.8 – 17
Reduced pressure	$p_r$	0.52 – 0.72
Heat flux [W/m <sup>2</sup> ]	$q''$	-91 – 150.8

## 7.4 Vapor-fraction calculations

The flowing vapor-fraction vary along the pipe length due to the frictional pressure-drop and heat transfer. This variation is estimated by making use property data from NIST together with some simple assumptions. The notation illustrated in Figure 7.2 will be used in all calculations in this section.

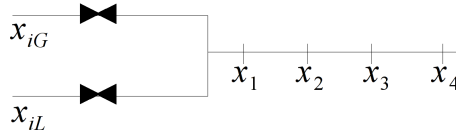


Figure 7.2: Notation used in the vapor-fraction calculations.  $x_{iG}$  and  $x_{iL}$  are the initial vapor fraction in the gas pipe and liquid pipe, respectively.  $x_1 - x_4$ , are the vapor fraction at the locations 1 – 4 along the test section.

### Assumptions:

- The fluid is saturated throughout the pipe test section (from position 1 – 4)
- Constant enthalpy through the throttling valves
- The frictional pressure-drop between the HP-tank and position 1 is neglected (except from the friction due to the throttling valves)
- Neglect heat loss between HP and position 1
- Neglect mixing losses where the gas stream and liquid stream meet



**Flowing vapor-fraction at the pipe inlet:**

The total enthalpy after the mixing will be (see Figure 7.3) :

$$h_1 = \frac{\dot{m}_G h_{iG} + \dot{m}_L h_{iL}}{\dot{m}_L + \dot{m}_G} \quad (7.1)$$

Hence, the flowing vapor-fraction can be calculated based on knowledge about the gas and liquid saturation-enthalpies at position 1.

$$x_1 = \begin{cases} \frac{h_1 - h_{l,1}}{h_{g,1} - h_{l,1}}, & \text{if } h_1 < h_{l,1} \\ 0, & \text{if } h_1 > h_{l,1} \\ 1, & \text{if } h_1 > h_{g,1} \end{cases} \quad (7.2)$$

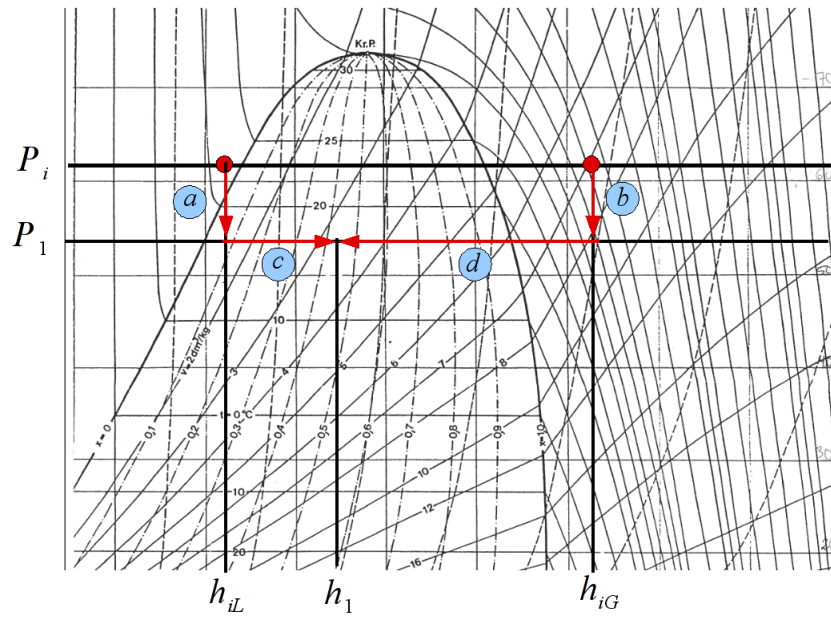


Figure 7.3: a) The liquid stream is throttled (the enthalpy is held constant  $h_{iL}$ ). b) The gas stream is throttled (the enthalpy is held constant  $h_{iG}$ ). c and d) The gas stream and liquid stream mix, and the total enthalpy for the mixture is  $h_1$ .

**Flowing vapor-fraction at positions 2,3 and 4 :**

The flowing vapor-fraction development from 1 to 4 can be estimated by making use of the energy conservation [28, Ch. 4]. By assuming steady state and by neglecting the change in kinetic and potential energy, we have:

$$\dot{m}h_2 = \dot{m}h_1 + q_{1-2} \quad (7.3)$$

Rearranging this equation, a relation for the flowing vapor-fraction is obtained:

$$x_2 = \frac{h_1 + q_{1-2}/\dot{m} - h_{l,2}}{h_{g,2} - h_{l,2}}, \quad (7.4)$$

where  $q_{1-2}$  is the heat added between location 1 and 2 which is modeled the following way:

$$q_{1-2} = U\pi d\Delta L(T_\infty - \frac{1}{2}(T_2 + T_1)), \quad (7.5)$$

where  $\Delta L$  is the distance between 1 and 2, and  $U$  is the overall heat transfer coefficient found to be approximately  $20 \text{ W/m}^2\text{K}$  for the given experiments [24]. Typically, a log-mean temperature profile is assumed in heat-exchange calculations like the one in Equation (7.5). However since the direction of the heat transfer vary along the pipe length, a linear temperature profile is assumed for simplicity. The thermodynamical process between location 1 and 2 is illustrated in the pressure-enthalpy ( $p - h$ ) diagram shown in Figure 7.4.

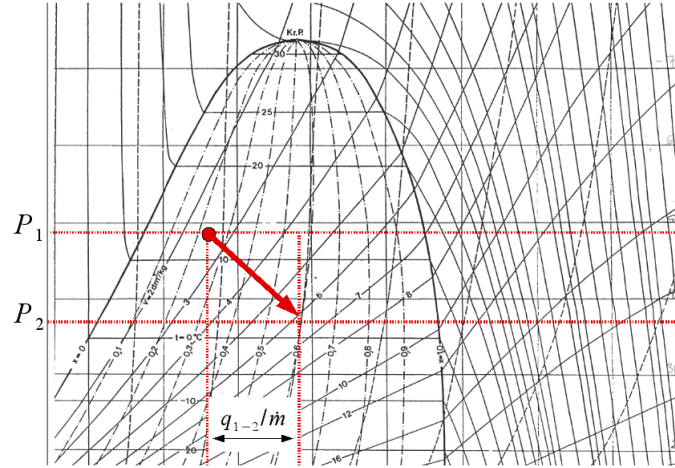


Figure 7.4:  $p - h$  diagram showing the thermodynamical process between location 1 and 2. As the fluid flows through the test section, the flowing vapor-fraction may either increase or decrease; It depends on the sign of  $q$  as well as the shape of the two-phase curve in that specific region. Here  $q$ , is positive.

## 7.5 The frictional pressure-drop

The measured pressure drop is the sum of the frictional pressure-drop ( $\Delta p_f$ ), the static pressure drop ( $\Delta p_s$ ) due to elevation change, and the momentum pressure-drop arising in a diabatic process ( $\Delta p_m$ ) [32].

$$\Delta p_{tot} = \Delta p_f + \Delta p_s + \Delta p_m \quad (7.6)$$

The pipe of interest is nearly horizontal [24], thus  $\Delta p_s$  is neglectable. The momentum pressure loss will be calculated the following way [8, 32] :

$$\Delta p_m = G^2 \left( \left[ \frac{(1-x)^2}{\rho_l(1-\alpha)} + \frac{x^2}{\rho_g \alpha} \right]_{out} - \left[ \frac{(1-x)^2}{\rho_l(1-\alpha)} + \frac{x^2}{\rho_g \alpha} \right]_{in} \right) \quad (7.7)$$

This can be recognized as the difference in the linear momentum at the inlet and outlet which will be non-zero if heat is added/removed. For the given experiments, the momentum pressure loss would be in the order of 0.007-0.025 bar (between location 1 and 4). It will be shown that this is small compared to the frictional pressure-drop, thus, for simplicity, the momentum pressure-loss will be neglected in further analysis.

## 7.6 Summary

In this chapter, the conditions and set-up for the given frictional pressure-drop experiments were presented. The flowing vapor-fraction is an important input parameter in many friction models. However this property is not measured directly in the experiments. A detailed discussion of the simplified calculation of the flowing vapor-fraction for each position along the pipe test-section, was therefore preformed in Section 7.4.



# Chapter 8

## Uncertainty and sensitivity

Measurements of the temperature, pressure and mass flow rates in the experiments [24], will be used in several calculations in this report. However, when dealing with experiments we have to be aware that the *measured value* is not the same as the *true value*. How the range in which the *true value* of a given variable lies within, can be estimated. This is treated in Section 8.1 and 8.2.

The friction models are functions of several variables. These variables will be calculated based on temperature, pressure and mass-flow rates given by sensors which are, as mentioned above, not necessarily measuring the system correctly. How each of the friction models are affected by the uncertainty of the model-input variables will be treated in Section 8.3.

### 8.1 Uncertainty

The term uncertainty can be defined as “the possible value an error may have” [27]. The true value,  $R$ , is unknown, but will be estimated as:

$$R = R_m \pm \Delta R, \quad (8.1)$$

where  $\Delta R$  is the possible error in the measured value  $R_m$ .

How the error is estimated, depends on what we choose as the definition of the *true value*. Moffat [27] presents four possible definitions of this value:

- $R(1)$  *The achieved value*, e.g. the pressure felt by the sensor
- $R(2)$  *The available value*, e.g. the pressure in the fluid flow
- $R(3)$  *The undisturbed value*, e.g. what the pressure in the fluid flow would have been if the sensors did not disturb the system
- $R(4)$  *The conceptual value*, e.g. the cross-sectional-average pressure in the fluid

For simplicity, and because  $R(1)$ ,  $R(2)$ ,  $R(3)$  and  $R(4)$  are assumed to be about the same, *the achieved value* will be used as the *true value* in this report. In this case, errors may arise only because of the measuring system alone.

### 8.1.1 Categorization of errors

Moffat [27] categorizes the errors into three different groups.

- *Bias error*, which are *fixed* and therefore not changing with time. It will be referred to as  $\Delta R_B$ .
- *Precision error*, which are presumed to behave *randomly* with a zero mean. It will be referred to as  $\Delta R_P$ .
- *Variable but deterministic error*, which are changing with time, but not randomly. It will be referred to as  $\Delta R_V$ .

The bias error and the precision error are illustrated in Figure 8.1.

The fact that the sensors are not calibrated 100 % correctly, would be an example of a *bias* error. The fact that the measuring system has an absolute resolution would result in a precision error, and the error arising because of temperature changes in the instrument would be an example of a variable but deterministic error.

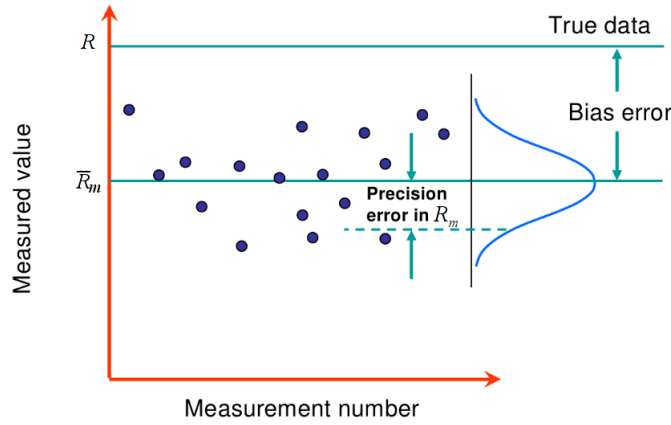


Figure 8.1: The Bias error is fixed, and the precision error behaves randomly with a zero mean.

It will be assumed that the error specified by the manufacturer of the measuring instrument and those who have calibrated it, is the sum of the *the bias error* and the relevant *variable but deterministic errors*. The standard deviation of a test sample is used as an estimation of the precision error. For further details see [27]. The total uncertainty can further be found using the root-mean-square formula:

$$\Delta R = \sqrt{\Delta R_B^2 + \Delta R_P^2 + \Delta R_V^2} \quad (8.2)$$

### 8.1.2 Error propagation

In many experiments, the result is a function of several measurements. Let  $R = R(r_1, r_2, \dots, r_k)$ , where  $r_1, r_2, \dots, r_k$  are independent measurements. The error in  $R$  can hence be obtained using the root-mean square formula.

$$\Delta R = \left[ \sum_{i=1}^N \Delta R_{r_i}^2 \right]^{1/2} = \left[ \sum_{i=1}^N \left( \frac{\partial R}{\partial r_i} \Delta r_i \right)^2 \right]^{1/2}, \quad (8.3)$$

where  $\Delta R_{r_i}$  is the total uncertainty in  $R$  because of the uncertainty in variable  $r_i$ . This equation applies in the calculations of the bias error, precision error and the variable but deterministic error.

### 8.1.3 Multiple-sample versus single-sample experiments

How the uncertainty analysis is carried out depends on what kind of experiment we are dealing with. Moffat [27] makes a distinction between *multi-sample experiments* and *single-sample experiments*.

The *single-sample experiments* are those in which each test point is run only once, or at least only a few times [27]. In this case the bias error, the precession error and the variable but deterministic errors are all important. In the *multi-sample experiments*, we are dealing with the mean of a “large” number of independent data point taken at the same test point. If the sample is large enough, the precision error will, according to its definition, be averaged out. Thus, only the bias error and the variable but deterministic error will be considered.

In our case, it is not obvious if we are dealing with a *single-sample* or *multi-sample* experiment. The pressure, temperature and mass flow are measured and logged every second for about 20 minutes, and the averages are used in further calculations. This result in a relatively big sample and can thus be considered as a *multi-sample experiment*. However, there is one drawback. Each data point taken at the same test point is not completely independent. This is mainly because there is expected to be some “lag” related to the sensors . For instance, the temperature present at one location at one point in time would effect the temperature measured one second later. Nevertheless, in this analysis, it will still be assumed that the precision error is averaged out.

## 8.2 Uncertainty analysis

### 8.2.1 Sensor uncertainty

The size of the sensor uncertainties (that is the bias error plus the variable but deterministic error) are listed in Table 8.1.

Table 8.1: Sources of uncertainty (about 2.5 standard deviations) [13, 24]

Source		Uncertainty
Temperature sensor	$T$	$\pm 0.5$ K
Absolute-pressure sensor	$p$	$\pm 0.16$ bar
Differential-pressure sensor	$\Delta p$	$\pm 0.05$ bar
Gas-flow meter	$\dot{m}_G$	$\pm 0.06$ %
Liquid-flow meter	$\dot{m}_L$	$\pm 0.3$ %

### 8.2.2 Pressure-drop uncertainty

When the absolute pressure sensors are used in order to estimate the experimental pressure drop, we have:

$$f = p_1 - p_2 \quad (8.4)$$

The uncertainty in  $f$  is hence found using the root-mean-square formula, Equation (8.3):

$$\Delta f = \left[ \left( \frac{\partial f}{\partial p_1} \Delta p_1 \right)^2 + \left( \frac{\partial f}{\partial p_2} \Delta p_2 \right)^2 \right]^{1/2}, \quad (8.5)$$

$$\Delta f = \left[ (\Delta p_1)^2 + (\Delta p_2)^2 \right]^{1/2}, \quad (8.6)$$

where  $\Delta p_1$  and  $\Delta p_2$  are found in Table 8.1. This result in,  $\Delta f = \pm 0.23$  bar.

The uncertainty related to the differential-pressure sensors are  $\Delta P = \pm 0.05$  bar (see Table 8.1), and are thus much smaller than the uncertainty in the pressure drop calculated using the absolute-pressure sensors. Therefore, the differential-pressure sensors will be used instead of the absolute-pressure sensors in pressure drop calculations.

### 8.2.3 Uncertainty in other variables

The fluid properties, the total mass-velocity and the flowing vapor-fraction are functions of temperature, pressure and mass-flow rates, which are measured by sensors. Thus, the uncertainty presented in Section 8.2.1 will, because of the error propagation described in Section 8.1.2, result in an uncertainty in the mentioned variables.

Besides the sensor uncertainty (listed in Table 8.1), additional uncertainty will be introduced by the use of a heat-transfer model and the equation of state. For simplicity, the uncertainties in the fluid properties given by NIST [1] are neglected because this is expected to be small compared to the the uncertainties arising because of sensor uncertainties. The uncertainty in the overall heat-transfer coefficient,  $U$ , is set to  $\pm 50\%$  [24, Sec. 4.2].

#### Fluid property uncertainty:

The fluid property uncertainty is obtained by perturbing the temperature and pressure with the corresponding sensor uncertainty. Further, the deviation in each property is found using NIST data [1]. The results are given in Table 8.2.

Table 8.2: Fluid property uncertainty

Fluid properties		[%]
Gas density	$\Delta \rho_g / \rho_g$	0.47
Liquid density	$\Delta \rho_l / \rho_l$	0.13
Gas viscosity	$\Delta \mu_G / \mu_g$	0.15
Liquid viscosity	$\Delta \mu_L / \mu_l$	0.28
Surface tension	$\Delta \sigma / \sigma$	0.96
Mixture enthalpy in gas pipe	$\Delta h_{i,G} / h_{i,G}$	0.69
Mixture enthalpy in liquid pipe	$\Delta h_{i,G} / h_{i,L}$	0.58
Saturated enthalpy of the gas phase	$\Delta h_g / h_g$	0.04
Saturated enthalpy of the liquid phase	$\Delta h_l / h_l$	0.17



**Uncertainty in  $h_{LG}$ :**

The heat of vaporization is:

$$h_{lg} = h_g - h_l \quad (8.7)$$

Hence, the uncertainty in the heat of vaporization can be calculated using the root-mean-square formula (Equation (8.3)). Thus,

$$\Delta h_{lg} = \left[ (\Delta h_g)^2 + (\Delta h_l)^2 \right]^{1/2}. \quad (8.8)$$

For experiment 1 at location 1,  $\Delta h_{lg}/h_{lg} = 0.23\%$ . For simplicity, this value will also be assumed at location 2,3 and 4.

**Uncertainty in  $G$ :**

The mass velocity is

$$G = \frac{\dot{m}_g + \dot{m}_l}{A}. \quad (8.9)$$

Hence the uncertainty in the mass velocity can be calculated using the root-mean-square formula, Equation (8.3), such that

$$\Delta G = \left[ \left( \frac{1}{A} \Delta \dot{m}_g \right)^2 + \left( \frac{1}{A} \Delta \dot{m}_l \right)^2 \right]^{1/2}. \quad (8.10)$$

For experiment 1 at location 1,  $\Delta G/G = 0.23\%$ .

For simplicity, this value will also be assumed at location 2,3 and 4.

**Uncertainty in  $x$ :**

The uncertainty in  $x$  is calculated numerically by perturbing all the relevant input variables (see Equation (7.2) and (7.4)) and further apply the root-mean-square formula, Equation (8.3). Table 8.3 summarizes what is obtained for the locations 1, 2, 3 and 4.

As seen from Table 8.3, the absolute uncertainty in  $x$  is about the same for the locations 1, 2, 3 and 4.

The fact that the flow may not be completely saturated through the test section is another important source of error especially in the flowing-vapor-fraction calculation. However, the uncertainty related to this is hard to quantify based on the information given in [24]. Thus, this is not taken into account in this analysis.

Table 8.3: The absolute uncertainty and relative uncertainty due to sensor uncertainty at location 1, 2, 3 and 4 defined in Figure 7.1.

Location	$\Delta x_i$ [%]	$\Delta x_i/x_i$ [%]
1	6.39	6.49
2	6.13	4.93
3	6.13	3.96
4	6.50	3.51

### 8.3 Friction-model sensitivity

The friction models are functions of several fluid properties and flow variables in which there is uncertainty (see Section 8.2.3). In this section it will be performed a sensitivity analysis in order to see how the model-input uncertainty will affect the result obtained using the relevant friction models (see e.g. Figure 8.2).

The fluid-property uncertainty, the uncertainty in derived properties such as the mass velocity,  $G$ , the heat of vaporization,  $h_{LG}$ , and the flowing vapor-fraction,  $x$ , are used (see Equation 8.8, Equation 8.10, and Table 8.3). The model-input sensitivity for the Friedel model, the Cheng et al. model and the homogeneous model, for experiment no 1 at location 1 are then calculated. The results are summarized in Table 8.4.

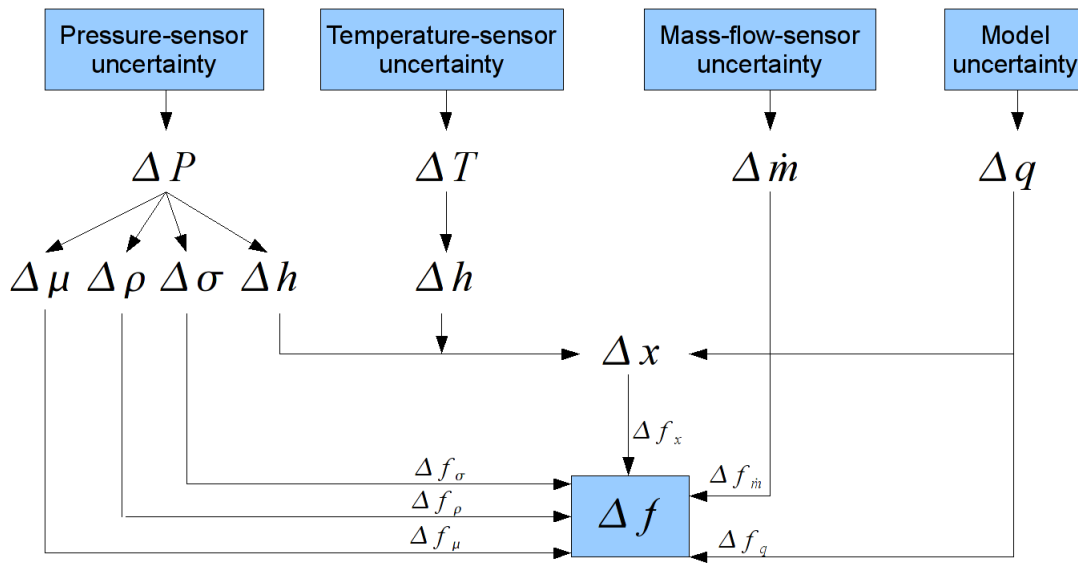


Figure 8.2: The friction models are a function of several variables and will hence be more or less sensitive to the variation of all of them. The uncertainty in the model-input variables arises due to sensor uncertainty and model uncertainty. The total sensitivity in the friction model,  $\Delta f$ , can hence be found using the root-mean square formula (8.3).

Table 8.4: The model-input sensitivity for the Friedel model, the Cheng et al. model and the homogeneous model, for experiment no 1 at location 1. Here the expected uncertainty in the model-input variables calculated in Section 8.2.3 are used.

Variable		Friedel $\Delta f_{q_i}$ [Pa/m]	Cheng $\Delta f_{q_i}$ [Pa/m]	Hom. $\Delta f_{q_i}$ [Pa/m]
Mass velocity	$\Delta G$	16.34	8.62	16.37
Flowing vapor-fraction	$\Delta x$	85.20	46.01	68.55
Gas density	$\Delta \rho_g$	9.29	0.04	6.72
Liquid density	$\Delta \rho_l$	2.59	3.00	3.05
Gas viscosity	$\Delta \mu_G$	0.032	1.07	0.24
Liquid viscosity	$\Delta \mu_L$	2.91	0.59	0.86
Surface tension	$\Delta \sigma$	0.74	0.59	-
Heat of vaporization	$\Delta h_{lg}$	-	0	-
Heat transfer	$\Delta q$	-	0	-
Absolute sensitivity [Pa/m]	$\Delta f$	87.34	46.92	70.86
Relative sensitivity [%]	$\Delta f/f$	2.05	1.95	1.87

As seen in Table 8.4, the the uncertainty in the flowing vapor-fraction, the total mass velocity ( $G$ ) and the gas density are what effects the results the most.

The Cheng et al. model will only be directly sensitive to variation of the heat of vaporization and the heat transfer when located in the dry-out region or in the mist region. However, in experiment 1 at location 1, the flow pattern is predicted to be intermittent (will be shown in Figure 9.2).

The Friedel model is not directly a function of the heat of vaporization or the heat transfer, thus the sensitivity to the variation of these variables are zero. The same is true for the homogenous model, which neither depend on the heat of vaporization, the heat transfer or the surface tension.

#### The Friedel model:

The total model-input sensitivity for the Friedel model is  $\pm 87.34$  Pa/m. For the distance between location 1 and 2 this means  $\pm 0.044$  bar, and for the distance between location 1 and 4 this means  $\pm 0.121$  bar.

#### The Cheng et al. model:

The total model-input sensitivity for the Cheng et al. model is  $\pm 46.92$  Pa/m. For the distance between location 1 and 2 this means  $\pm 0.024$  bar, and for the distance between location 1 and 4 this means  $\pm 0.065$  bar.

#### The homogeneous model:

The total model-input sensitivity for the homogeneous model is  $\pm 70.86$  Pa/m. For the distance between location 1 and 2 this means  $\pm 0.036$  bar, and for the distance between location 1 and 4 this means  $\pm 0.098$  bar.

Several simplifying assumptions are made throughout this analysis:

- The friction models assumes that the pipe-wall roughness will not affect the frictional pressure-drop
- It is assumed that the flow is completely saturated between position 1 to 4
- Steady state is assumed
- The momentum pressure-drop and the static pressure-drop described in Section 7.5, are neglected

These can be thought of as additional sources of uncertainty. If not steady state is the case, the measured pressure drop will be different from the frictional pressure-drop and if the flow is not saturated, the calculated fluid properties and the flowing vapor-fraction would be very different.

## 8.4 Summary

In this chapter, the uncertainty associated with the experiments [24] and the friction-model sensitivity was investigated.

According to Moffat's definitions [27], the experiments were assumed to be *multi-sample experiments*, and thus only the *bias error* and the *variable but deterministic error* were considered. Further, only the errors arising due to the measuring system alone were taken into account. The total uncertainty of the differential pressure sensors, which will be used in further analysis, were found to be  $\pm 0.05$  bars.

The friction-model sensitivity was investigated in Section 8.3. It was found that the friction models were sensitive to all of its input-variables, especially the mass velocity ( $G$ ), the flowing vapor-fraction ( $x$ ), and the gas density ( $\rho_g$ ). The total model-input sensitivity due to the uncertainty in the flow variables was found to be between  $\pm 0.024$  bar –  $\pm 0.121$  bar.

The fact that the fluid is not completely saturated in the test section, is an additional important source of uncertainty. However, this is not quantified.

**Part III**

**RESULTS AND DISCUSSION**



# Chapter 9

## Friction-model comparison

The homogeneous pressure drop model, the Friedel model [20] and the Cheng et al. model [8] are compared to frictional pressure-drop experiments [24]. The objective is to give an indication what friction model will most accurately describe the frictional pressure-drop arising in pipelines for carbon dioxide transport.

The MATLAB code described in Chapter 6 will be used in all calculations in this chapter.

### 9.1 Calculations

The modeled pressure-drop between location 1 and  $N$  (see Figure 7.1) is calculated the following way:

$$\Delta p_{1-N} = \sum_{i=1}^N \frac{1}{2} \left( \left. \frac{\partial p}{\partial x} \right|_i + \left. \frac{\partial p}{\partial x} \right|_{i+1} \right) \Delta x_i, \quad (9.1)$$

where  $\Delta x_i$  is the distance between location  $i$  and  $i + 1$ , and  $\partial p / \partial x|_i$  is the pressure gradient given by the friction model at location  $i$ . The calculations are based on saturated fluid properties predicted by NIST [1] at the pressure given by the absolute-pressure sensors at each location (see Figure 9.1).

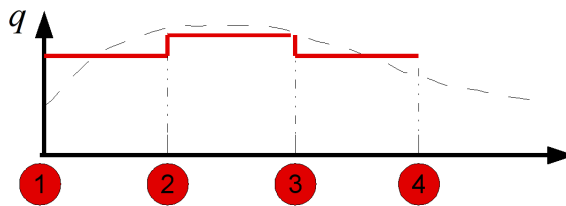


Figure 9.1: The quantity,  $q$ , measured by the sensor is varying along the test-section (dashed line). However,  $q$  is only available at position 1,2,3 and 4. Therefore,  $(q_i + q_{i+1})/2$  is assumed in the region between  $i$  and  $i + 1$  (red continuous line).

The calculated  $\Delta p_{1-2}$  and  $\Delta p_{1-4}$  for each experiment are compared to the experimental pressure drop measured by PDT-41 and PDT-61, respectively (see Figure 7.1).

Be aware that the heat flux,  $q''$ , is set to 0 when using then Cheng et al. model. This is because the model does not handle the sometimes negative heat flux. Because the heat flux is relatively small, the error due to this assumption will be small.

## 9.2 Results

A rough illustration of the flow patterns predicted by the Cheng et al. model for the four locations in each experiment is shown in Figure 9.2. The flow-pattern maps are not exactly the same for every experiment and each location, this is the reason for thick transition lines.

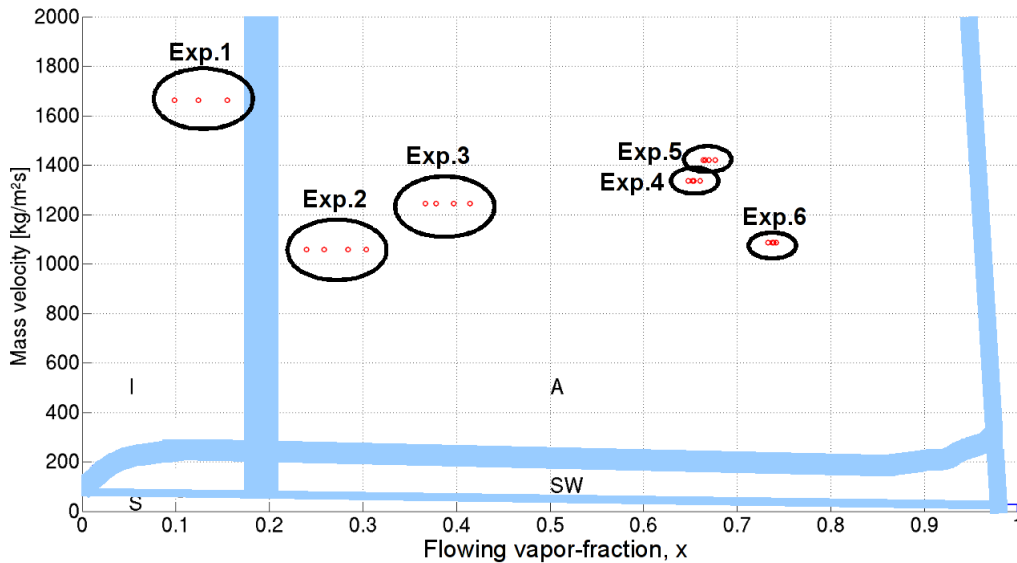


Figure 9.2: A rough illustration of the flow patterns predicted by the Cheng et al. model for each experiment. Be aware that several flow pattern maps have been plotted on the top of each other in this figure.

The experimental pressure drop and the pressure drop predicted by the friction model between position 1 – 2, and 1 – 4, are compared as shown in Figures 9.3, 9.4 and 9.5 . The 45-degree line indicates where the friction model predicts the pressure drop exactly, and the two neighboring dashed lines represent the calculated relative standard-deviation for the given sample (see Equation 9.2 and Table 9.1). This value can be interpreted as the uncertainty in the friction model itself. The uncertainty in the differential-pressure sensors is represented as a horizontal bar accompanied by each dot. The friction-model-input sensitivity is represented as a vertical bar accompanied by each dot. As seen, the friction-model-input uncertainty and the sensor uncertainty are small compared to uncertainty in the friction model itself. Thus, the uncertainty calculated in Chapter 8 is not considered as important when deciding what friction model is the most accurate.



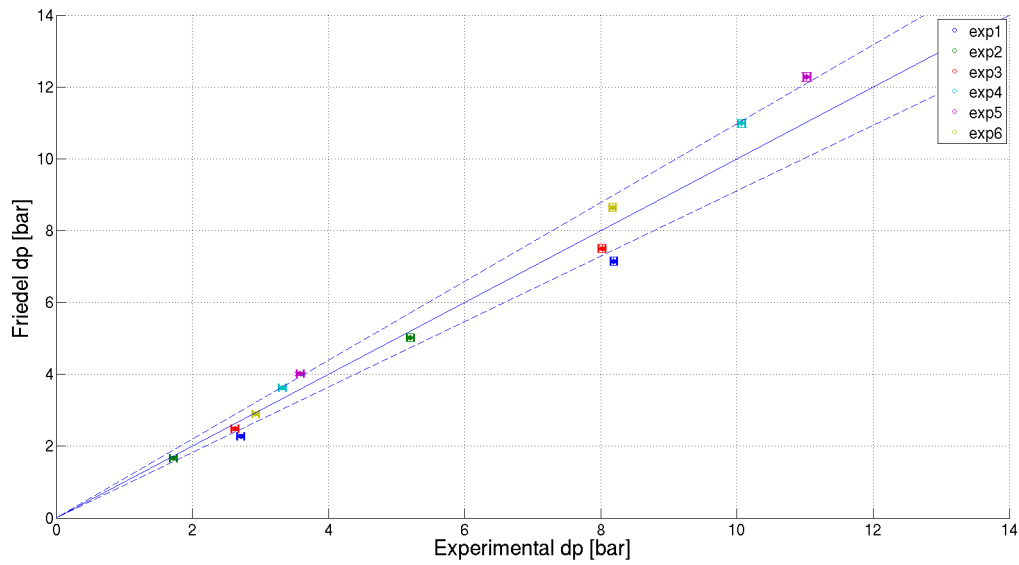


Figure 9.3: A comparison of the experimental pressure drop and the modeled pressure drop using the Friedel model. The calculated relative standard-deviation is  $s_R = 9.7\%$ .

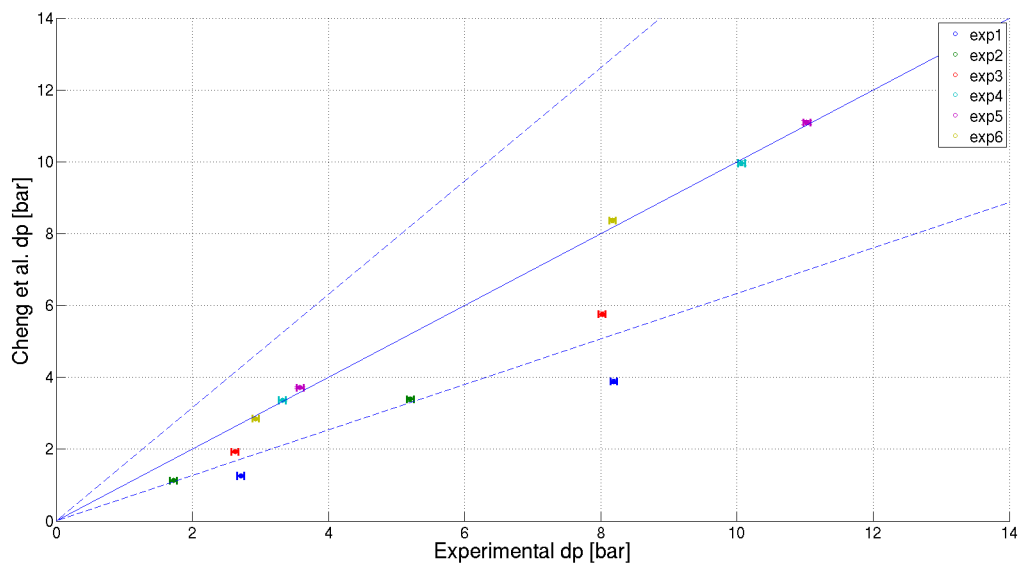


Figure 9.4: A comparison of the experimental pressure drop and the modeled pressure drop using the Cheng et al. model. The calculated relative standard-deviation is  $s_R = 57.74\%$ .

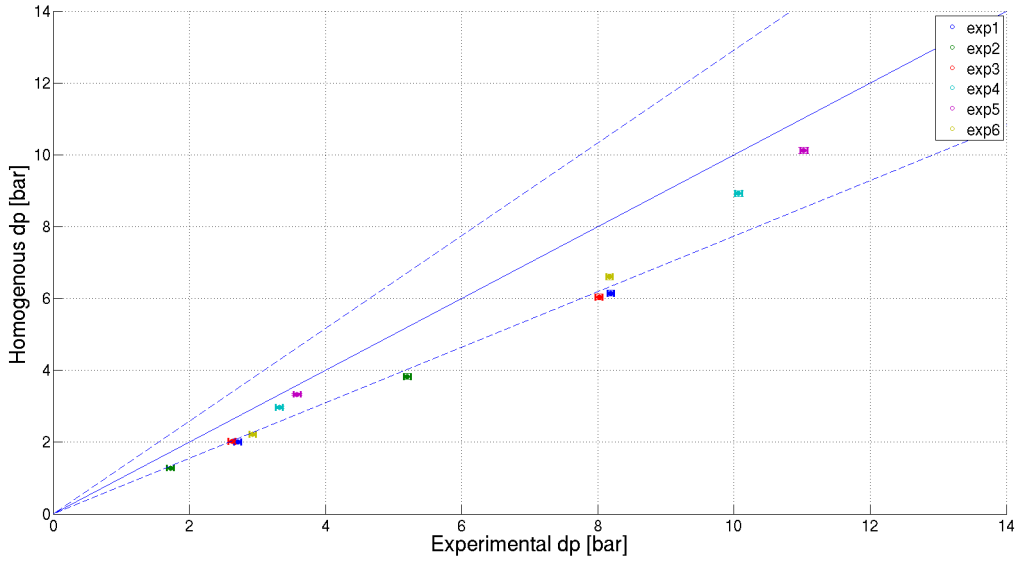


Figure 9.5: A comparison of the experimental pressure drop and the modeled pressure drop using the homogenous model. The calculated relative standard-deviation is  $s_R = 29.18\%$ .

### Model-error estimation

As expected, neither of the friction models are able to predict the frictional pressure-drop exactly. However, as seen from the above figures, the predictions are not necessarily far off. The models' ability to predict the pressure drop can be represented by the *relative standard deviation* or the *mean error*.

### Relative standard deviation

The relative standard deviation is used by Friedel [20] and is calculated using the following equation:

$$s_R = \left( \frac{1}{N-1} \sum_i z_i^2 \right)^{1/2}, \quad (9.2)$$

where

$$z_i = \frac{\Delta p_{i,exp} - \Delta p_{i,pred}}{\Delta p_{i,pred}}. \quad (9.3)$$

### Mean error

An alternative way to represent the accuracy of the friction models is by the *mean error*. It is used by Cheng et al.[8] and is defined as:

$$\bar{e} = \left( \frac{1}{N} \sum_i |z_i| \right) \quad (9.4)$$

The mean error and the relative standard deviation are further computed for the relevant friction models. The results are summarized in Figure 9.1.

Only the data points for the total pressure drop (between location 1 and 4) is used in these calculations.

Table 9.1: Friction-model error calculated based on all experiments given in [24].

<b>Model</b>	$s_R[\%]$	$\bar{e}[\%]$
Friedel	9.7	8.13
Cheng et al.	57.74	19.93
Homogenous	29.18	19.11

### 9.3 Discussion

As seen from Table 9.1, when considering all experiments in the given sample [24], the Friedel model predicts the frictional pressure-drop most accurately. The Cheng et al. model, on the other hand, predicts the frictional pressure-drop the least accurately. This is a bit surprising since the Cheng et al. model is developed specifically for CO<sub>2</sub> flows. The reason is probably because the mass flow rates in the experiments investigated in this report [24], are much higher than what the this model is developed for. Thus, this is an indication that the significance of CO<sub>2</sub>-specific insight (which is exploited in the Cheng et al. model) is relatively small compared to the importance of a larger database of data (which is advantage of the Friedel model).

From Figure 9.4, it seems like there is a huge difference of how well the Cheng et al. model is able to predict the pressure drop for experiment number 4, 5, and 6 compared to 1, 2 and 3. One main difference between these two groups of experiments can be seen in Figure 9.2; Experiment 4,5, and 6 are associated with a higher flowing vapor-fraction. When only these “high flowing-vapor-fraction” experiments are considered, a huge reduction in the computed standard deviation will arise for the Cheng et al. model (see Table 9.2). This may be a coincidence or an indication that the Cheng et al model works better for higher vapor fractions. More experiments should be carried out in order to verify the indicated trend.

In the next section, the above results will be compared to the results obtained in the paper of Friedel [20] and Cheng et al. [8].

Table 9.2: Friction-model error calculated based on the high flowing-vapor-fraction experiments (experiment 4, 5 and 6)

<b>Model</b>	$s_R[\%]$	$\bar{e}[\%]$
Friedel	10.2	8.78
Cheng et al.	1.85	1.35
Homogenous	20.12	12.92

### 9.3.1 Comparison with Friedel's results

For all the horizontal single-component two-phase flow in Friedel's database, Friedel calculated a relative standard deviation of 32 % [20, Tab. 3]. The fact that the relative standard-deviation calculated in this report (9.7 %) is less than 32 %, shows that the results obtained for the given sample [24] is far better than expected. This may be an indication that the Friedel correlation is a suitable model for prediction pressure drop in CO<sub>2</sub> flows. However, it should be emphasized that an absolute conclusion is hard to make based on only six experiments.

### 9.3.2 Comparison with Cheng et al.'s results

The mass flow-rates in the experiments investigated in this report [24], are much higher than what the Cheng et al. model [8] is developed for. Nevertheless, the model still estimates the frictional pressure-drop well for the high flowing-vapor-fraction experiments.

In the paper of Cheng et al. [8], 387 pressure-drop experiments for CO<sub>2</sub> is compared to the Cheng et al. model and the Friedel model. Here a mean error of 28.6 % and 30.9 % were found respectively. This is higher than the results in this report (19.93 % and 8.13 %), especially for the Friedel model. This may indicate that the Friedel model works better for CO<sub>2</sub> at higher mass flow rates than at lower mass flow rates.

## 9.4 Summary and conclusion

In this chapter, the Friedel model [20], the Cheng et al. model [8] and the homogenous model have been compared with six steady-state pressure-drop experiments [24]. The following is determined:

- When all the six experiments are considered, the Friedel model is superior with a standard deviation of only 9.7 %. The performance of the Cheng et al. model is even less accurate than the homogeneous model with a relative standard deviation of 57.74 % versus 29.18 %. This is an indication that the significance of CO<sub>2</sub>-specific insight (which is exploited in the Cheng et al. model) is relatively small compared to the importance of a larger pressure-drop database (which is advantage of the Friedel model).
- The frictional pressure drop is underestimated; for all experiments when using the homogenous model, and for the low vapor-fraction experiments when the Cheng et al. model is used.
- When only the high flowing-vapor-fraction experiments are considered, the Cheng et al. model is superior, with a relative standard deviation of only 1.85 %.
- The calculated relative standard deviation for the Friedel model was 9.7 % and thus much lower than the relative standard deviation for the large pressure-drop database used by Friedel (32 %). This may be an indication that the Friedel model is just as suitable for predicting the pressure drop in CO<sub>2</sub> as for other fluids.
- The friction-model-input uncertainty and the sensor uncertainty are small compared to uncertainty in the friction model itself. Thus, the uncertainty calculated in Chapter 8 is not considered as important when deciding what friction model is the most accurate.

# Chapter 10

## Steady-state simulation

The Cheng et al. model and the Friedel model are implemented in the COTT code and experiment 1 presented in Chapter 7 is simulated. The results are verified using results from Chapter 9.

### 10.1 Mathematical models used

The following mathematical models are used:

**Transport model:** DF3 model, Equation (2.13), (2.14), and (2.15)

**Slip model:** No slip, Equation (2.20) with  $K_s = 1$  and  $S_s=0$ .

**Friction model:** Friedel [20] and Cheng et al. [8] (see Section 5.3.2 and 5.3.3)

**EOS:** Span-Wagner [36]

Heat transfer through the pipe wall is neglected.

In Section 6.2.2 it was shown that when using no-slip in the Cheng et al. model, the frictional pressure-drop would be underestimated. Nevertheless, no-slip will still be applied because slip is not yet implemented in the COTT code when the DF3 model with the Span-Wagner EOS is used.

#### 10.1.1 Initial conditions

The initial condition is set equal to the measured inlet condition (see Appendix G).

- Pressure,  $p_1 = 48.69$  bar
- Flowing vapor-fraction,  $x_1 = 0.0986$
- Mass velocity,  $G = 1662.8$  kg/m<sup>2</sup>s

Saturated condition is present, with liquid and gas coexisting.

### 10.1.2 Boundary conditions

The DF3 model, consist of three first order differential equations. – One momentum equation, one energy equation and one continuity equations (see Section 2.3.1). In order to solve this system, three variables have to be specified at a boundary. In the case of subsonic flow to the right, three right-going characteristics and one left-going characteristic are present. Thus the pressure will be specified at the eastern boundary. Further, two other properties have to be specified at the western boundary. Based on available information from the experiments [24],  $G$  and  $x$  are specified here (see Figure 10.1).

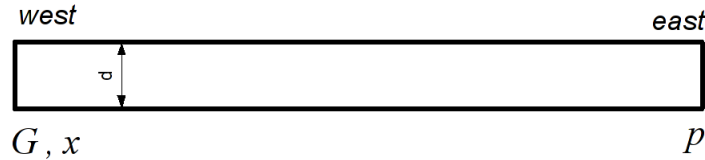


Figure 10.1: The mass velocity ( $G$ ) and the flowing vapor-fraction ( $x$ ) are specified on the western boundary. The pressure ( $p$ ) is specified on the eastern boundary.

#### Western boundary:

- Mass velocity,  $G = 1662.8 \text{ kg/m}^2\text{s}$
- Flowing vapor-fraction,  $x = 0.0986$

#### Eastern boundary:

- Pressure,  $p = 40.33 \text{ bar}$

Based on this information, the rest of the variables can be calculated. Details about the implementation of the boundary conditions can be found in Appendix C.

### 10.1.3 Numerical setup

The mathematical model is solved numerically. The forward Euler method is used for time discretization and the MUSTA method is used for spatial discretization. The numerical parameters used are given in Table 10.1.

Table 10.1: The numerical parameters used in the steady-state simulation

CFL- number	0.9
MUSTA sub steps	4
MUSTA- local cells	4

## 10.2 Results

The simulations were run until  $t = 130$  s. At this time, steady-state condition was obtained. Figure 10.2 shows the results from a grid refinement test done when the Friedel model is used. As seen from the plot, the result converges as the grid is refined. A grid refinement test is also made when using the Cheng et al. model (see Figure 10.3). The total pressure drop between position 1 and 4 (for  $N = 100$ ) is found to be  $\Delta p = 6.58$  bar and 2.91 bar when using the Friedel model and Cheng et al. model respectively.

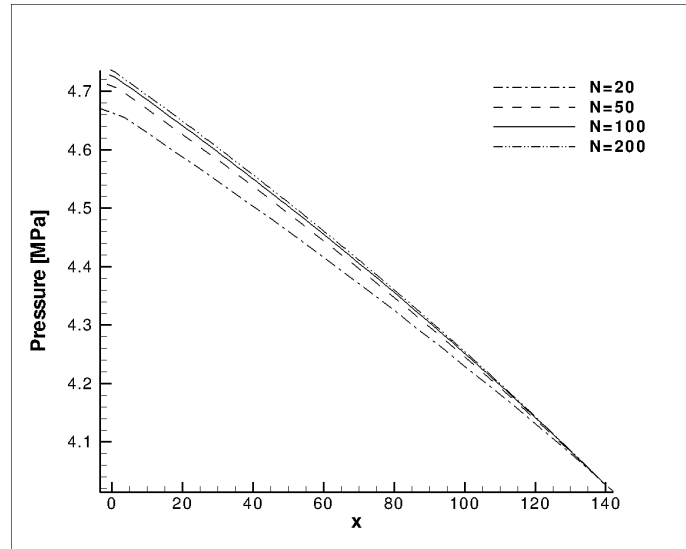


Figure 10.2: Pressure. Grid refinement test using the Friedel model.

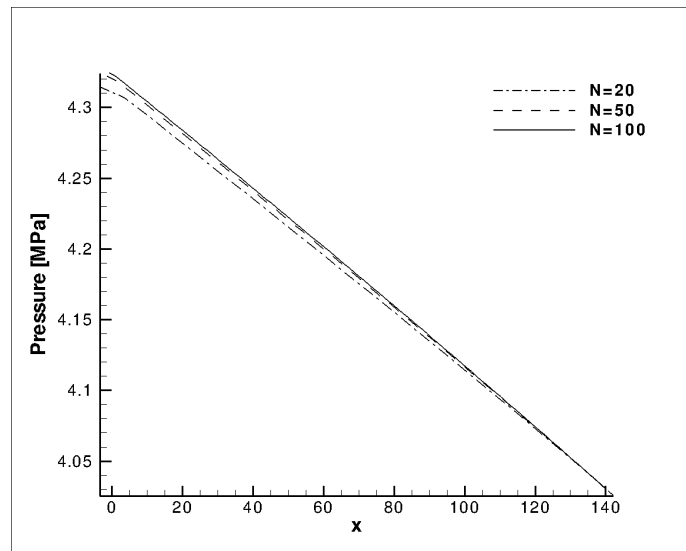


Figure 10.3: Pressure. Grid refinement test using the Cheng et al. model.

The consequences of an incorrect prediction of the frictional pressure-drop, is misprediction of many fluid variables. It was shown in Figure 9.4 that the Cheng et al. model underestimates

the frictional pressure-drop for experiment number 1. Hence, the liquid density will be overestimated and the temperature, the flowing vapor-fraction and the gas density will be underestimated (see Figure 10.4). Be aware that which variables are underestimated and overestimated will change if the boundary conditions are set differently.

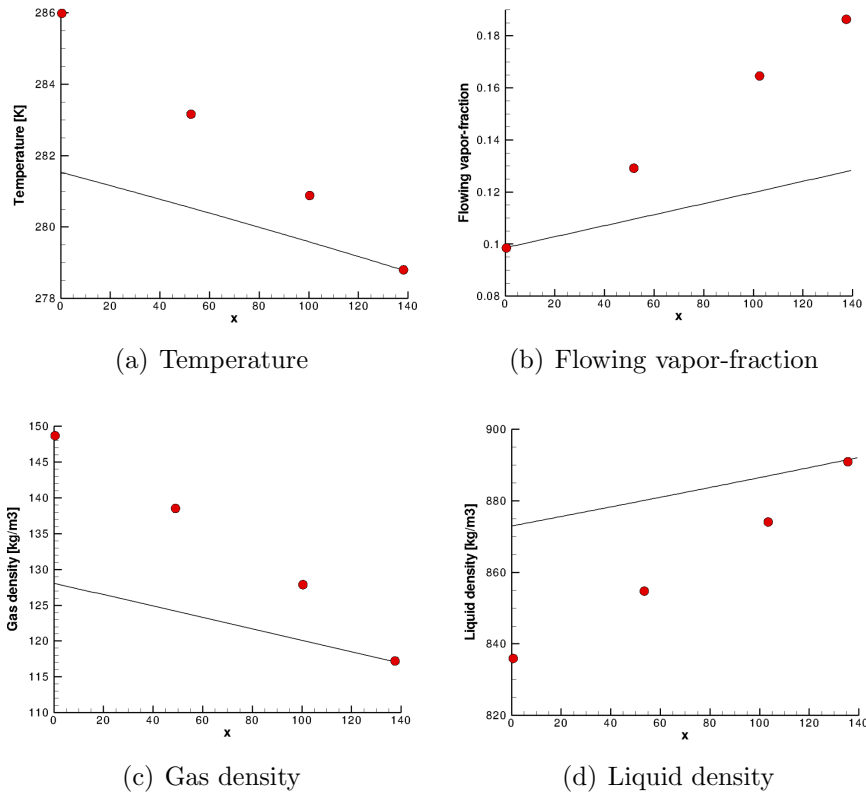


Figure 10.4: The fluid properties evaluated using the experimental pressure, temperature, and mass flow-rates (red dots). The fluid properties calculated by the COTT code when the Cheng et al. model (and no slip) is used (black line).

The fluid properties and flow variables are input parameters in the friction-models. The misprediction in these variables will hence result in an even larger misprediction in the pressure drop. This fact will be illustrated comparing the following calculations:

- A:** When a priori knowledge about fluid properties, total mass flow rate and flowing vapor-fraction are used as friction-model input. This is the calculation from Chapter 9<sup>1</sup>, using the MATLAB code.
- B:** When only a priori knowledge about the fluid properties given at the boundaries<sup>2</sup> are used as friction-model input. This is the calculation using the COTT code.
- C:** When only a priori knowledge about the fluid properties and total mass flow is used as friction-model input. The value of the flowing vapor-fraction is taken from the calculation in B. This is calculated using the the MATLAB code.

<sup>1</sup>However, now the no-slip condition is used

<sup>2</sup>and the fluid properties in the rest of the domain is calculated by COTT



The resulting pressure drop are shown in Table 10.2.

Table 10.2: The pressure drop predicted by the Friedel model and the Cheng et al. model using different model-input parameters.

Cases	$\Delta p_{friedel}$ [bar]	$\Delta p_{cheng}$ [bar]
A	7.15	3.31
B	6.58	2.91
C	6.63	2.99

### 10.3 Discussion

Both when using the Friedel model and the Cheng et al. model, the frictional pressure-drop is found to be smaller when using the COTT code (case B) compared to the simple calculation done in Chapter 9 (case A). This is due to the effects illustrated in Figure 10.4 and the fact that several terms in the transport model, Equation (2.16), are coupled. The main reason is expected to be due to the underestimation of the flowing vapor-fraction when the COTT code is used (see Figure 10.4b). In Chapter 9 (case A) the flowing vapor-fraction,  $x$ , was found based on the measured saturated pressure at each location. In the COTT simulation (case B), the flowing vapor-fraction is specified at the western boundary, and in the rest of the domain the value of  $x$  is given by the pressure which is determined by the friction model. If the frictional pressure-drop is estimated to low (as is the case both in the Cheng et al. model and the Friedel model for experiment number 1), the flowing vapor-fraction will be underestimated.

By performing the same calculation as in Chapter 9, but with the lower flowing vapor-fraction predicted by COTT as input (case C), the resulting pressure drops are reduced (see Table 10.2). A difference of only 0.75 % and 2.7 % are found between case B and C for the Cheng et al. model and Friedel model, respectively. The remaining deviation is expected to be due to the difference in the the misprediction of the rest of the friction-model input variables (See Figure 10.4), the errors arising due to the linear interpolation made in Chapter 9, and the neglect of the heat transfer. This is an indication that, despite the deviating result between the COTT code (case B) and the results from Chapter 9 (case A), the Friedel and Cheng et al. model are most probably implemented correctly in the COTT code.

### 10.4 Summary and conclusions

In this chapter, the Cheng et al. model [8] and the Friedel model [8] are implemented in the DF3 model with the Span-Wagner EOS in the COTT code. The implementation is further compared with calculations using the results from Chapter 9. A difference of 8 – 12 % is found. However, this is expected to arise because the friction model and other sub models, such as the equation of state, are coupled in the COTT code.

This illustrates that the experiments carried out in [24], are not especially suitable for CFD-model verification.



# Chapter 11

## Transient effects of friction models

In order to investigate how friction may affect transient simulations, a test case is performed. How the wave speed is affected by the friction model and the associated slip-relation, will be explored.

### 11.1 Mathematical models used

The following mathematical models are used for all cases in this chapter:

**Transport model:** DF4 model, Equation (2.11)– (2.14)

**Slip model:** Linear slip, Equation (2.20) with  $S_s = 0$

**Friction model:** Friedel [20] and Cheng et al. [8] (see Section 5.3.2 and 5.3.3)

**EOS:** Stiffened gas with parameters adapted to CO<sub>2</sub> (see Section 3.3)

The objective is *not* to perform an exact calculation for transient CO<sub>2</sub>-flows, but instead get an indication of how friction models and slip-relation will affect the solution. Thus, for simplicity the more accurate Span-Wagner EOS will not be used

#### 11.1.1 Initial conditions

The initial conditions for all the simulations are given in Figure 11.1.

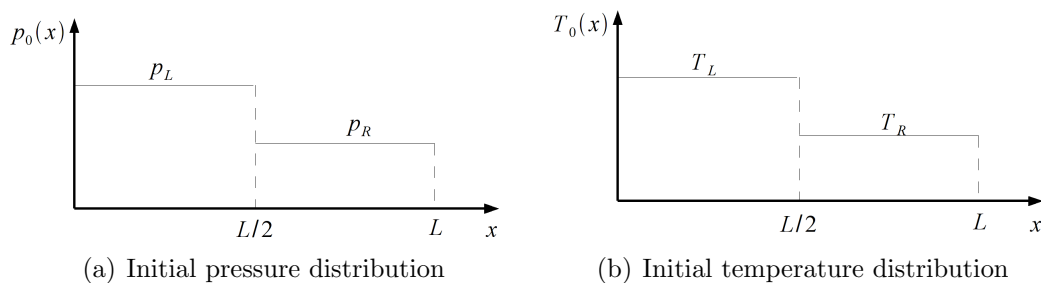


Figure 11.1: An initial pressure and temperature discontinuity is present in a CO<sub>2</sub> two-phase mixture at  $x = L/2$ .  $p_L = 60$  bar,  $p_R = 30$  bar,  $T_R = T_{sat}(p_R)$ ,  $T_L = T_{sat}(p_L)$  and  $L = 100$  m. Pipe diameter,  $d = 0.1$  m.

### 11.1.2 Boundary conditions

Since the objective is to investigate transient effect and not the effect of boundary conditions, extrapolating boundary conditions are used. The simulation is stopped before any of the waves have reached the boundaries.

### 11.1.3 Parameters for the stiffened-gas EOS

The constant parameters needed in the stiffened-gas equation of state are calculated based on the “speed of sound” procedure suggested in Section 3.3.

$p_0 = 45$  bar and  $T_0 = 283.13$  K is in the middle of the domain of interest ( $30 \text{ bar} < p < 60$  bar), and is thus chosen as the reference state. This is saturated  $\text{CO}_2$ . Fluid properties are obtained from the NIST web-book [1] and are listed in Table 11.1. The constant parameters used in the stiffened gas equation of state can then be calculated, and they are given in Table 11.2.

Be aware, because the the stiffened gas EOS is linearized, errors will occur when estimating the density and the speed of sound at pressures and temperatures different from the reference state  $(p_0, T_0)$ .

Table 11.1: Saturated  $\text{CO}_2$  properties at  $p_0=45$  bar used in the calculation of the parameters in the stiffened-gas equation of state. From NIST [1].

	Gas phase	Liquid phase
$\rho_0$ [kg/m <sup>3</sup> ]	135.07	861.27
$c_{p,0}$ [J/kgK]	2555.8	2996.3
$c_0$ [m/s]	205.42	441.16

Table 11.2:  $\text{CO}_2$ -adapted parameters used in the stiffened-gas EOS

	Gas phase	Liquid phase
$\gamma$	1.06	1.23
$c_v$ [J/kgK]	2414.97	2437.18
$p_\infty$ [Pa]	$8.855 \cdot 10^5$	$1.3184 \cdot 10^8$

### 11.1.4 Constant fluid properties

The viscosity and the surface tension is assumed constant in the stiffened gas EOS. The values used are given in Table 11.3.

Table 11.3: Saturation properties at  $p_{avg} = 45$  bar obtained from NIST [1].

	<b>Gas phase</b>	<b>Liquid phase</b>
Viscosity, $\mu$ [N/m <sup>2</sup> s]	$1.6055 \cdot 10^{-5}$	$8.2589 \cdot 10^{-5}$
Surface tension, $\sigma$ [N/m]		0.00276

### 11.1.5 Numerical setup

The mathematical model is solved numerically. The forward Euler method is used for time discretization and the MUSTA method is used for spatial discretization. The numerical parameters used are given in Table 11.4.

Table 11.4: The numerical parameters used in all the transient simulations

CFL- number	0.9
MUSTA sub steps	4
MUSTA- local cells	4

## 11.2 Cases

In this chapter, the cases run are given in Table 11.5. Case 1 will be compared with the wave speeds derived by Martinez et al. [15] in order to verify the solution. Case 2 and 3 will be used in order to obtain a qualitative understanding of the slip-dependent behavior of the wave speeds. Case 4 and 5 will be used in order to investigate how transient phenomena are affected by the friction model.

Table 11.5: Transient cases run

<b>Case</b>	<b>Slip, <math>K</math></b>	<b>Friction model:</b>
<b>1</b>	1	-
<b>2</b>	0.5	-
<b>3</b>	0.1	-
<b>4</b>	1	Friedel
<b>5</b>	1	Cheng et al.

## 11.3 Results for case 1

### 11.3.1 Grid refinement

Figure 11.2 shows how the solution converges as the grid is refined. As the number of grid cells is increased from 3000 to 5000, the result almost does not change and the solution is said to be grid independent.

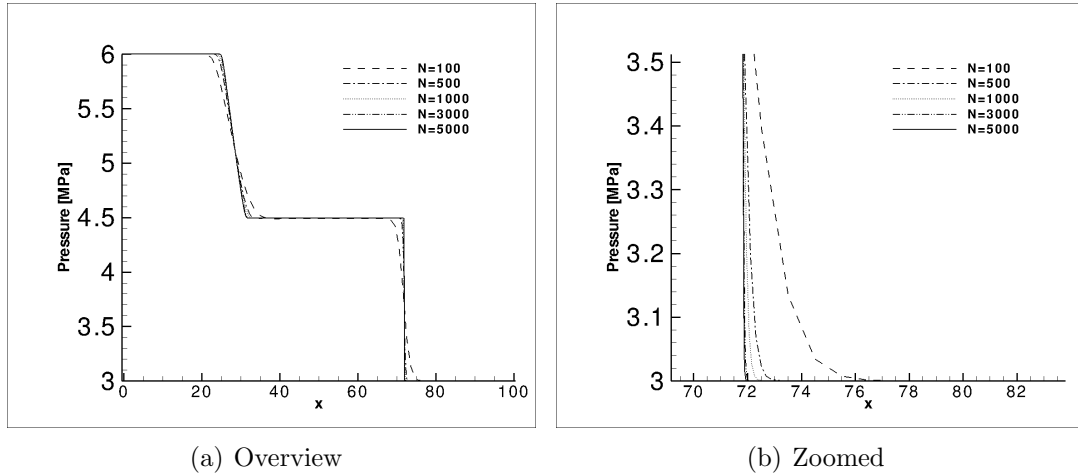


Figure 11.2: Grid refinement test for no-slip conditions

### 11.3.2 Physical behavior

The physical behavior is explained in Figure 11.3.

- a) Due to the initial pressure gradient, the fluid starts flowing at a velocity of about  $u_g = u_l = 20$  m/s in the positive  $x$ -direction.
- b) A rarefaction wave propagates to the left and reduces the pressure, and a shock wave propagates to the right and increases the pressure.
- c) The void fraction,  $\alpha$ , increases to the left and is reduced to the right because of the reduction and increase in pressure, respectively.
- d) The temperature will increase slightly in the regions where the pressure is increased, and decrease slightly in the regions where the pressure is decreased. In addition, the initial temperature discontinuity at  $L/2$  will propagate as a material wave.
- e) The gas density is high in the region where the pressure and temperature is high and low in the regions where the pressure and temperature is low.
- f) The liquid density is more sensitive to the temperature than the pressure, thus the density is higher to the left than to the right.

The DF4 model used assumes no mass transfer, thus the following will not be described in the results from this simulation:

- Change in the void fraction due to mass transfer
- Temperature drop/rise due to mass transfer (associated with the *heat of vaporization* which is released when vapor condensates)

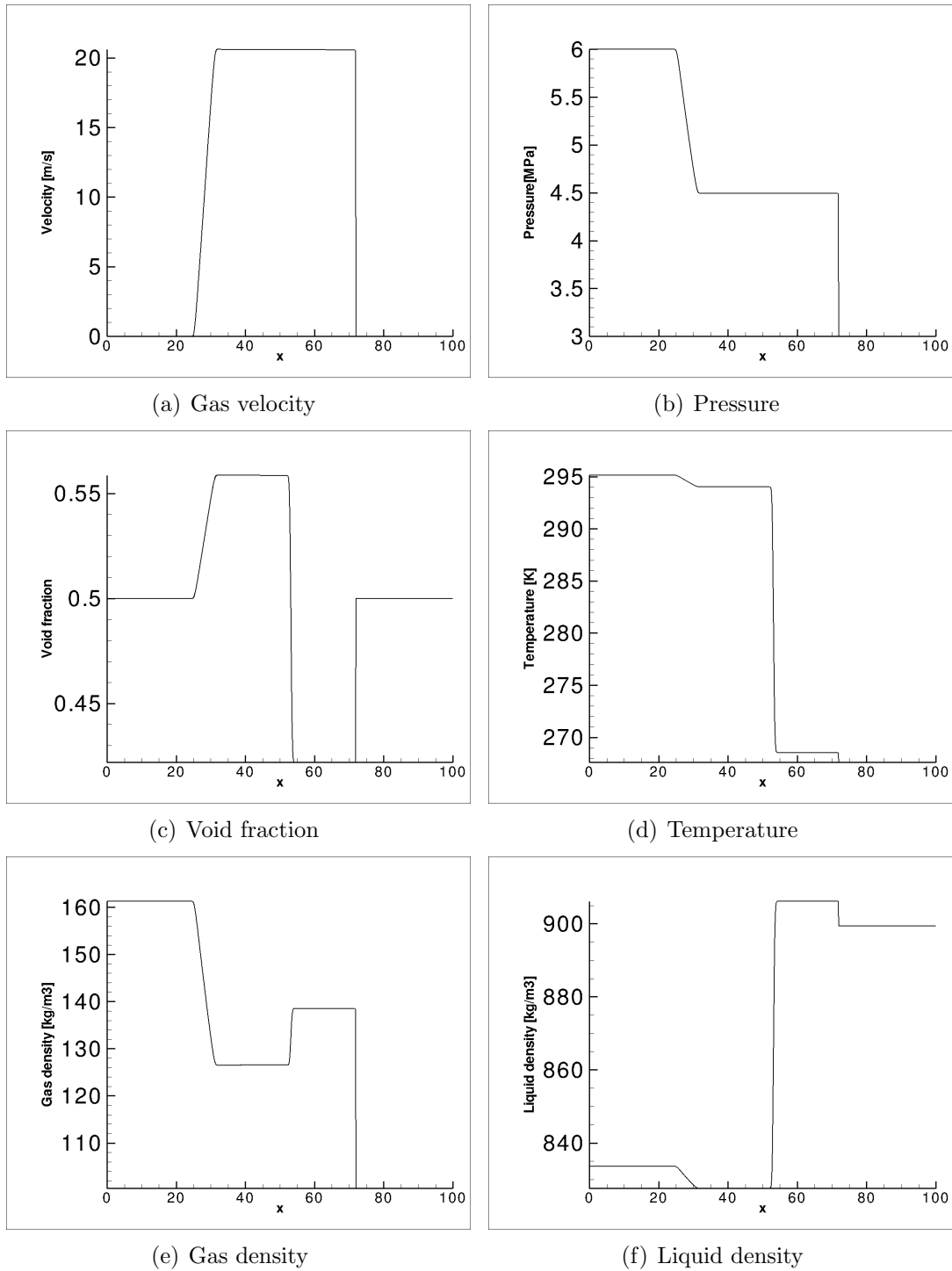


Figure 11.3: The physical behavior of the flow for no-slip conditions (case 1). Number of grid cells,  $N = 5000$ . All properties are plotted at  $t = 0.15$  s.

### 11.3.3 Eigenvalues

The length at which each wave has traveled after  $t = 0.15$  seconds can be measured, for instance in Figure 11.3d. The material wave has traveled 3.1 meters, the shock wave has traveled 22.1 meters and the rarefaction wave have traveled from 18.7 to 25.0 meters. This corresponds to the following average<sup>1</sup> wave velocities:

- Shock: 147.3 m/s
- Material: 20.7 m/s
- Rarefaction: 124.7 – 166.7m/s

The eigenvalues can also be calculated analytically by using Equation (2.31),  $\zeta_k$  as calculated in Equation (F.8), and the fluid properties as predicted by COTT for the specific case (see Figure 11.3). For details about the calculations see Appendix F.2.

#### Shock wave

In Section 2.4.2, we saw that the speed of the shock wave would be found within the following range:

$$\lambda(\mathbf{q}_L) > S_1 > \lambda(\mathbf{q}_R), \quad (11.1)$$

where  $\mathbf{q}_L$  and  $\mathbf{q}_R$  are to the left and the right of the wave respectively.

By using Equation (2.31), we find  $166.88 > S_s > 124.16$ . This agrees with the result from the simulation ( $S = 147.3$  m/s).

#### Rarefaction wave

In Section 2.4.2, we saw that the speed of the rarefaction wave would vary between  $\lambda(\mathbf{q}_L)$  and  $\lambda(\mathbf{q}^*)$ , which are the conditions to the left and right of the rarefaction wave respectively. When using Equation (2.31) we find :  $S_4 = 127.73$  to  $164.97$ . This is slightly different from the results obtained in the simulations ( $S=124.7-166.7$  m/s).

#### Material wave

In Section 2.4.2, we saw that the speed of the material wave would be equal to the eigenvalue which is equal to the current fluid velocity  $u = 20.6$  m/s. This is slightly lower than the results obtained in the average calculation performed ( $u = 20.7$ ).

The wave speeds calculated using Equation (2.31) are the instantaneous speeds. However, the wave speeds calculated from the visual readouts from the graph are averages between  $t = 0$  and  $t = 0.15$ . This is expected to be the main reason for the deviation.

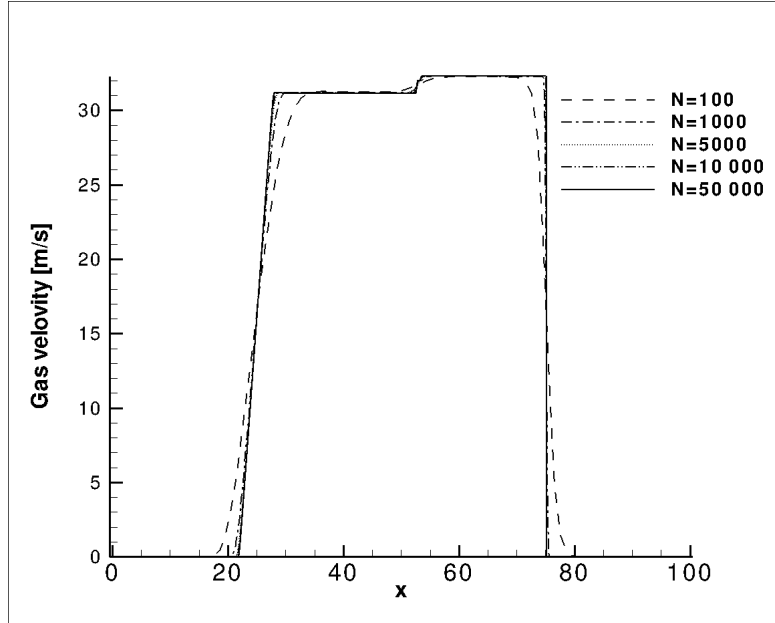
---

<sup>1</sup>between  $t = 0$  and  $t = 0.15$

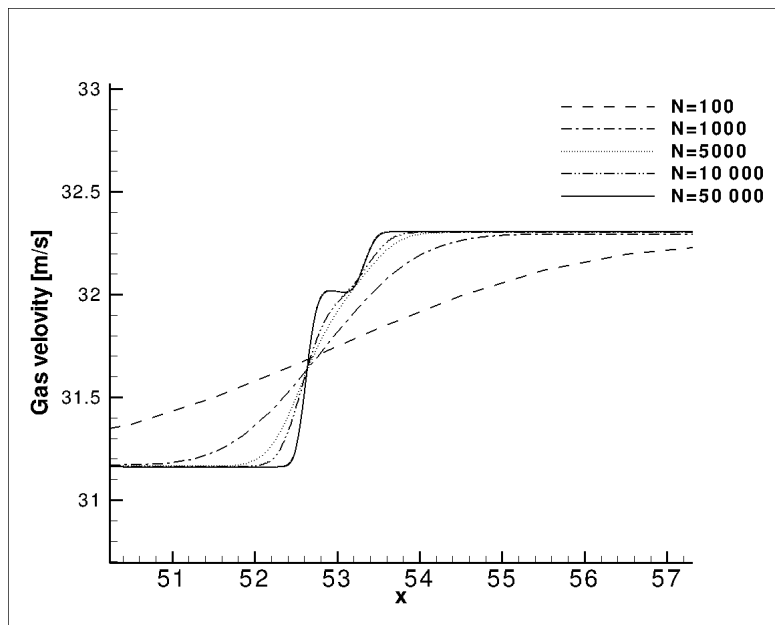


## 11.4 Results for case 2

At slip conditions, we expect the two material waves to have different velocities. However, the eigenvalues for this case are not derived analytically, instead this will be verified by performing a simulation in COTT. In Figure 11.4 the gas velocity at  $t = 0.15$  s for different grids is shown. As seen, the two material waves have almost the same speed, hence a very fine grid is needed in order to capture the difference.



(a) Overview

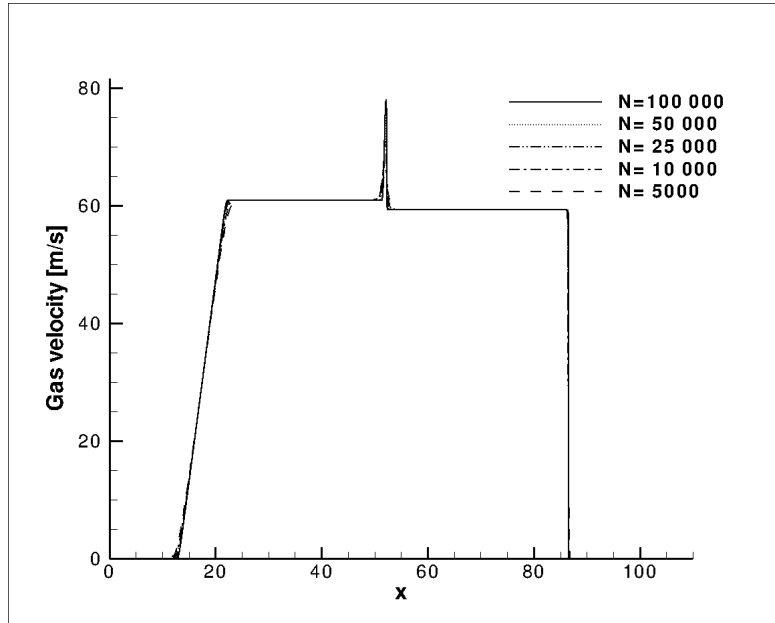


(b) Zoomed. Showing the two material waves

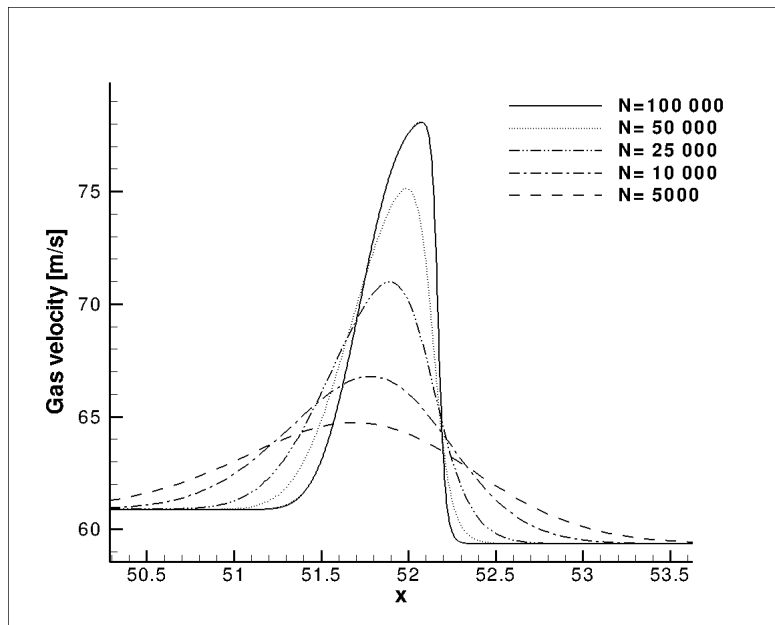
Figure 11.4: Gas velocity. Grid-refinement test for case 2.

## 11.5 Results for case 3

In test case 3 a slip constant of  $K = 0.1$  is used. This means that the gas velocity is forced to be 10 times higher than the liquid velocity. Compared to case 2, which only differ by a higher slip constant, the result is very different (see Figure 11.5). The fourth wave will now take the form of a “sharp increase” and is visible even on a somewhat coarse grid ( $N = 1000$ ).



(a) Overview



(b) Zoomed. Showing the two material waves

Figure 11.5: Grid-refinement test for case 3.

As seen from Figure 11.5, the solution around the material waves converges very slowly.

This can be explained by the following: The “wave-specific” CFL number<sup>2</sup> would vary in the domain. –The fastest going waves would be associated with a CFL-number of 0.9 (see Equation(4.8) and Table 11.4) and the slowest waves, would be associated with a CFL number much smaller than 0.9. Typically, the lower the CFL number is the more diffusive the numerical method will be. This would be the case for the material waves since these have very small velocities compared to the shock wave and the rarefaction wave.

## 11.6 Influence of slip relation

Case 1, 2 and 3 are plotted in the same figure in order to show the slip dependent behavior of the waves (see Figure 11.6 and 11.7). The shock wave can be recognized as the wave to the right, the material waves are the middle waves, and the rarefaction wave is the wave to the left. As seen from the plot, the absolute value of the wave speed decreases for the rarefaction wave and the shock wave as  $K$  is increased. Because of the very different behavior of the material waves in case 2 and 3, the slip dependence of these waves will not be analyzed any further.

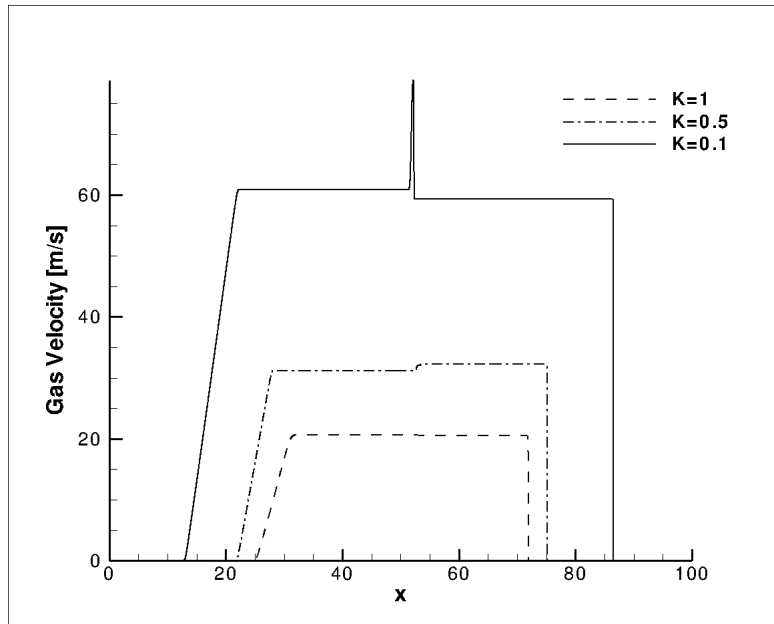


Figure 11.6: Case 1, 2 and 3 at  $t = 0.15$  s. Gas velocity decreases as  $K$  is increased.

<sup>2</sup>Replace  $\lambda_{max}$  in Equation(4.8) with the wave speed of interest

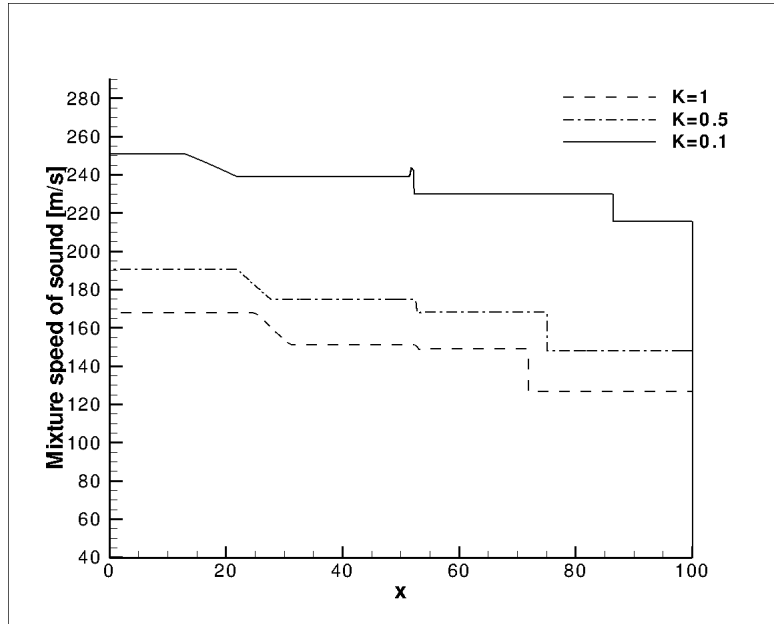


Figure 11.7: Case 1, 2 and 3 at  $t = 0.15$  s. Mixture speed of sound decreases as  $K$  is increase

As mentioned in Section 2.4, Evje and Flåtten [14] made an estimation of the wave velocities at slip condition for the DF4 model where the energy equation is excluded.

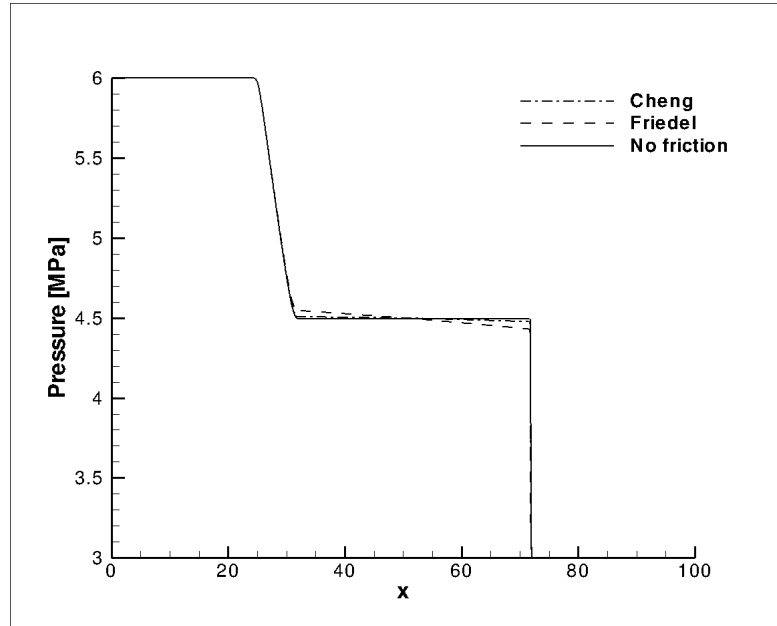
$$\mathbf{\Lambda} = \begin{bmatrix} u_{p1} - c_{DF4*} \\ u_{p2} \\ u_{p1} + c_{DF4*} \end{bmatrix}, \quad (11.2)$$

where  $c_{DF4*}$  is the mixture speed of sound computed according to [14], and shown in Figure 11.7. As seen from Figure 11.7, the mixture speed of sound is reduced as  $K$  is increased. This is the main reason why the velocity of the shock speed and the rarefaction speed are reduced as  $K$  is increased.

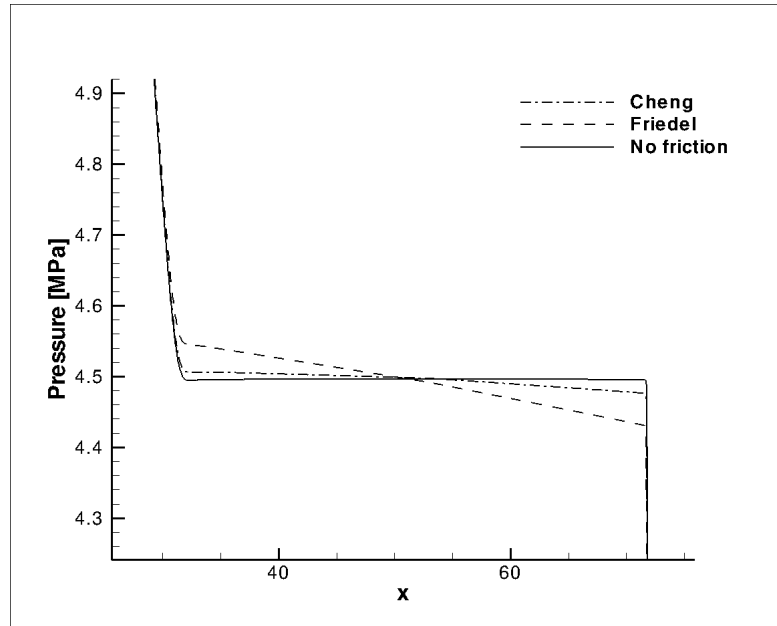
## 11.7 Friction-model effects

In this section, case 4 and 5 are compared in order to get an understanding of how different friction model may affect the solution. In case 4 the Friedel model [20] is used, and in case 5 the Cheng et al. model [8] is used.

The pressure distribution is plotted in Figure 11.8. As seen from the plot, in the region where the fluid is flowing a pressure gradient will arise due to the friction effect. For these specific flow conditions, the friction predicted by the Cheng et al. model is smaller than predicted by the Friedel model. The slope of the pressure curve is thus different for the two models.



(a) Overview pressure

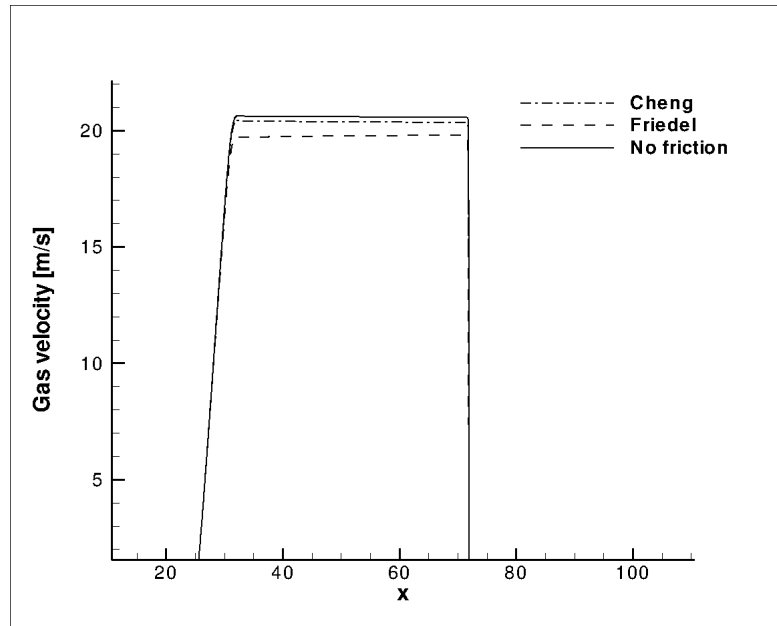


(b) Zoomed, - the region where the velocity is non-zero

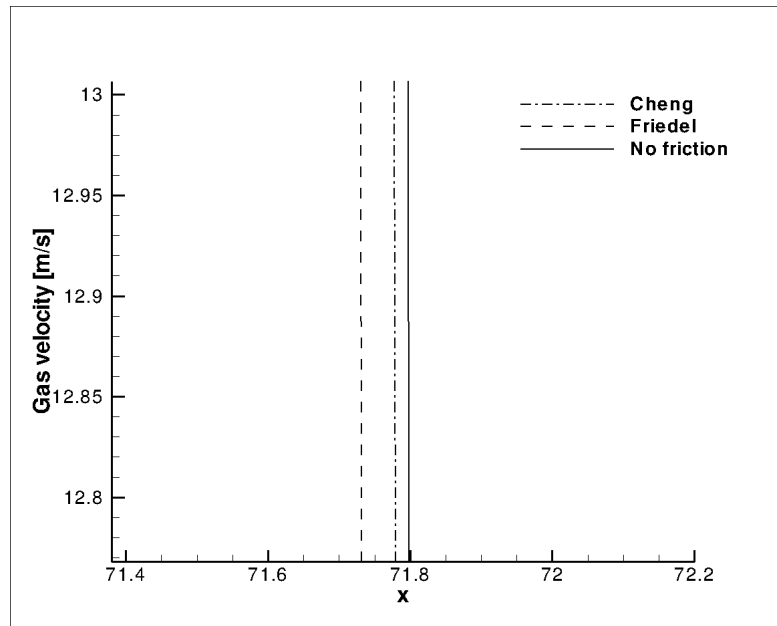
Figure 11.8: Case 4 and 5. Plotted with  $N = 3000$  at  $t = 0.15$  s.

The larger the pressure gradient, the smaller the pressure difference will be across the waves (see e.g. the right going shock wave in Figure 11.8). This will result in a lower driving force, and thus a smaller velocity. This is verified in Figure 11.9a. The velocity is the highest in the case of frictionless flow, and the velocity is the lowest when the Friedel model is used.

Since the wave speeds are functions of the fluid velocity (see Equation (2.36)), they will also be affected by the friction model. As seen from Figure 11.9b, the shock speed is higher using the Cheng et al. model than the Friedel model, and even higher when no friction condition is applied.



(a) Overview, velocity



(b) Zoomed, - the right going wave

Figure 11.9: Case 4 and 5. Plotted with  $N = 3000$  at  $t = 0.15$  s.

The flow pattern predicted by the Cheng et al. model is shown in Figure 11.10. As seen from the figure, in the region where the fluid is not yet flowing, the flow pattern would be stratified. In the region where the fluid is flowing the flow pattern is predicted to be mostly Intermittent (and close to the left-going wave, the flow is stratified wavy/slug).

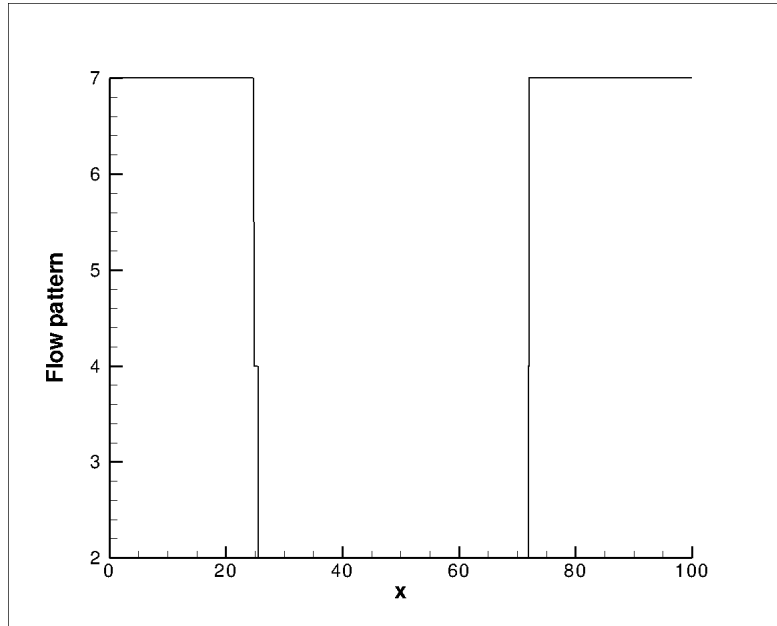


Figure 11.10: Case 5. Flow pattern predicted by Cheng et al.. Where the following flow-pattern coding is used: 1- annular, 2-intermittent, 3- stratified wavy, 4- stratified wavy/slug, 5- mist, 6- dry-out, 7- stratified, 8- bubbly. Plotted with  $N = 3000$  at  $t = 0.15$  s.

## 11.8 Summary and conclusions

In this chapter:

- We have studied a transient case and tried to explain the physical behavior of the waves at no-slip conditions.
- We have verified the observed wave velocities with analytical relations given by Martinez et al. [15].
- We have studied the effect of slip (which is a part of the friction model) and how it introduces a fourth material wave. A very fine grid was needed in order to capture the material waves. This is expected to be due to the diffusive behavior of the MUSTA method for the slow going waves.
- We have seen how the slip relation will affect the wave speeds. As the slip is increased ( $K_s$  is reduced), the absolute speed of the shock wave and the rarefaction wave will increase. This is expected to be mainly due to the increase of the mixture speed of sound.
- Finally, we have seen how the wave speeds are affected by the friction model directly. This is mainly because the velocity depends on the pressure gradient. However, the main effect of the friction model is the pressure gradient arising where the velocity is non-zero.





# Chapter 12

## Conclusions and further work

Three questions were asked in Section 1.2. The main conclusions and the further work are summarized below.

### Friction-model comparison

A homogenous friction-model, the Friedel model [20], and the Cheng et al. model [8] have been compared with six steady-state frictional-pressure-drop experiments for pure CO<sub>2</sub> [24]. The Friedel model was found to be the most accurate model with a relative standard deviation of 9.7 % versus 55.74 % for the Cheng et al. model and 29.18 % for the homogenous model. The homogenous model underestimates the frictional pressure-drop for all experiments [24], and the Cheng et al. model underestimates the frictional pressure drop for the low vapor-fraction experiments.

Thus, this is an indication that the significance of CO<sub>2</sub>-specific insight (which is exploited in the Cheng et al. model) is relatively small compared to the importance of a larger database of data (which is advantage of the Friedel model).

The calculated relative standard deviation for the Friedel model (9.7 %) was found to be much lower than the relative standard deviation for the large pressure-drop database used by Friedel (32 %). This may be an indication that the Friedel model is just as suitable for predicting the pressure drop in CO<sub>2</sub> as for other fluids.

It should be noted that an absolute conclusion are hard to make based only on six experiments. It would have been interesting to include more experimental data in this analysis in order to verify the observed trends. In particular, it would have been of interest to compare the model with conditions more similar to what would be the case in typical CCS pipes (see e.g. Appendix D). That means larger pipes and in the presence of impurities.

### Friction models performance in the complete CO<sub>2</sub>-transport model

The selected friction models were implemented into the COTT code with the DF3 model and the DF4 model, using the Span-Wagner EOS and stiffened gas EOS, respectively. One of the experiments in [24] was reproduced. The implementation was further compared with the

calculations from Chapter 9. A difference of 8–12 % was found. However, this was expected to arise because the friction model and other sub models, such as the equation of state, are coupled in the COTT code. The results illustrate how the accuracy of the friction model is even more important when used as a part of a complete transport-model. Besides this, it exemplifies why the experiments carried out in [24], are not particularly suitable for CFD-model verification.

### Transient effects of friction models

In the case of a transient flow, the influence of the friction model and the associated slip relation, was explored. A very fine grid was needed in order to capture the material waves. This is expected to be due to the diffusive behavior of the numerical method of MUSTA for the slow waves. It was shown that wave speeds depended strongly on the slip relation used. As the slip constant,  $K_s$ , was reduced the speed of the shock wave and the rarefaction wave increased. This is expected to be mainly due to the increase of the mixture speed of sound.

The friction model itself will indirectly affect the wave speed. This is mainly because of the reduced driving force across the wave and hence a reduction in the fluid velocity. However, the main effect of the friction model is the pressure gradient arising in regions where the velocity is non-zero.

Most frictional-pressure-drop models are derived for steady-state conditions, but the application is here extended to transient situations. The accuracy of this assumption should be verified by making use of experimental data.

### Further work

- Compare the Friedel model and the Cheng et al. model with conditions more similar to what is the case in typical CCS applications. That means larger pipes and under conditions where impurities are present.
- Compare the friction models with transient experiments.
- Implement slip in the “DF3 – Span-Wagner” model. This will result in a more accurate CO<sub>2</sub> transport-model, and the friction model of Cheng et al. can be used without simplifications. An iterative procedure is probably needed in order to do this. Thus, it is expected to be relatively computationally expensive.
- A more detailed investigation of the slow material waves arising in the DF4 model. This can be done by a further refinement of the grid, or by making use of a less diffusive numerical method, such as the Roe method (see e.g. [38, Ch. 11]).
- In order to predict the flowing vapor-fraction for the steady-state simulation in Chapter 10 better, a heat transfer model can be implemented in the “DF3 – Span-Wagner” model.
- Investigate how the selected wall-friction models can be exploited in a two-fluid model.

# Bibliography

- [1] Nist chemistry webbook. <http://webbook.nist.gov/chemistry/>, 2012. Online: accessed 9-May-2012.
- [2] F. Aakenes. Multiphase flow modelling and prediction of flow regime and frictional pressure drop for pipeline transport of carbon dioxide. Project report, NTNU, 2011.
- [3] International Energy Agency. World energy outlook 2010. <http://www.worldenergyoutlook.org/media/weo2010.pdf>, 2010.
- [4] D. Biberg. An explicit approximation for the wetted angle in two-phase stratified pipe flow. *The Canadian Journal of Chemical Engineering*, 77:1221–1224, 1999.
- [5] C. E. Brennen. *Fundamentals of Multiphase Flow*. Cambridge, 2005.
- [6] V. P. Carey. *Statistical Thermodynamics and Microscale Thermo physics*. Cambridge University Press, 1999.
- [7] L. Cheng. University of Portsmouth. Personal communication, 2012.
- [8] L. Cheng, G. Ribatski, J. M. Quiben, and J. R. Thome. New prediction methods for CO<sub>2</sub> evaporation inside tubes: Part 1- a two-phase flow pattern map and a flow pattern based phenomenological model for two-phase flow frictional pressure drops. *Int. Journal of Heat and Mass Transfer*, 51:111–124, 2008.
- [9] L. Cheng, G. Ribatski, and J. R. Thome. New prediction methods for CO<sub>2</sub> evaporation inside tubes: Part 2- an updated general flow boiling heat transfer model based on flow patterns. *Int. Journal of Heat and Mass Transfer*, 51:125–135, 2006.
- [10] J. G. Collier and J. R. Thome. *Convective boiling and condensation*. Oxford Science Publications, 3rd edition, 1994.
- [11] G. de Koeijer, J. H. Borch, M. Drescher, H. Li, Ø. Wilhelmsen, and J. Jakobsen. CO<sub>2</sub> transport and depressurization, heat transfer and impurities. *Energy Procedia*, 4:3008 – 3015, 2011.
- [12] G. de Koeijer, J. H. Borch, J. Jakobsen, and M. Drescher. Experiments and modeling of two-phase transient flow during CO<sub>2</sub> pipeline depressurization. *Energy Procedia*, 1(1):1683 – 1689, 2009.
- [13] M. Drescher. Sintef. Personal communication, 2012.
- [14] S. Evje and T. Flåtten. On the wave structure of two-phase flow models. *SIAM Journal of Applied Mathematics*, 67(2):487–511, 2007.

- [15] P. J. Martinez Ferrer, T. Flåtten, and S. T. Munkejord. On the effect of temperature and velocity relaxation in two-phase flow models. *ESAIM: Mathematical Modelling and Numerical Analysis*, 46(2):411–442, 2012.
- [16] T. Flåtten and H. Lund. CO<sub>2</sub> dynamics notebook. Technical memo, SINTEF Energy Research, 2010.
- [17] T. Flåtten and H. Lund. Relaxation two-phase flow models and the subcharacteristic condition. *Mathematical Models and Methods in Applied Sciences*, 21:2379–2470, 2011.
- [18] The Carbon Sequestration Leadership Forum. CO<sub>2</sub> transportation -is it safe and reliable? Technical report, The Carbon Sequestration Leadership Forum (CSLF), 2011.
- [19] The Carbon Sequestration Leadership Forum. Why carbon capture and storage? Technical report, The Carbon Sequestration Leadership Forum (CSLF), 2011.
- [20] L. Friedel. Improved friction pressure drop correlation for horizontal and vertical two phase pipe flows. In *European two phase flow group meeting, Ispra, 5-8 June 1979*, 1979.
- [21] K. E. T. Giljarhus, S. T. Munkejord, and G. Skaugen. Solution of the Span-Wagner equation of state using a density-energy state function for fluid-dynamic simulation of carbon dioxide. *Industrial and Engineering Chemistry Research*, 51(2):1006–1014, 2012.
- [22] Global CCS Institute. The global status of CCS: 2011. Technical report, Global CCS Institute, 2011.
- [23] Pipelines International. Transport of CO<sub>2</sub> for carbon capture and storage. [http://pipelinesinternational.com/news/transport\\_of\\_co2\\_for\\_carbon\\_capture\\_and\\_storage/040204/#](http://pipelinesinternational.com/news/transport_of_co2_for_carbon_capture_and_storage/040204/#), 2011. Online; accessed 9-May-2012.
- [24] J. P. Jakobsen, G. Skaugen, A. Austegard, A. Hafner, and M. Drescher. CO<sub>2</sub> pipeline test rig: Experiments and simulation. model verification. Technical report, SINTEF Energy Research, 2008. Restricted.
- [25] R. J. Leveque. *Finite Volume Methods for Hyperbolic Problems*. Cambridge, 2002.
- [26] R. Menikoff. Empirical equations of state for solids. In Yasuyuki Horie, editor, *Shock-Wave Science and Technology Reference Library*, pages 143–188. Springer Berlin Heidelberg, 2007.
- [27] R. J. Moffat. Describing the uncertainties in experimental results. *Experimental Thermal and Fluid science*, 1:3–17, 1988.
- [28] M. J. Moran and H. N. Shapiro. *Fundamentals of engineering thermodynamics*. John Wiley and Sons, Inc, 5th edition, 2006.
- [29] S. T. Munkejord. *Analysis of the two-fluid model and the drift-flux model for numerical calculation of two-phase flow*. PhD thesis, NTNU, 2005.
- [30] S. T. Munkejord, S. Evje, and T. Flåtten. A MUSTA scheme for a nonconservative two-fluid model. *Journal of Scientific Computing*, 31:2587–2622, 2009.

- [31] Intergovernmental Panel on Climate Change. Climate change 2007: Synthesis report. Technical report, Intergovernmental Panel on Climate Change (IPCC), 2007.
- [32] J. M. Quiben and J. R. Thome. Flow pattern based two-phase frictional pressure drop model for horizontal tubes, part 1: Diabatic and adiabatic experimental study. *Int. Journal of Heat and Fluid Flow*, 28:1049–1059, 2007.
- [33] J. M. Quiben and J. R. Thome. Flow pattern based two-phase frictional pressure drop model for horizontal tubes, part 2: New phenomenological model. *Int. Journal of Heat and Fluid Flow*, 28:1060–1072, 2007.
- [34] S. Z. Rouhani and E. Axelsson. Calculation of void volume fraction in the subcooled and quality boiling regions. *Int. Journal of Heat and Mass Transfer*, 13:383–393, 1969.
- [35] J. Serpa, J. Morbee, and E. Tzimas. Technical and economical characteristics of CO<sub>2</sub> transmission pipeline infrastructure. Technical report, JRC Scientific and Technical Reports, European Commission, 2011.
- [36] R. Span and W. Wagner. A new equation of state for carbon dioxide covering the fluid region from the triple-point temperature to 1100 K at pressures up to 800 MPa. *Journal of Physics and Chemistry*, 25:1509–1588, 1996.
- [37] J. R. Thome. Engineering data book 3. <http://www.wlv.com/products/databook/db3/DataBookIII.pdf>, 2010.
- [38] E. F. Toro. *Riemann Solvers and Numerical Methods for Fluid Dynamics*. Springer, 3rd edition, 2008.
- [39] E.F. Toro. MUSTA: A multi-stage numerical flux. *Applied Numerical Mathematics*, 56:1464–1479, 2006.
- [40] F. M. White. *Fluid Mechanics*. McGraw Hill, 6th edition, 2008.
- [41] N. Zuber and J.A. Findlay. Average volumetric concentration in two-phase flow systems. *Journal of Heat Transfer*, 87:453–462, 1965.



# Appendix A

## Zuber-Findlay slip relation

The Zuber-Findlay slip relation is given by [41, Eq. (32)]:

$$\boxed{u_g = K_s \cdot j + S_s}, \quad (\text{A.1})$$

where  $j$  is the total volumetric flux.

### A.1 Manipulation of the Zuber-Findlay slip relation

#### A.1.1 Written in terms of the slip

Defining the slip  $\phi \equiv u_g - u_l$  and substituting  $u_l = u_g - \phi$  into Equation (A.1), an alternative form of Equation (A.1) is obtained:

$$\phi = \frac{u_g(K_s - 1) + S_s}{K_s \alpha_l} \quad (\text{A.2})$$

#### A.1.2 Written in a dimensionless form

By defining  $\beta$ :

$$\beta = \frac{\alpha_g u_g}{\alpha_g u_g + \alpha_l u_l} = \frac{j_g}{j} \quad (\text{A.3})$$

and rearranging, the dimensionless form of Equation (A.1) is obtained:

$$\frac{\beta}{\alpha} = K_s + S_s/j \quad (\text{A.4})$$

#### A.1.3 Written in terms of the total mass velocity, $G$

Writing Equation (A.1) in terms of the liquid velocity, we get:

$$u_l = \frac{1}{\alpha_l} \left( \frac{u_g - S_s}{K_s} - \alpha_g u_g \right) \quad (\text{A.5})$$

This is substituted into the definition of the total mass velocity:

$$G \equiv \alpha_g u_g + \alpha_l u_l = \alpha_g u_g + \alpha_l \frac{1}{\alpha_l} \left( \frac{u_g - S_s}{K_s} - \alpha_g u_g \right) \quad (\text{A.6})$$

Further, this can be solved for the gas velocity, and the following relation is obtained:

$$u_g = \frac{G + \rho_l S_s / K_s}{\alpha_g \rho_g + \rho_l (\alpha_l - (K_s - 1) / K_s)} \quad (\text{A.7})$$

#### A.1.4 Written in terms of the void fraction

Substituting the equation for the gas velocity,

$$u_g = \frac{Gx}{\rho_g \alpha_g}, \quad (\text{A.8})$$

into the definition of  $\beta$ , Equation (A.3), we get:

$$\beta = \frac{x / \rho_g}{x / \rho_g + (1 - x) / \rho_l}. \quad (\text{A.9})$$

Further this result is substituted into Equation (A.4) and solved for  $\alpha$ :

$$\alpha = \frac{x}{\rho_g} \left[ \frac{x}{\rho_g} + \frac{1 - x}{\rho_l} \right]^{-1} \left[ K_s + S_s / j \right]^{-1} \quad (\text{A.10})$$

Using the fact that  $j = G / \rho_{mix}$  where  $\rho_{mix} = (x / \rho_g + (1 - x) / \rho_l)^{-1}$ , we get:

$$\alpha = \frac{x}{\rho_g} \left[ K_s \left( \frac{x}{\rho_g} + \frac{1 - x}{\rho_l} \right) + S_s / G \right]^{-1} \quad (\text{A.11})$$

This is the equation used by Cheng et al. [8, Eq. (8)], where the Rouhani-Axelsson definition of the constants  $K_s$  and  $S_s$  are used, given by:

$$K_s = 1 + 0.12(1 - x), \quad (\text{A.12})$$

and

$$S_s = 1.18(1 - x) \left[ \frac{g\sigma(\rho_L - \rho_G)}{\rho_L^2} \right]^{1/4}. \quad (\text{A.13})$$



# Appendix B

## Implementation of the Rouhani-Axelsson version of the Zuber-Findlay slip relation

When using the COTT code, we have to be able to solve for the liquid velocity and gas velocity, when only the following variables are given: The gas density ( $\rho_g$ ), the liquid density ( $\rho_l$ ), the volume fractions ( $\alpha_g$  and  $\alpha_l$ ) and the total mass velocity  $G$ .

The Zuber-Findlay slip-model on the form given by Equation (A.7), will be used. The Rouhani-Axelsson definition of  $K_s$  and  $S_s$ , given by Equation (A.12) and (A.13), are used. This will be solved for using an iterative procedure:

1. Use  $u_l$  from the previous time step as a first guess
2. Calculate the flowing vapor-fraction,

$$x = \frac{u_g \rho_g \alpha_g}{G}. \quad (\text{B.1})$$

3. Calculate the Rouhani-Axelsson slip constants using Equation (A.12) and (A.13)
4. Calculate the gas velocity using Equation (A.7)
5. Calculate the liquid velocity using  $u_l = u_g - \phi$ , where  $\phi$  is given by Equation (A.2)
6. Use the calculated liquid velocity and repeat procedure until convergence



# Appendix C

## Implementation of boundary conditions

**Western boundary conditions in the DF3 model used in Chapter 10:**

Based on the flowing vapor-fraction,  $x$ , pressure,  $p$  and mass velocity,  $G$ , the following have to be computed:

- Gas and liquid density
- Volume fraction
- Velocity
- Temperature

This will be done using the following procedure:

- Extrapolate pressure
- Find the liquid density, gas density, and temperature at the extrapolated pressure based on the EOS
- Compute the void fraction,  $\alpha$ , based on the relevant slip-model used and the specified vapor fraction,  $x$ :

*If the linear slip-model is used:*

$$\alpha_G = \left[ \left( \frac{1-x}{x} \right) \frac{\rho_G}{\rho_L} \frac{1}{K_s} + 1 \right]^{-1} \quad (\text{C.1})$$

*If the Zuber-Findlay slip model is used:*

$$\alpha_G = \frac{x}{\rho_G} \left[ K_s \left( \frac{x}{\rho_G} + \frac{1-x}{\rho_L} \right) + \frac{S_s}{G} \right]^{-1} \quad (\text{C.2})$$

- Compute the gas velocity and liquid velocity based on the volume fraction, the flowing vapor-fraction and the total mass velocity ( $G$ ):

$$u_i = \frac{Gx_i}{\alpha_i\rho_i} \quad (\text{C.3})$$



# Appendix D

## Typical CO<sub>2</sub>-transport pipes

Table D.1: Typical operating conditions for a CO<sub>2</sub> transport pipe [35].

Diameter [m]	$d$	0.2-0.8
Pressure [bar]	$p$	100-200
Mass velocity [kg/m <sup>2</sup> s]	$G$	1000-1500
Length [km]	$L$	100-1000



# Appendix E

## Speed of sound for the stiffened gas EOS

The speed of sound is defined as:

$$c^2 = \left. \frac{\partial p}{\partial \rho} \right|_s \quad (\text{E.1})$$

The pressure is given as a function of the temperature and density,  $p = p(\rho, T)$ . Hence the total derivative of  $p$  is:

$$\partial p = \left. \frac{\partial p}{\partial \rho} \right|_T \partial \rho + \left. \frac{\partial p}{\partial T} \right|_\rho \partial T \quad (\text{E.2})$$

Dividing by  $\partial \rho$  at constant entropy, we get:

$$\left. \frac{\partial p}{\partial \rho} \right|_s = \left. \frac{\partial p}{\partial \rho} \right|_T + \left. \frac{\partial p}{\partial T} \right|_\rho \left. \frac{\partial T}{\partial \rho} \right|_s \quad (\text{E.3})$$

From Equation (3.17) we have:

$$\left. \frac{\partial p}{\partial \rho} \right|_T = (\gamma - 1)c_v T = \frac{p + p_\infty}{\rho}, \quad (\text{E.4})$$

$$\left. \frac{\partial p}{\partial T} \right|_\rho = (\gamma - 1)c_v \rho = \frac{p + p_\infty}{T}, \quad (\text{E.5})$$

and from Equation (3.19) we have:

$$\left. \frac{\partial T}{\partial \rho} \right|_s = \frac{T(\gamma - 1)}{\rho} \quad (\text{E.6})$$

By substituting Equation (E.4), (E.5) and (E.6) into (E.3), we get:

$$c^2 = \gamma(\gamma - 1)c_v T = \frac{(p + p_\infty)\gamma}{\rho} \quad (\text{E.7})$$

Often the definition of  $\gamma = c_p/c_v$  is used in order to simplify this equation even more. Thus:

$$c^2 = (\gamma - 1)c_p T \quad (\text{E.8})$$





# Appendix F

## Eigenvalues for the DF4 model

### F.1 The parameter $\zeta$

In order to find the eigenvalues of the DF4 model in the case of no slip, the parameter  $\zeta$  has to be derived. (See Section 2.4)

$$\zeta_k = -\frac{1}{\rho_k^2} \left( \frac{\partial \rho_k}{\partial s_k} \right)_p \quad (\text{F.1})$$

We have  $s = s(\rho, T)$ , hence the total differential of  $s$  is:

$$\partial s = \left. \frac{\partial s}{\partial \rho} \right|_T \partial \rho + \left. \frac{\partial s}{\partial T} \right|_\rho \partial T \quad (\text{F.2})$$

Dividing by  $\partial \rho$  and evaluate at constant pressure, we get:

$$\left. \frac{\partial s}{\partial \rho} \right|_p = \left. \frac{\partial s}{\partial \rho} \right|_T + \left. \frac{\partial s}{\partial T} \right|_\rho \left. \frac{\partial T}{\partial \rho} \right|_p \quad (\text{F.3})$$

**When the stiffened-gas EOS is used:**

From Equation (3.19), we have:

$$\left. \frac{\partial s}{\partial \rho} \right|_T = -\frac{c_v}{\rho} (\gamma - 1) \quad (\text{F.4})$$

and

$$\left. \frac{\partial s}{\partial T} \right|_\rho = \frac{c_v}{T}. \quad (\text{F.5})$$

From Equation (3.17), we have:

$$\left. \frac{\partial T}{\partial \rho} \right|_p = -\frac{T}{\rho} \quad (\text{F.6})$$

By substituting the above three equations into Equation (F.3), we get:

$$\left. \frac{\partial s}{\partial \rho} \right|_p = -\frac{c_v \gamma}{\rho} \quad (\text{F.7})$$

Thus,

$$\zeta_k = -\frac{1}{\rho_k^2} \left( \frac{\partial \rho_k}{\partial s_k} \right)_p = \frac{1}{\rho_k^2} \frac{1}{\frac{c_v \gamma}{\rho}} = \frac{1}{\rho \gamma c_v} = \frac{1}{\rho c_p} \quad (\text{F.8})$$

## F.2 Calculations used in Section 11.3.3

The instantaneous eigenvalues at  $t = 0.15$  can be calculated by using Equation (2.31),  $\zeta_k$  as calculated in Equation (F.8), and the fluid properties as predicted by COTT for the specific case (given in Figure 11.3). The results for the four different regions are given in the table below.

Table F.1: Fluid properties, and the corresponding calculated eigenvalues, in the four different regions in the domain. Fluid properties are obtained from the COTT simulation and the eigenvalues are further calculated using Equation (F.8).

	<b>Left</b>	<b>Left – middle</b>	<b>Right – middle</b>	<b>Right</b>
$u$ [m/s]	0	20.6	20.6	0
$p$ [bar]	60	45	45	30
$T$ [K]	295.13	294	268.5	267.6
$\alpha$	0.5	0.56	0.42	0.5
$c_{mix}$ [m/s]	164.97	148.33	146.28	124.16
$\lambda_1$ [m/s]	164.97	168.93	166.88	124.16
$\lambda_2$ [m/s]	0	20.6	20.6	0
$\lambda_3$ [m/s]	0	20.6	20.6	0
$\lambda_4$ [m/s]	-164.97	-127.73	-125.68	-124.16

# Appendix G

## The experiments [24]

EXPNR	TT-30 (C)	TT-40 (C)	TT-50 (C)	TT-60 (C)	PIT-30 (bar)	PIT-40 (bar)	PIT-50 (bar)	PIT-60 (bar)
1	13.19	10.76	8.3	5.96	48.47	45.8	42.97	40.33
2	8.69	6.98	5.35	3.83	43.37	41.72	39.88	38.16
3	12.4	10.04	7.52	5.26	47.65	45.14	42.28	39.64
4	16.31	13.62	10.55	7.76	52.36	49.13	45.51	42.26
5	16.92	14.01	10.69	7.59	53.04	49.54	45.59	42.05
6	15.51	13.02	10.68	8.56	51.2	48.33	45.56	43.07

Figure G.1: The logged temperature and pressure along the test-section. See Figure 7.1

EXPNR	TT-20 (C)	PT-20 (bar)	TT-122 (C)	TT-123 (C)	FE-10 (kg/min)	FE-20 (kg/min)	TT-120 (C)	TT-121 (C)
1	3.37	66.82	28.53	2.9	1.9	5.93	11.52	11.35
2	10.02	60.38	27.02	9.51	1.22	3.76	11.45	11.28
3	2.49	60.51	22.78	1.83	2.86	3	8.98	10.5
4	0.27	56.93	20.07	-0.19	4.68	1.61	11.11	12.4
5	9.98	54.78	18.55	-0.13	4.96	1.73	13.16	15.21
6	6.66	55.77	22.35	6.21	3.85	1.27	13.18	14.85

Figure G.2: The temperature and pressure before the throttling valves, the mass flow rates and the surrounding temperature (TT-120 and TT-121).

EXPNR	PDT-41 (bar)	PDT-61 (bar)
1	2.71	8.2
2	1.72	5.2
3	2.63	8.02
4	3.32	10.07
5	3.58	11.03
6	2.93	8.17

Figure G.3: The Pressure drop between position 1 and 2, and 1 and 4. See Figure 7.1



# Appendix H

## The implementation of the Cheng et al. flow-pattern map

The idea behind the implementation of the Cheng et al. flow pattern model is described by Figure H.1, H.2 and H.3.

The different transition lines, labeled  $G_{SWS}$ ,  $G_{SW}$ ,  $G_S$ ,  $G_D$ ,  $G_M$ ,  $x_{LA}$  and  $G_B$ , are drawn based on the correlations given in [8] (see Figure H.1).

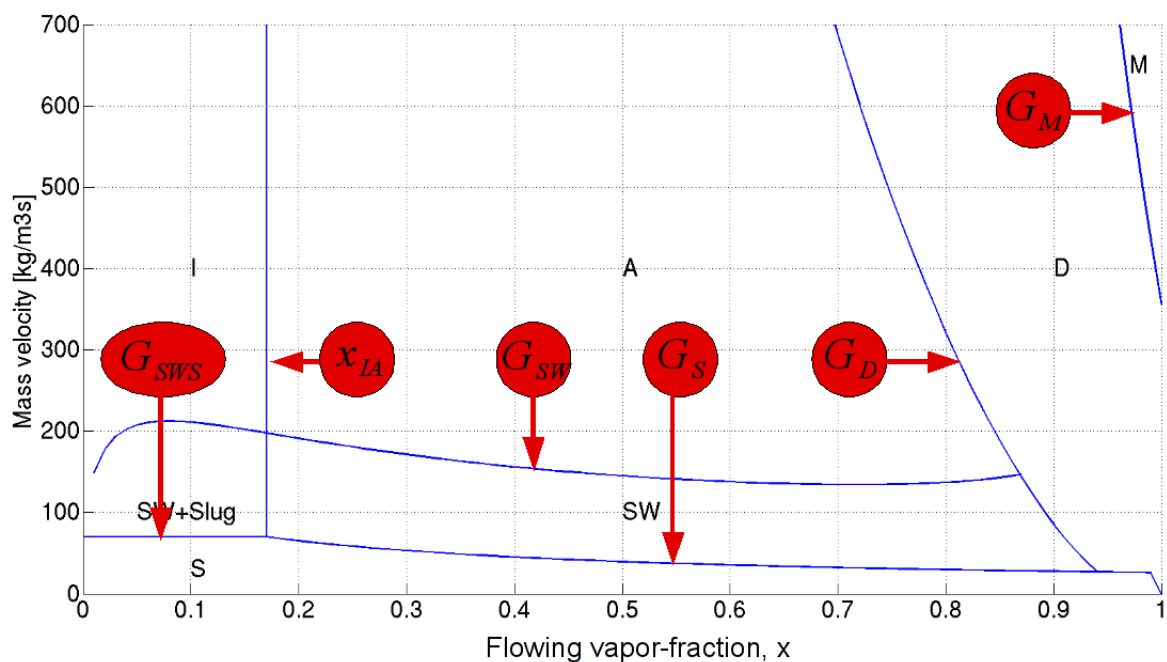


Figure H.1: The name of the transition lines in the flow-pattern map of Cheng et al.

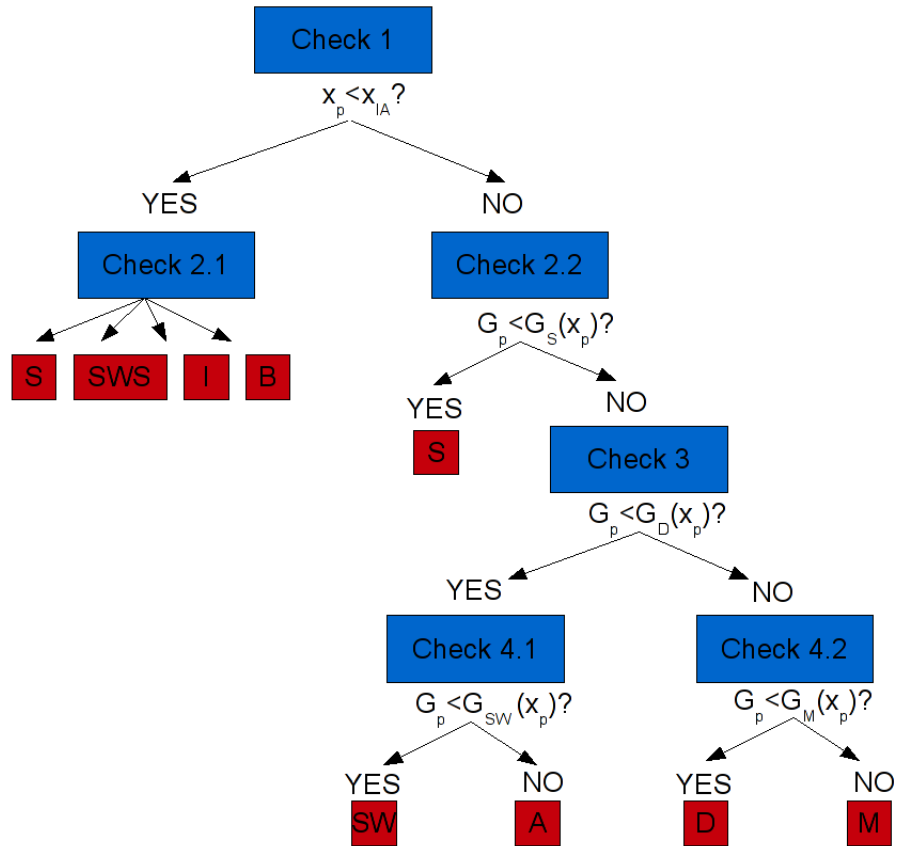


Figure H.2: The procedure used to determine the flow pattern when the fluid properties, the present mass velocity,  $G_p$ , and the flowing vapor-fraction,  $x$ , are known. For details related to check 2.1, see Figure H.3. In the trivial case where  $G = 0$ , the flow pattern will be stratified.

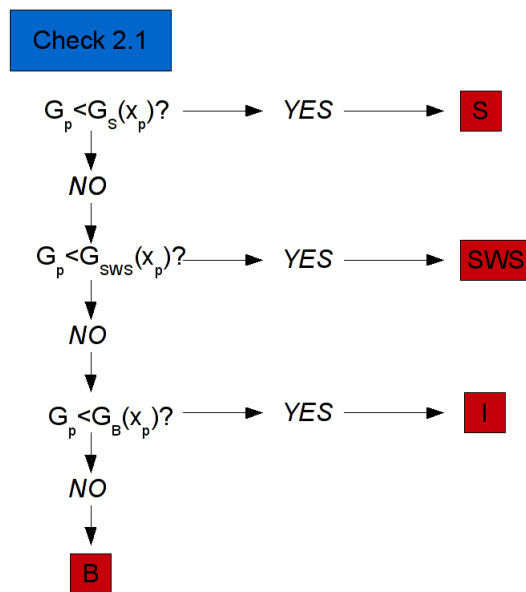


Figure H.3: The procedure used to determine the flow pattern when  $x < x_{IA}$ .